UNIVERSITÀ DI PARMA

UNIVERSITA' DEGLI STUDI DI PARMA

DOTTORATO DI RICERCA IN

"SCIENZE MEDICHE E CHIRUGICHE TRASLAZIONALI"

CICLO XXXV

TARGETING ONCOGENIC *NOTCH1* IN T-CELL ACUTE LYMPHOBLASTIC LEUKEMIA WITH A SELECTIVE SERCA INHIBITOR CAD204520

Coordinatore:

Chiar.mo Prof. Nicola Sverzellati

Tutore:

Chiar.mo Prof. Giovanni Roti

Co-Tutore:

Chiar.mo Prof. Pieter Van Vlierberghe

Dottorando: Dr. Luca Pagliaro

Anni Accademici 2019/2020 – 2021/2022

ABSTRACT

The identification of SERCA (sarco/endoplasmic reticulum calcium ATPase) as a target for modulating gain-of-function *NOTCH1* mutations in Notch dependent cancers has spurred the development of this compound class for cancer therapeutics. SERCA plays a critical role in Ca^{2+} regulation particularly in myocytes, thus inhibiting it may increase the risk of heart failure, limiting the development of this compound class for cancer therapeutics. Considering this toxicity challenge, discovery and early optimization of small molecules with better drug-like properties and reduced off-target toxicity is warranted. Despite the innate toxicity challenge associated with SERCA inhibition, we identified CAD204520, a small molecule with better drug-like properties and reduced off-target Ca^{2+} toxicity compared with the SERCA inhibitor thapsigargin. Similar to the SERCA inhibitor thapsigargin, CAD204520 inhibits Notch signaling in T-ALL leukemia cells causing a cell cycle arrest and induction of apoptosis. CAD204520 also preferentially targets mutated over wild type NOTCH1 proteins in T cell acute lymphoblastic leukemia (T-ALL) and mantle cell lymphoma (MCL), thereby overcoming the therapeutic limitation associated with the use of pan-Notch inhibitors. Remarkably, CAD204520 resulted in an effective treatment in a *NOTCH1*-mutated T-ALL *in vivo* model without causing overt Ca^{2+}-related cardiac toxicity. To anticipate the potential mechanism of resistance to SERCA inhibitors, we generated a T-ALL cell line resistant to the effect of thapsigargin. A subsequent small molecule library screening identified glucocorticoids among the top hits in the resistant cell line. This effect is at least in part mediated by the specific upregulation of glucocorticoid receptor. Consequently, the association of SERCA inhibitors and glucocorticoids displayed a synergistic effect in multiple preclinical models. This study supports the development of SERCA inhibitors for Notch-dependent cancers and extends their application to cases with isolated mutations in the

PEST degradation domain of NOTCH1, such as MCL or chronic lymphocytic leukemia (CLL). Furthermore, this study suggests that SERCA-Ca^{2+} modulation mediates glucocorticoid signaling and that innovative SI can pharmacologically modulate glucocorticoid resistance in T-ALL.

INDEX

INTRODUCTION

Targeting Notch Trafficking

The Notch signaling pathway plays an important role in the pathogenesis of human cancers. Notch controls both cell-intrinsic and extrinsic circuits leading to tumor development, progression and response to therapy. Several therapeutic efforts have historically focused on modulating Notch signaling by using small molecules such as γ-secretase inhibitors (GSI) or antibody-based strategies. However, these approaches have a poor therapeutic window - wild type vs mutant proteins - limiting their application in human diseases. This is not the case of small molecules targeting the sarco-endoplasmic reticulum Ca^{2+}-ATPase (SERCA). SERCA inhibition hijacks Notch trafficking and its activation, emerging as druggable approach for *NOTCH*-dependent cancers.

SERCA

SERCA proteins belong to the superfamily of active transporters known as P-type ATPases (E1/E2-type) located in the endoplasmic reticulum (ER). In 1993 Toyoshima and colleagues described the first complete structure of SERCA by cryo-electron microscopy (1). Subsequently, novel high-resolution techniques shaped the resolution of several crystallography structures of SERCA. These studies showed how ligands (e.g., vanadate, thapsigargin) bind SERCA, and what structural changes occur during the enzymatic catalytic cycle (2-6). The SERCA protein comprises ten helices (M1-M10), a small luminal tail and three cytoplasmic domains (A, actuator; N, nucleotide binding; P, phosphorylation). These modules mediate ATP hydrolysis, hydron ($H^{+)}$ and calcium (Ca^{2+}) binding and their transport through ER membrane (7). *ATP2A1* (16p11.2), *ATP2A2* (12q24.11) and *ATP2A3* (17p13.2) genes encode for SERCA1, 2 and 3 respectively (8, 9). Today, over 70 SERCA isoforms

resulting from alternative splicing are deposited in the Protein Data Bank database (www.rcsb.org). While these transcripts share up to 85% of sequence homology, differences in tissue distribution, Ca^{2+} binding affinity both in normal and cancer tissue are due to changes in the protein C-terminal region (10-15).

SERCA proteins maintain intracellular Ca^{2+} homeostasis by pumping Ca^{2+} from cytosol into the ER (16). This adenosine triphosphate (ATP) (10) dependent catalytic cycle alternates different SERCA phosphorylated intermediates (*E1P*; *E2P*) with different conformation for high (*E1*-Micromolar-μM) or low (*E2*-Millimolar-mM) affinity for Ca^{2+}: this cycle, named Post-Albers scheme by the first proponent, was originally applied to other types of ion pump, such as the Na^+/K^+-ATPase, and subsequently adapted to SERCA (17). The net balance of the ATP hydrolysis required to complete the cycle is of two Ca^{2+} ions transferred from the cytosol to the ER lumen, and two or three protons in the opposite direction towards the cytosol (18) (Figure 1).

All SERCA isoforms present two Ca^{2+} binding sites (site I and II) between four transmembrane (TM) helices (M4, M5, M6 and M8), near the cytoplasmic side of the membrane. Site I contains five amino acids residues from three different transmembrane helices associated with two water molecules: Asn^{768} and Glu^{771} from M5, Thr^{799} and Asp^{800} from M6 and Glu^{908} from M8 (19). Site II is located on the cytoplasmic surface next to the site I and it is composed of Ile^{307} and Gly^{310} from M4 helix, that is partially unwound, and Asn^{796} and Asp^{800} from M6; both sites provide one to three chain of oxygen to the co-ordination (19). Interestingly, the binding of the first Ca^{2+} ion on site I acts in a cooperative way, bringing to a conformational change on the oxygen chains of site II and allowing an high affinity state for the second ion binding (16, 19, 20).

SERCA, is organized in functional domains that mediate ions binding, ATP hydrolysis and ions transport through membrane (7). The N domain is the largest one to accommodate through the binding at the Phe^{487} residue, the adenine ring of the ATP (19, 21, 22). The N-domain is linked, through the Arg^{560} residue to the surrounding enzymatic P domain that contains the amino acid residues targeted by the phosphorylation. For example, phosphorylation of the Asp^{351} residue allows for a 25-30 Å rearrangements of the P-domain-ATP complex leading to generation of the high energy enzyme intermediate (16, 20, 22, 23). The A domain realizes the gating mechanism of calcium transport. The A domain is the smallest cytosolic domain and is situated near the M1, M2 and M3 helices with which is bound by flexible linkers allowing a better range of movement for ATP utilization. Similarly to other P-type ATPases, the A domain presents conserved protein motives such as the TGES motif, responsible for the dephosphorylation of the Asp^{351} residue during the catalytic cycle (16, 19, 20, 23, 24). The high-resolution crystal structures of the SERCA bound to Ca^{2+}, thapsigargin, and vanadate provided the frame for the understanding of structural changes occurring during the catalytic cycle (19). Thapsigargin binds to SERCA fitting in a cavity composed by M3, M5 and M7 helices (25). The most important amino acid residue that interacts with Thapsigargin is Phe^{256} on M3 helix, assisted by Ile^{765} on M5 and Tyr^{837} on M7 (25, 26). Mutations affecting the residue Phe^{256} bring to thapsigargin resistance confirming the pivotal role of this amino acid in the inhibition of the enzyme, even if the reduction of sensitivity of SERCA caused by the mutation is different among the isoforms, with SERCA2b the least affected (14, 26). Other SERCA inhibitors, like cyclopiazonic acid (CPA) or 2,5-di-(t-butyl)-1,4-benzohydroquinone (DBHQ), bind the enzyme in a different pocket, between the transmembrane helices M1, M2, M3 and M4 (27, 28), identified as the entrance pathway of calcium ions from cytosol (29).

The conformational rearrangement that changes during the catalytic cycle involving the N, A, and P domains along with the TM helices allow for a continued alternated access of Ca^{2+} site I and II to the cytoplasmic and luminal sides (16). At the resting state (*E2*-ATP state) SERCA presents two Ca^{2+} binding sites exposed to the cytoplasmic side; in this conformation ATP is located on N-domain and it is far from Asp^{351} residue on the P-domain (20, 30). The subsequent exchange of two Ca^{2+} ions for two or three protons ($Ca^{2+}{}_2$-*E1*-ATP state) causes a conformational change in the M1-M4 helices. The binding to Ca^{2+} breaks the closed configuration and enables a rotation of the A-domain to allow the shifting of N-domain to the Asp^{351} and the consequent autophosphorylation (20, 31). The transfer of the gamma-phosphate to the aspartate residue generates a high energy intermediate ($Ca^{2+}{}_2$-*E1*-ADP-P state) (31), followed by a substitution of ATP ($Ca^{2+}{}_2$-*E2*-ATP state) and a rotation of N-domain and A-domain of 30° and 110° respectively. The consequent movement of the A-domain induces a pairing of the M1-M2 and M3-M4 helices with the M5-M10 complex. This conformational change in TM domains leads to the opening of Ca^{2+} sites towards the luminal side and to the subsequent Ca^{2+} release (18-20, 32). The following binding of two or three protons determines the closure of the luminal channel and compensates the negative charge of Ca^{2+} sites ($H^{+}{}_{2/3}$-*E2*-ATP state). In this state the conserved P-type ATPase signature sequence fits into the phosphorylation site of P-domain and reacts with water, liberating phosphate. The catalytic cycle ends with the release of protons to the cytosolic side leading to the reacquisition of a resting state (*E2*-ATP state) (20, 23). Thapsigargin and the other SERCA inhibitors inhibit the enzyme in a calcium-free state (*E2* state), avoiding the high affinity binding of Ca^{2+} and the following activation of the catalytic cycle (25, 29, 33, 34).

Each step of the above-described catalytic cycle corresponds to a protein rearrangement required for the ions transport (7, 17, 35). For example, the transition between *E1*-ATP to E2-ATP state (7, 23, 36) identifies the luminal/extracellular pathway (Ca^{2+} out, H^{+} in) mediated by the M1-M6 helices. The N-path, or cytoplasmic pathway, regulates through the M1, M2 and M4 the transport and the binding of two Ca^{2+} and represents the passage from $Ca^{2+}{}_2$-*E1*-ATP state to $Ca^{2+}{}_2$-*E1*-ADP-P state (5, 30). Finally, the C-path identifies two different hydrated pathways on luminal side for the exit of calcium or protons that avoid to share a single access channel (7, 37).

SERCA presents different isoforms resulting from alternative splicing. These transcripts share up to 85% of sequence homology resulting in differences in the sequence of the C-terminal region of the protein, in tissue specific distribution, and for Ca^{2+} binding affinity (10-15).

SERCA1 is preferentially expressed in fast-twitch skeletal muscles in two variants: SERCA1a (994 amino acid residues) expressed in adults, and SERCA1b (1001 residues) typical of fetal-neonatal stage. As they are functionally identical, the seven additional residues on SERCA1b isoform may play a role during muscle development (38). SERCA1 shows the same affinity to Ca^{2+} compared to SERCA2a, but with an higher kinetic turnover rate (20). Overexpression of SERCA1 in a murine model of ischemia-reperfusion injury re-establishes Ca^{2+} homeostasis and diminishes the disease progression (39-41), a therapeutic effect also seen with the overexpression of SERCA2a (42), suggesting that SERCA1 can functionally act as SERCA2 in cardiac muscle (39). Interestingly loss function mutations of *ATP2A1* cause the Brody syndrome, a rare autosomal dominant genetic condition characterized by a severe myopathy. In these patients, reduced expression of

SERCA1 leads to painless muscles cramping and stiffening after exercise or cold temperatures (43, 44).

SERCA2 may results from four different splice variants numbered form “a” to “d”. SERCA2a (997 residues) is mainly expressed in cardiac muscle, slow-twitch skeletal muscle and smooth muscle cells (45). In cardiomyocytes, similarly to SERCA1a, SERCA2a is reversibly and cooperatively inhibited by two micropeptides: phospholamban (PLN) and sarcolipin (SLN) (46-48) that together with others like myoregulin (MLRN), endoregulin (ELN) and another-regulin (ALN) act as strong regulators of SERCA expression and activity (49-51). SERCA2b is located in all cell types and shows the highest affinity for Ca^{2+} (K_{Ca}^{2+} 0.2 μM) among the other isoforms (52). SERCA2b accounts for 1042 amino acid residues protein, and the difference in size between SERCA 2a and 2b is due to the presence of an M11 transmembrane helix which extends the C-terminal tail into the ER lumen (47, 53). Recently, additional SERCA2 isoforms have been described. For example, SERCA2c is expressed in cardiac muscle (54), and at lower extent in hematopoietic and epithelial cells (55). Finally, SERCA2d mRNA is transcribed in skeletal muscle but the enzymatic activity of this protein is not certain (56). Similarly to loss SERCA1 activity, *ATP2A2* mutations causes an inherited autosomal dominant disease, the Darier disease (*keratosis follicularis*), a severe skin disorder characterized by skin wart-like blemishes, due to loss of adhesion between epidermal cells (57, 58); interestingly, over 100 mutations are responsible of the disease phenotype, and only those that involved both SERCA2a and SERCA2b gene locus are specific to the Darier disease (59, 60).

The pattern of *ATP2A3* expression is similar to the one described for SERCA2b. In fact, SERCA3 is expressed in several tissue including hematopoietic cells, fibroblasts, epithelial and endothelial cells (61) and more recently in cardiac muscle cells (62). While several

isoforms have been described (form “a” to “f”), SERCA3 shows the lowest affinity for Ca^{2+} (K_{Ca}^{2+} 1.2 μM) and is scarcely regulated by PLN (63-68).

SERCA and Cancer

The potential involvement of SERCA in cancer progression has been an active area of investigation given its role in Ca^{2+} homeostasis and its associated effect on cell survival and ER stress pathway (10). While SERCA mutations are rare, altered expression is frequent as described in colorectal (69), gastric (70), thyroid (71), prostate (72, 73), lung cancer, head and neck squamous cell carcinoma (74) and hematological malignancies (75, 76). This overexpression may result from the activation oncogenic signal mediated by *BCL-2*, *RAS* (77, 78) and *TP53* (79) genes.

The preferential expression of one of the three proteins, SERCA1-3, may determine differences in the cellular behavior. For example, SERCA2 overexpression protects from apoptosis (68), while aberrant SERCA3 expression co-occurs in differentiating cells (10). Park and colleagues showed that the overexpression of SERCA2 and BCL-2 is a consequence of the repositioning of the nuclear factor kappa B (NF-kB) secondary to calcium/calmodulin-dependent protein kinase 2 alpha (CaMK2α) activation in metabolic stress-resistant breast cancer cell lines MDA-MB-231 and MCF-7 (80, 81). They next showed that combined treatment with thapsigargin, a general SERCA inhibitor, and 2-deoxy-D-glucose (2-DG, acting as an NF-kB inhibitor) reduces the tumor burden while 2-DG alone, that mimics glucose starvation, had a lower effect in a breast cancer xenograft model (81). Overall, these data suggest that SERCA2 overexpression is a general mechanism to evade apoptosis (82) and may result from the activation of metabolic stress.

A second observation is that SERCA expression may vary during epithelial differentiation and carcinogenesis. For example, in colon cancer, SERCA3 expression increases in colonic mucosa and hyperplastic polyps, while it reduces in dysplastic, moderately or poorly differentiated carcinoma cells (83). However, the expression of SERCA isoforms is not mutually exclusive in cancer cells. In fact, cancer cells may simultaneously have multiple SERCA isoforms and the net contribution to the cancer phenotype is a balance between the expression of different transcripts (84). For example, SERCA2 and SERCA3 are oppositely regulated in acute promyelocytic leukemia (APL) cell lines HL-60 and NB4 and freshly isolated APL cells treated with the pro-differentiating agent all-trans-retinoic acid (ATRA) *in vitro* (76). A similar effect is seen during the differentiation of MEG 01, UT7, M-07e and CHRF 288-11 erythro-megakaryoblastic leukemia cell lines treated with 10^{-8} M of the phorbol ester PMA (85). Collectively these studies suggest that the down regulation of SERCA3 and overexpression of SERCA2 are a key process in leukemia stem cell and cancer maintenance (10).

While SERCA mutations are rare in cancer, some studies have demonstrated the involvement of genetic alterations of *ATP2A* genes in tumor development, mainly for lung and colon cancer (86). Liu and colleagues showed that heterozygous mutant *ATP2A2* mice develop late-onset squamous cell tumors in the gut and in the skin where the expression of SERCA2 protein is reduced due to haploinsufficient loss-of-function mutations (74). Toki and colleagues confirmed these initial observations and showed that the onset of *ATP2A2* deficient tumor depends on the level of SERCA residual activity (87) suggesting that SERCA haploinsufficiency may predispose to multistage carcinogenesis by altering Ca^{2+} homeostasis (88).

SERCA and Notch

NOTCH is a surface receptor that drives many aspects of embryonic cell development, and adult tissue differentiation. Mammalian organisms express four NOTCH receptors that are activated by nearly identical mechanisms. This pathway requires a spatial-temporal control of a cascade of proteolytic cleavages (S1-S3). A furin-like protease (S1) processes a pro-NOTCH form in the ER/Golgi compartment into a non-covalent heterodimer between the extracellular Notch domain (ECD-N) and a transmembrane domain (TM-N1) that is subsequently expressed on the surface of the cells. ECD-N contains 36 N-terminal epidermal growth factor (EGF)-like repeats that participate in binding to ligands and three iterated LIN-12/NOTCH repeats (LNR), which maintain NOTCH receptors in the “off” state prior to ligand binding. In the “canonical” Notch signaling, ECD-N binds through cell-to-cell contact ligands (DLL1-4, JAG1-2) and activate metalloproteases (S2) (ADAM-10 or ADAM-17) to release trans-membrane short-lived intermediates that are the substrate of the gamma-secretase complex (S3). This latest event releases NOTCH fragments (ICN, ICD-N) that associate with a co-transcription factor Mastermind-like (MAML) family and complex with the DNA-binding factor recombination signal binding protein for immunoglobulin kappa J region (RBPJ) to drive transcription (89). Most genetic alterations of NOTCH receptors in human cancers are observed in the *NOTCH1* gene. The involvement of *NOTCH1* in the pathogenesis of T-ALL, an aggressive form of leukemia that mainly affects children, was initially discovered in 1991 (90). Ellisen and colleagues described a chromosome translocation, t(7;9), that juxtaposes the promoter elements of the T-cell receptor-β (*TCRB*) to the 3’ end portion of the *NOTCH1* gene encoding its intracellular domain ICN1 (90). This fusion results in the overexpression of ICN1 that activates genes that promote T-cell leukemogenesis. Similarly, activating *NOTCH1* mutations are prevalent in hematological malignancies and sequenced in 40% to 70% of T-ALL (91), in 10-15% of CLL, MCL (92, 93)

and in a subset of B-cell-like (activated B-cell, ABC) diffuse large B-cell lymphoma (94). Most of these mutations occur in the juxtamembrane heterodimerization (HD) domain, which hold together the ECD-N with TM-N, or in the PEST (rich in proline (P), glutamic acid (E), serine (S), and threonine (T)) degron domain. In T-ALL, HD and PEST mutations may co-occur while isolated PEST are common in CLL and MCL. Here, a premature stop codon (P2514fs*4) generally truncates the C-terminal PEST region of the protein. The PEST domain controls the degradation of activated NOTCH proteins, and its deletion results in a delayed protein half-life.

In addition, the Notch signaling pathway is frequently activated in multiple types of solid tumors (95, 96), such as melanoma, colorectal carcinoma, and cholangiocarcinoma through mechanisms that differ from genetic variations (97, 98). Paradoxically, mutations that inactivate the Notch pathway have been described in several human cancers (96, 99) showing that, depending on the cellular context, Notch signaling can be oncogenic or tumor suppressive and suggesting that fine-tuned inhibition of Notch signaling could be useful in those situations where Notch is activated.

The preponderance of oncogenic *NOTCH1* mutations in T-ALL has prompted the search for effective anti-Notch1 therapeutics (75, 100). Because Notch activation relies on γ-secretase mediated proteolysis, GSI had entered in clinical trials to treat relapsed T-ALL. However, first generations of GSIs were poorly tolerated because of on-target gastro-intestinal toxicity (101-103). As showed by Riccio and colleagues the toxic effect of GSIs are a consequence of lack of substrate specificity of these molecules resulting in the combined inhibition of wild type NOTCH1 and NOTCH2 in intestinal progenitor cells (104). Although few patients achieved a complete response, GSIs exhibited moderate clinical activity in some patients with solid tumor and leukemia (105). Recently, several studies demonstrated that combining

GSIs with chemotherapy or other targeted agents increases the anti-cancer effects of these drugs (106-109), supporting the development of innovative anti-Notch1 therapeutics.

The rise of SERCA inhibitors for cancer therapeutics date back to 1960 when the National Cancer Institute (NCI) launched a program to identify compounds with antitumor activity from 35,000 plants extracts (110). Sesquiterpene lactone (SL) derivatives demonstrated an anti-inflammatory and antitumor activity in several tumor types, like laryngeal carcinomas, uveal melanomas, pituitary macroadenomas, kidney, prostate cancer and hematological malignancies (111-116). Among others, thapsigargin, parthenolide and artemisinin were selected for their potency and initially used as tool compounds in different cancer models. Several SERCA inhibitors which differed in their source, chemical structure, potency and binding affinity to specific SERCA isoforms were subsequently developed (82).

In 1999, Goran Periz and Mark E. Fortini described that the trafficking events leading to a correct NOTCH activation may be disrupted in the presence of a defective Ca^{2+}-ATPase function in a Drosophila model. In this work, the authors demonstrated that loss-of-function alleles of the Drosophila SERCA homologous gene *Ca-P60A* alters proper synthesis, folding and trafficking of the NOTCH receptor in the ER/Golgi compartments (Figure 2). Consistently, in Drosophila S2 cultured lines, the treatment with general SERCA inhibitors such as thapsigargin and CPA primarily reduces the amount of NOTCH proteins that reach the cell surface (117). While extremely interesting, these observations were not confirmed in mammalian cells until, Giovanni Roti and Kimberly Stegmaier embarked on a large gene-expression based screening (GE-HTS) effort to identify inhibitors of oncogenic *NOTCH1* signatures or enhancer of *NOTCH1* HD mutant L1601PΔP activity in T-ALL. Among the top hits were the genes *ATP2A2* and *ATP2A3*, and SERCA inhibitors such thapsigaricin (an analogue of thapsigargin) and CPA. Together with other ion flux modulators, SERCA

emerged as a novel potential therapeutic target in *NOTCH1*-associated cancers (75, 118). Furthermore, these data suggest the hypothesis that Notch signaling could be dysfunctional in several genetic disorders associated with loss of function *ATPA1-3* mutations.

However, thapsigargin binding to SERCA results in an increase in cytosolic Ca^{2+} concentration and a depletion of Ca^{2+} stored in the ER. Thus, the delivery of free thapsigargin to humans might cause cardiac toxicity due to a rapid calcium ion shift. To overcome this limitation in the past we generated a thapsigargin pro-drug taking advantage of the dependency of ALL on folic acid (FA) and, tagged folate to a permissive site on an active alcohol derivative of thapsigargin (8-*O*-debutanoylthapsigargin) via a cleavable ester linkage (JQ-FT) (119). However, an alternative approach to reducing the potential toxicity of thapsigargin is through the identification of SERCA inhibitors that retain the anti-Notch properties but lack Ca^{2+} related toxicities (Figure 3).

AIM OF THE STUDY

Given its critical oncogenic role in several human cancers, Notch1 signaling has garnered increased attention as a potential therapeutic target. To date, several Notch inhibitors, including GSI, have shown therapeutic efficacy in preclinical cancer models. However, despite this promise, few of these candidates have been demonstrated to have a meaningful clinical benefit for patients, in part due to tissue-dependent on-target toxicities from the simultaneous repression of both mutant and wild type NOTCH proteins.

The discovery of SERCA as actionable modulators of Notch1 suggested a new targeted approach to treat T-ALL. Uniquely among Notch modulators, SERCA inhibitors preferentially impair the clinically relevant class of oncogenic *NOTCH1* mutants compared to wild type. Thus, the development of tolerated SERCA modulators may uncover a new therapeutic avenue for one of the most frequently mutated genes in human cancers.

In this work, we identified a new series of P-type ATPase/SERCA inhibitors and characterized the effect of CAD204520 in *NOTCH1*-mutated T-ALL. We demonstrated that CAD204520 exhibits a reduced Ca^{2+} related off-target toxicity but retains anti-Notch1 and anti-leukemia capacity both *in vitro* and *in vivo* in *NOTCH1*-mutated T-ALL models. In addition, we extended the testing of CAD204520 in B-cell malignancies carrying clinically relevant PEST mutations and demonstrated, for the first time, the potential of SERCA inhibition as a therapeutic approach in these diseases.

Furthermore, to anticipate the potential mechanism of resistance to SERCA inhibitors, we generated a T-ALL cell line (ALL/SIL) resistant (R) to the effect of thapsigargin by exposing the cells to increased concentrations of thapsigargin. Exome sequencing analysis identified a mutation (c.G770T→ p.G257V) in the *ATP2A2* locus that impedes an efficient thapsigargin

binding to the protein, finally resulting in a diminished inhibitory effect. we then screened a small molecule library of nearly 2500 bioactive compounds (from the European Chemical Biology Library provided by EU-OPENSCREEN) in ALL/SIL and ALL/SIL R. Compound hits were flagged by their ability to preferentially inhibits ALL/SIL, ALL/SIL R, or both. Confirmatory experiments and pathway analysis were completed in multiple T-ALL preclinical models.

MATERIALS AND METHODS

Experimental Models and Subject Details

Animals

NOD-*scid* IL2Rgamma^{null} (NSG) mice (The Jackson labs, RRID: IMSR_JAX:005557) for efficacy studies were maintained in specific pathogen–free facilities at the ‘‘Preclinical Research Services Center’’ (Ce.Se.R.P) at the University of Perugia (08/2018-UT of 07/24/2018). Animal procedures were approved by the University of Perugia IACUC following the DL 26/2014 and 2010/63/EU guidelines for the protection of animals used for scientific purposes. Pharmacokinetics (PK) and tolerability studies were performed at Aurigene Discovery Technologies, India. In-house breed CD1 (ICR) or BALB/cAnNCr mice for pharmacokinetics (PK) and tolerability studies were maintained in individually ventilated cages at the Aurigene facility in Hyderabad in India.

To assess effect of CAD204520 on the cardiac mechanics, cardiomyocytes were isolated from 12-14 week aged Wistar rats (Rattus norvegicus, Charles River Laboratory, RRID: RGD_13508588) of 362 ± 5 g in weight. Animals were housed in a temperature-controlled room (22–24°C), with a 12 hour light cycle (light on from 7.00 AM to 7.00 PM) with unrestricted food and water supply. Experiments were performed under the Veterinary Animal Care and Use Committee of the University of Parma-Italy and conform to the National Ethical Guidelines of the Italian Ministry of Health (Prot. N 614/2016-PR) and the Guide for the Care and Use of Laboratory Animals (National Institute of Health, Bethesda, MD, USA, revised 1996).

Yeast Cells

Saccharomyces cerevisiae RS72 yeast cells (ATCC #9763) for the biochemical ATPase assay were pre-cultured in 100 ml sterile SGAH medium (7.04 g/L yeast nitrogen base, 19.8

g/L galactose, 64 mg/L adenine, 64 mg/L histidine) for 3 days at 25°C and 150 rpm. The pre-culture was transferred to 500 mL sterile SGAH medium and further incubated for 3 to 4 days. 100 mL from the cell culture was transferred to 1 L YPAD medium (10 g/L yeast extract, 20 g/L bacto-peptone, 20 g/L glucose, 20 mg/L adenine) and incubated at 25°C for 18-20 hours.

Cell Lines

Human cell lines DND41 (source: male), MOLT16 (source: female), PF382 (source: female), RPMI-8402 (source: female), SKW-3/KE-37 (source: male), JURKAT (source: male), CTV-1 (source: male), HBS2 (source: male), Loucy (source: female) and PEER (source: female), REC-1 (source: male), Mino (source: female), were purchased from Leibniz-Institut DSMZ-German collection of microorganisms and cell cultures (Germany); the identity of ALL/SIL (source: male) was confirmed by PCR sequencing for known *NOTCH1* mutations and short tandem repeat (STR) loci profiling and they were kindly provided by Stegmaier laboratory. MAVER-1 (source: male) cells were a gift from the Muraro laboratory (C.R.O. National Cancer Institute, Aviano, Italy). Cells were cultured in RPMI 1640 (Fisher Scientific, Waltham MA, USA #MT10040CV) with 10% or 20% fetal bovine serum (FBS) (Thermo Fisher Scientific, Waltham MA, USA, #10270-106) and 1% penicillin-streptomycin (Fisher Scientific, Waltham MA, #3MT30002CI) and incubated at 37°C with 5% CO_2. 293T (source: human primary embryonal kidney cell line 293 (ACC 305)) cells were purchased Leibniz-Institut DSMZ-German collection of microorganisms and cell cultures (Germany) and cultured in DMEM (Fisher Scientific, Waltham MA, USA #11965-084) with 10% FBS and 1% penicillin-streptomycin and incubated at 37°C with 5% CO_2. HL-1 cardiac muscle cell line was a kind gift from the Miragoli laboratory (University of Parma, Parma, Italy). HL-1 cells were plated on a gelatin layer derived from bovine skin/fibronectin (1mg/ml) (Sigma-Aldrich, St. Louis, MO, USA, #G9391 and #F-1141) coated T25 flask and cultured in Claycomb

medium (Sigma-Aldrich, St. Louis, MO, USA, #51800C) with 10% FBS, 1% penicillin-streptomycin, 2mM L-Glutamine (Thermo Fisher Scientific, Waltham MA, USA, Waltham MA, USA, #25030081), 0,1mM Norepinephrine [(±)- Arterenol] plus L-Ascorbic acid, sodium salt (Sigma-Aldrich, St. Louis, MO, USA, #A0937 and #A7506) and incubated at 37°C with 5% CO_2. Cytogenetic, FISH and mutation analysis was completed according to validated methods as previously described (120, 121).

Primary Samples

T-ALL lymphoblasts were obtained from patients with leukemia under an approved protocol at the Parma University Hospital (n.18249/18/05/2017) and according to the declaration of Helsinki guidelines for the protection of human rights. Peripheral blood (PB), and bone marrow (BM) samples were collected at the time of diagnosis, and we retained samples with blasts >85%. Mononuclear cells were isolated by density gradient centrifugation using LSM-lymphocyte separation medium (CappelTM MP Biomedicals, LLC, Ohio, USA #50494). Lymphocytes were isolated from peripheral blood mononuclear cell (PBMC) by using a CliniMACS Prodigy (Miltenyi Biotec, Bergisch Gladbach, Germany) and cultured for a short time using the same growth conditions described above.

Data and Code Availability

The model and structure factors for the SERCA-CAD204520 complex structure reported in this paper have been deposited in the Protein Data Bank: PDB: 6YAA.

Preparation, Crystallization and Structure Determination of the SERCA-CAD204520 Complex

Rabbit sarcoplasmic reticulum (SR) membranes containing SERCA were prepared from rabbit hind leg muscle as previously described (122). Briefly, muscle tissue was dissected and minced in 10 mM KCl, 2.5 mM K_2HPO_4, 2.5 mM KH_2PO_4, 2 mM EDTA, followed by centrifugation at 4°C for 20 min and 6.400 x g, supernatant filtered and spun at 9.700 x g for 20 min. SR membranes were sedimented by a 60 min centrifugation at 47.800 x g at 4°C. Membranes were homogenised and washed successively with buffers B (1 M sucrose, 50 mM KCl), C (1 M KCl, 3.4 mM MgATP pH 7.0), D (50 mM KCl), and E (0.3 M sucrose, 5 mM Hepes pH 7.4). Finally, washed membranes were extracted twice with extraction buffer (0.3 M sucrose, 0.5 M KCl, 1 mM EDTA, 10 mM Tris, 0.01 mM $CaCl_2$, 1.25 mM $MgCl_2$, pH 7.9, 0.5 mg/ml DOC, 0.5 mg/ml DTT) followed by centrifugation at 4°C and 181.000 x g for 75 min. The pellet was then washed with 5 mM TAPS pH 7.5, 0.3 M sucrose, 0.5 M KCl, 0.5 mM $MgCl_2$, 10 μM $CaCl_2$, and finally resuspended and flash frozen in buffer E. SERCA membranes were resuspended and gently homogenized in 100 mM MOPS-Tris pH 6.8, 80 mM KCl, 3 mM $MgCl_2$, 4 mM EGTA and 20% (v/v) glycerol. CAD204520 was added to the membrane preparation at a final concentration of 0.5 mM and incubated overnight at 4°C. The following day, 0.4 mM TNPATP were added and incubated for 15 minutes (min) prior to the solubilization of the protein with C12E8 at a detergent/protein ratio of 1.5:1 (w/w). After 10 min incubation and centrifugation (TLA-100.3 rotor, 50,000 rpm, 30 min, 4°C), the concentration of solubilized protein was usually 10–12 mg/mL. Co-crystallization of SERCA with CAD204520 was carried out using hanging drop equilibration at room temperature (RT) with protein/buffer in a 1:1 ratio. The best diffracting crystals were obtained with crystallization buffer consisting of 10% glycerol, 14% PEG 6000, 100 mM NaCl and 6% MPD. Data were collected at 100 K and a wavelength of 0.976 A at beam line I03 at the

Diamond Light Source (DLS) in Didcot, UK. The data were processed using XDS (123) and AIMLESS (124) and the structure was determined by molecular replacement in PHASER (125) using a SERCA crystal structure with matching space group (pdb: 4UU0) (126). PHENIX (127) was used for refinement, ligand fitting and model validation and COOT for model building (128). Figures were prepared with Pymol (Molecular Graphics System, Version 2.0 Schro¨dinger, LLC).

Synthesis Pathways

CAD307496 (2-[1-[3-(3-pyridyl)propyl]-2-piperidyl]-6-(trifluoromethoxy)-1H-indole) was prepared through the following intermediates:

a) Intermediate 2-[2-(2-pyridyl)ethynyl]-5-(trifluoromethoxy)aniline: 2-Bromo-5-(trifluoromethoxy)aniline (6.21g, 24,2 mM), 2-ethynylpyridine (2.50g, 24.2 mM) and potassium carbonate (8.38g, 60.6 mM) in NMP (50 mL) were degassed with argon. Pd(DtBPF)Cl2 (474mg, 0.73 mM) was added and the reaction heated under argon to 120°C for 1 hour 45 min. The reaction cooled and diluted with water, extracted with 1:1 cHexane/EtOAc (3x 150 ml), washing each extract well with water. The combined extracts were dried, evaporated, and columned on 100 g SNAP cartridge eluting with 0-60% EtOAc/cHexane, using 20 column volumes to yield 750 mg of title compound as a brown solid. This was used without further purification.
b) Intermediate 2-(2-pyridyl)-6-(trifluoromethoxy)-1H-indole: To 2-[2-(2-pyridyl)ethynyl]-5-(trifluoromethoxy)aniline (950mg, 3.41 mM) was added potassium 2-methylpropan-2-olate (383.13 mg, 3.41 mM) in DMF (50 mL) and the mixture was stirred at RT overnight. The reaction was quenched with 0.4 mL HOAc concentrated in vacuo, dissolved in diethyl ether and washed with sat. $NaHCO_3$ and water. The organic

phase was dried, evaporated, columned on 50 g SNAP cartridge eluting with 20-60% DCM/cHexane using 20 column volumes to yield 510 mg of the title compound as a yellow solid.

c) Intermediate A (2-(2-piperidyl)-6-(trifluoromethoxy)-1H-indole): 2-(2-pyridyl)-6-(trifluoromethoxy)-1H-indole (4.18 g, 15.02 mM) in ethanol (100 mL) and 1M HCl in methanol (45 mL) hydrogenated over PtO_2 (300 mg, 1.32 mM) at RT and pressure on 9.35. The mixture was warmed after 1 hour to 40°C and left overnight after which additional PtO_2 (300 mg, 1.32 mM) was added, and the reaction was stirred for another 5 hours. The catalyst was removed by filtration, and the filtrate evaporated to a white solid foam. This was taken up in DCM and crystallized upon standing. The solid was broken up with diethyl ether and filtered to yield 3.7 g of title compound. The product may be converted to the hydrochloride by standard methods known to those skilled in the art.

d) Intermediate 3-(3-bromopropyl)pyridine: to a stirring solution of 3-(3-pyridyl)propan-1-ol (0.14 g, 1 mM) in dichloromethane (2 mL) at 0°C was added carbon tetrabromide (0.5 g, 1.5 mM) then triphenylphosphine (0.42 g, 1.6 mM) portion wise, carefully. The reaction mixture was then stirred at 0°C for 2 hours. The material was applied to a DCM-wetted 5g SCX-2 cartridge; washed with DCM then eluted with 0.5 M DIPEA in DCM to yield a pink solution used in the next step.

e) To 2-(2-piperidyl)-6-(trifluoromethoxy)-1H-indole hydrochloride (100 mg, 0.31 mM) was added 3-(3-bromopropyl)pyridine (10 mL, mixture of the bromide and DIPEA in DCM and prepared described above; 0.34 mM). The reaction mixture was stirred at RT for 1 hour and then left to stand overnight. The reaction mixture was heated at 45°C and the DCM allowed to evaporate to concentrate the mixture after which DMF (1 mL) and DIPEA were added. A MDAP purification returned 35 mg of gum-like

material which was run through a 2g SCX-2 cartridge yielding the title product after evaporation in 29 mg (23%) with satisfactorily purity. QC-LC-MS (99.2%). LC-MS (ESI): (M+H)+ = 404.1.

Intermediate A was used to produce additional compounds in a fashion similarly to that used in the preparation of CAD307496.

CAD204522

From Intermediate A and commercially available 4-(2-Chloroethyl)morpholine (CAS 3240-94-6). Yield 61%. QC-LCMS (ESI): (m/z) (M+H)+ = 398.1, (M-H)- = 396.3.

CAD204521

Intermediate A and commercially available 4-bromobenzaldehyde (CAS 1122-91-4) was added followed by HOAc (0.02 ml, 0.35 mM) and sodium triacetoxyborohydride (74.55mg, 0.35 mM). The reaction mixture was stirred for 1 hour and run through a MeOH-wetted SCX-2 cartridge, washed with methanol, and then eluted with 2M NH_3 (aq). Yield 28%. QC-LCMS (ESI): (m/z) (M+H)+ = 453.0, (M-H) = 451.1.

CAD204631

(3-(2-{1-[(4-bromophenyl)methyl]piperidin-2-yl}-6-(trifluoromethoxy)-1H-indol-3-yl)propan-1-ol): Intermediate 5-(2-pyridyl)pent-4-yn-1-ol: To 2-bromopyridine (2g, 12.7 mM), bis-triphenylphosphine palladium dichloride (1.1g, 1.58 mM) and CuI (301 mg, 1.58 mM) in triethylamine (50 mL, 358.7 mM) under argon was added dropwise pent-4-yn-1-ol (3.53 mL, 38 mM) and the mixture was heated to 50°C for 21.5 hours after which the reaction was cooled, evaporated almost to dryness, and then partitioned between water and ethyl acetate. The phases were separated and the aqueous phase extracted with ethyl acetate. The combined organics were dried (sodium sulfate), filtered, and evaporated. The crude product

was purified by column chromatography (Isolera, 100 g column; 0-100% ethyl acetate in cyclohexane to provide 3.98 g (78%) of the title product as a yellow liquid.

a) Intermediate 3-[2-(2-pyridyl)-6-(trifluoromethoxy)-1H-indol-3-yl]propan-1-ol: 5-(2-Pyridyl)pent-4-yn-1-ol (3.98 g, 24.7 mM), 2-bromo-5-(trifluoromethoxy)aniline (6.32 g, 24.7 mM), potassium carbonate (8.53 g, 61.7 mM) and Pd(DtBPF)Cl2 (805 mg, 1.23 mM) in 1-methyl-2-pyrrolidinone (100 mL) were degassed then heated at 120°C under argon for 18 hours. The reaction mixture was split in two and each fraction passed through a MeOH-wetted SCX-2 cartridge (70 g); which were washed with methanol and then eluted with 2M ammonia in methanol. The ammonia fractions were evaporated and the crude product (8.3 g) was further purified on a Isolera (330 g column; 0-100% ethyl acetate in cyclohexane to yield 4.47g (54%) in accordance with the title compound.
b) Intermediate B (3-[2-(2-piperidyl)-6-(trifluoromethoxy)-1H-indol-3-yl]propan-1-ol): A solution of 3-[2-(2-pyridyl)-6-(trifluoromethoxy)-1H-indol-3-yl]propan-1-ol (2.76 g, 8.21 mM) and PtO_2 (200 mg, 0.880 mM) in ethanol (100 mL) and 1M HCl in MeOH (24.62 mL, 24.62 mM) was degassed before placing under a H_2 atmosphere at RT for 4.5 hours. The reaction mixture was filtered through celite, the filterpad washed with additional ethyl acetate after which the filtrate was evaporated to give 4.02 g of a brown oil. The crude product was purified columned on Isolera (100 g column; 0-10% (2N ammonia in methanol) in DCM) to provide 2.48 g (88%) of a brown solid consistent with the title structure.
c) From Intermediate B and commercially available 4-bromobenzaldehyde (CAS 1122-91-4) and a procedure similar to CAD204521. Yield 78%. QC-LCMS (ESI): (m/z) (M+H)+ = 511.1, (M-H)- = 509.1.

CAD204520

(4-[2-[2-[3-propyl-6-(trifluoromethoxy)-1H-indol-2-yl]-1-piperidyl]ethyl]morpholine) dihydrochloride was prepared through following intermediates:

a) Intermediate 2-Pent-1-ynylpyridine: A slurry of 2-bromopyridine (8 g, 50.63 mM) and pent-1-yne (4.14 g, 60.76 mM) in triethylamine (141.16 mL, 1012.7 mM) degassed with argon added bis-triphenylphosphine palladium dichloride (1776.96 mg, 2.53 mM) and CuI (964.3 mg, 5.06 mM) was warmed to 50°C overnight. The reaction mixture was diluted with diethyl ether and washed with water. The crude product was dried and evaporated, columned on 100 g SNAP cartridge eluting with 0-20% EtOAc/cHexane, using 15 column volumes to yield a black oil which was used without further purification.

b) Intermediate 3-Propyl-2-(2-pyridyl)-6-(trifluoromethoxy)-1H-indole: 2-Bromo-5-(trifluoromethoxy) aniline (3879 mg, 15.15 mmol), 2-pent-1-ynylpyridine (2200 mg, 15.15 mM) and potassium carbonate (5235 mg, 37.88 mM) in NMP (20 mL) were degassed with argon. Pd(dtbpf)Cl2 (494 mg, 0.760 mmol) was added and the reaction heated under argon to 120°C overnight. The reaction mixture was then diluted with water, extracted with 1:3 EtOAc/cHexane, and subsequently diethyl ether. The combined extracts were dried, evaporated and columned on 100 g SNAP cartridge eluting with 0-10% EtOAc/cHexane to yield 2.225 g of product.

c) Intermediate E: (2-(2-Piperidyl)-3-propyl-6-(trifluoromethoxy)-1H-indole hydrochloride): 3-Propyl-2-(2-pyridyl)-6-(trifluoromethoxy)-1H-indole (2.23 g, 6.95 mM) in ethanol (50 mL) and 1M HCl in methanol (21 mL) was hydrogenated over PtO2 (450 mg, 2.00 mM) at 40°C for 7 hours after which the reaction mixture was left overnight at RT, in a hydrogen atmosphere. The reaction mixture was filtered, evaporated and taken up in 20 mL DCM. A white precipitate formed when 50 mL

diethyl ether was added to give after drying 1.066 g (42%) of product. The mother liquor was columned after evaporation on a SNAP (50g) cartridge eluting with 0-10% NH_3 in MeOH/DCM, using 15 column volumes. Fractions containing products were combined and evaporated to dryness to yield 0.544 g (23%) of title compound as the free base providing a combined yield of 66%.

d) 4-[2-[2-[3-propyl-6-(trifluoromethoxy)-1H-indol-2-yl]-1 piperidyl]ethyl]morpholine dihydrochloride: 2-(2-Piperidyl)-3-propyl-6-(trifluoromethoxy)-1H-indole (140 mg, 0.430 mM), 4-(2-chloroethyl)morpholine hydrochloride (87.81 mg, 0.470 mM) and sodium bicarbonate (108.11 mg, 1.29 mM) in methyl alcohol (2 mL) was refluxed under argon for 75 min. The reaction mixture was filtered and concentrated, loaded onto an elute 5 g cartridge and eluted with EtOAc, then 5% MeOH/DCM. The crude product was further purified by Xselect CSH 5 micron C18 prep column (19x250 mm) HPLC eluting with 10-60% MeCN/water (+0.1% HCO_2H) to yield a product which was taken up in MeCN, 1M HCl (aq) and freeze dried to yield a white solid, 70 mg (31%) QC-LCMS (ESI): (m/z) (M+H)+ = 440.2, (M-H)- = 438.2.

CAD204519

From Intermediate E and commercially available 4-bromobenzaldehyde (CAS 1122-91-4) and a procedure similar to CAD204521. Yield 26%. QC-LCMS (ESI): (m/z) (M+H)+ = 495.0 (M-H)- = 493.1.

CAD306750

(1-{[(4-fluorophenyl)methyl]amino}-3-{2-[3-propyl-6-(trifluoromethoxy)-1H-indol-2-yl]piperidin-1-yl}propan-2-ol):

a) Intermediate F: 1-Chloro-3-[2-[3-propyl-6-(trifluoromethoxy)-1H-indol-2-yl]-1-piperidyl]propan-2-ol: 2-(Chloromethyl)oxirane (163 mg, 1,76 mM) was dissolved in

dichloromethane (1mL) and methyl alcohol (0.5 mL) and 2-(2-piperidyl)-6-(trifluorome- thoxy)-1H-indole (Intermediate E, 500mg, 1.76mmol) was added. The reaction mixture was stirred at RT for 19 hours after which the reaction mixture was evaporated and columned on the Isolera (50 g cartridge, 0-5% (2N ammonia in methanol) in DCM) (yield 74%).

b) Intermediate (1-{[(4-fluorophenyl)methyl]amino}-3-{2-[3-propyl-6-(trifluoromethoxy)-1H-indol-2-yl]piperidin-1-yl}propan-2-ol): From Intermediate F and commercially available 4-fluorobenzylamine (CAS 140-75-0) and sodium iodide (25.9 mg, 0.17 mM) in N,N-dimethylformamide (1mL) was heated at 70°C for 22 hours after which the reaction was poured into water and extracted with EtOAc. The organic phases were dried (sodium sulfate), filtered and evaporated. The crude material was purified using Isolera column chromatography (0-10% (2N ammonia in methanol) in DCM). The crude product was further purified using preparative HPLC (C18, Xselect, 20-80% MeCN in water plus 0.1% formic acid). Yield 33%. QC-LCMS (ESI): (m/z) (M+H)+ = 508.1, (M-H)- = 506.2. The product is a 1:1 mixture diastereomer.

CAD306749

This compound was produced in a similar way as CAD306750 from Intermediate F and commercially available 1-(3-Bisphenylyl) methanamine (CAS 177976-49-7). Yield 19%. QC-LCMS (ESI): (m/z) (M+H)+ = 566.2 (M-H)- = 564.2

CAD305666

(2-[2-[1-[(4-bromophenyl)methyl]-2-piperidyl]-6-(trifluoromethoxy)-1H-indol-3-yl]ethanol):

a) Intermediate 2-[2-(2-pyridyl)-6-(trifluoromethoxy)-1H-indol-3-yl]ethanol: Was prepared similar to CAD204631 step (a). Yield 52%.

b) Intermediate 2-[2-(2-piperidyl)-6-(trifluoromethoxy)-1H-indol-3-yl]ethanol was prepared similar to intermediate B (step (b) for CAD204631). Yield 45%.

c) Intermediate 2-[2-[1-[(4-bromophenyl)methyl]-2-piperidyl]-6-(trifluoromethoxy)-1H-indol-3-yl]ethanol was obtained using Intermediate 2-[2-(2-piperidyl)-6-(trifluoromethoxy)-1H-indol-3-yl]ethanol and commercially available 4-bromobenzaldehyde (CAS 1122-91-4) and a procedure similar to CAD204521. Yield 87%. QC-LCMS (ESI): (m/z) (M+H)+ = 497.1 (M-H)- = 495.1.

CAD204630

(2-[1-[(4-bromophenyl)methyl]-2-piperidyl]-3-isopentyl-6-(trifluoromethoxy)-1H-indole hydrochloride):

a) Intermediate 3-isopentyl-2-(2-pyridyl)-6-(trifluoromethoxy)-1H-indole: By a method similar to that of CAD204631 step (a) above using commercially available 2-Bromo-5-(trifluoromethoxy)aniline (CAS 887267-47-2) and 2-(5-methylhex-1-ynyl)pyridine. Yield 60%.

b) Intermediate 3-isopentyl-2-(2-piperidyl)-6-(trifluoromethoxy)-1H-indole: By a method similar to intermediate B (step b for CAD204631). Yield 56%.

c) 2-[1-[(4-bromophenyl)methyl]-2-piperidyl]-3-isopentyl-6-(trifluoromethoxy)-1H-indole hydrochloride: By a method similarly to that of CAD204521 employing commercially available 4-bromobenzaldehyde (CAS 1122-91-4). Yield 62%. QC-LCMS (ESI): (m/z) (M+H)+ = 523.1 (M-H)- = 521.1. Note: Many of the compounds are racemates i.e. of enantiomers or diastereomers. The pure enantiomer was not isolated

ATPase Preparation

Heat competent *Saccharomyces cerevisiae* RS72 yeast cells (129) were transformed using a lithium acetate, single-stranded carrier DNA/polyethylene glycol method and with a yeast multicopy vector (130) containing the full-length cDNA of the S. cerevisiae plasma membrane H^+-ATPase isoform *PMA1* under control of the *PMA1* promoter. Transformed yeast cells were pre-cultured in 100 mL sterile SGAH medium (7.04 g/L yeast nitrogen base, 19.8 g/L galactose, 64 mg/L adenine, 64 mg/L histidine) for 3 days at 25°C and 150 rpm. The pre-culture was transferred to 500 mL sterile SGAH medium and further incubated for 3 to 4 days. 100 mL from the cell culture was transferred to 1 L YPAD medium (10 g/L yeast extract, 20 g/L bacto-peptone, 20 g/L glucose, 20 mg/L adenine) and incubated at 25°C for 18-20 hours. Recombinant yeast was harvested by 2-3 min of centrifugation at 3.000 x g and 4°C, followed by 2 times wash in milli-Q water. Harvested cells were incubated in 10% glucose for 10 min, on a shaking table, and centrifuged at 3.000 x g and 4°C. Cells were re-suspended in homogenisation buffer (50 g/L glucose, 28.3% glycerol, 0.1 M Tris-HCl pH 7.25, 10 mM EDTA pH 8.0, 50 mM KCl, 1mM DTT, 200 μM PMSF, 2 μg/ml Pepstatin A), and disrupted with 165 g glass beads (500 μm) by runs in a BeadBeater (Biospec). The disrupted cells were centrifuged at 4°C for 5 and 15 min at 1.400 x g and 12.000 x g, respectively. The supernatant was collected and centrifuged at 251.000 x g for 1 h with 112 μM phenylmethylsulfonyl fluoride (PMSF) and 1.1 μg/mL Pepstatin A. The resulting pellet was re-suspended in $GTEK_{20}$ buffer (20% glycerol, 10 mM Tris-HCl pH 7.25, 25 mM KCl, 0.5 mM EDTA pH 8.0, 1 mM DTT, 0.2 mM PMSF, 2 μg/ml Pepstatin A) and centrifuged for 45 min at 251.000 x g and 4°C. Pellet was then re-suspended in $STKED_{20}$ buffer (200 g/L sucrose, 40 g/L glucose, 50 mM Tris-HCl pH 7.25, 50mM KCl, 1 mM EDTA pH 8.0, 1 mM DTT, 0.2 mM PMSF, 2 μg/ml Pepstatin A), homogenised and diluted with $STKED_{20}$ buffer. The plasma membranes were recovered at the interface of a 43%/53% (wt/wt) step sucrose

gradient containing sucrose in 50 mM Tris-HCl pH 7.25, 50 mM KCl, 1 mM EDTA, 1 mM DTT. Centrifugation was done for 16 h at 154.000 x g and 4°C. The plasma membrane fraction was collected and diluted with $GTEK_{20}$ buffer and centrifuged for 1 hour at 274.000 x g. Pellet was collected and homogenised in $GTEK_{20}$ buffer and stored at -80°C.

Sarco/Endoplasmic reticulum (SR) Ca^{2+}-ATPase was provided in SR membranes purified by extraction with a low concentration of deoxycholate (DOC) as described above. The pig kidney Na^+/K^+-ATPase purification included a mild SDS treatment of isolated microsomes followed by a washing step and was kindly performed by Natalya Fedosova, Aarhus University and prepared as described in (131). In brief, pieces of outer medulla were extracted and cut in pieces and further suspended and homogenized in ISE-buffer (25 mM imidazole, 250 mM sucrose, 1 mM EDTA pH 7.4). Microsomes were isolated by differential centrifugations. The final pellet was suspended and homogenized in ISE-buffer and stored at -20°C.

ATP Hydrolysis Inhibition

ATPase activity was determined by measuring the amount of liberated phosphate from ATP hydrolysis. The ATPase assay was performed in 96 well plates in a final reaction volume of 60 μL. 0.1-0.2 μg/well of DOC extracted SERCA membrane or the Na^+/K^+-ATPase was used, while 1-2.5 μg/well was used of the Pma1 membrane preparation. Reactions including protein membrane preparation and exogenously added compounds in a ½ log dilution concentration range from 333 μM or 166 μM to 0.005 μM. We conducted the enzymatic reactions in the following buffers; Pma1 buffer: 17.5 mM MOPS-NaOH pH 7,7 mM $MgSO_4$, 44 mM KNO_3 (vacuolar ATPase inhibitor), 22 mM NaN_3 (mitochondrial ATPase inhibitor), 0.22 mM Na_2MoO_4 (acid phosphatase inhibitor); SERCA buffer: 9 mM MOPS-NaOH pH 7,

2.7 mM $MgCl_2$, 0.1 mM $CaCl_2$ and 72 mM KCl. Na^+/K^+-ATPase buffer: 30 mM MOPS-NaOH pH 7, 40 mM NaCl, 4 mM $MgCl_2$ and 20 mM KCl. Reactions were started by the addition of Na-ATP to a final concentration of 2.5 mM (Pma1 and Na^+/K^+-ATPase) or 5 mM (SERCA), followed by 30 min incubation at 30°C. The amount of liberated phosphate was determined calorimetrically after addition of STOP solution (mixture of L-ascorbic acid, ammonium heptamolybdate tetrahydrate, and HCl to give final concentrations of 65 mM, 2.2 mM, and 189 mM, respectively) with 5 min incubation at RT followed by addition of arsenite solution (mixture of $NaAsO_2$, sodium citrate dihydrate, and acetic acid to give final concentrations of 3.1 mM, 28 mM, and 141 mM, respectively). We measured absorption at 860 nm after additional 30 min incubation at RT.

Cell Viability, Apoptosis and DNA Content Assays

ATP-based cell viability was determined using the CellTiter-Glo viability assay (Promega Corporation, Madison, WI, USA #G7573) and luminescence was measured using a Victor X4 (Perkin Elmer, Waltham, MA, USA). Apoptotic rate was quantified by staining cells with Annexin V and propidium iodide using a flow-cytometry commercial kit (eBioscience™ Annexin V Apoptosis Detection Kit APC, Waltham MA, USA, # 88-8007-74). Cells were analyzed by flow cytometry with a FACScan flow cytometer (Beckman Culture-Cytomics FC 500, Life Sciences Division, Indianapolis, USA) and FlowJo V10 (Tree Star LLC, Ashland, OR, USA) analytical software. Cellular DNA content was assessed by staining with propidium iodide (50 g/mL) and analyzed by flow cytometry. At least 20,000 events were acquired and all determinations were replicated at least twice.

Cell Competition Assay

SKW-3/KE-37-GFP and MOLT16 were co-cultured at 1:1 ratio in RPMI 1640, 10% FBS, 1% P/S medium. 1 x 10^6 cells per condition were treated with CAD204520 at the following concentrations 2.5 and 5 μM and DMSO at 0.005% and 0.01% respectively and incubated at 37°C. After 72 hours, T-ALL cells were washed in PBS, and stained with a LIVE/DEAD Fixable Far Red Dead Cell Stain (Invitrogen, Life Technologies, Carlsbad, CA, USA, #L34973) for 30 min. Fluorescent signal was assessed by flow-cytometry [Beckman Culture-Cytomics FC 500 (Life Sciences Division, Indianapolis, USA) and FlowJo V10 (Tree Star LLC, Ashland, OR, USA) analytical software]. A minimum of 20,000 events was collected for each biological sample. Experiments are representative of two independent experiments.

Compound Sources

We obtained the compounds for this study from the following sources: DAPT (N-[N-(3,5-difluorophenacetyl)-1-alanyl]-(S)-phenylglycine) (Selleckchem, Houston, TX USA, #S2215), thapsigargin (Enzo Biochem, Inc., USA #BML-PE180-0005), dexamethasone, clobetasol propionate, fluticasone propionate and RU486 were purchased from MedChemExpress EU (MCE) (MedChemTronica, Sweden, #HY-14648; #HY-13600; #HY-B0154; #HY-13683).

Compound Treatment of Cell Lines and Primary Cells

Cells were seeded in 384-well plates (Corning Life Sciences Plastic, Bedford MA, USA, #3570) at the final concentration of 0.02 x 10^6/mL per condition. Small molecules were added with a nanometric dispenser Tecan D300e (Tecan Trading AG, Switzerland), and cellular viability was assessed after 72 hours of drug treatment using a CellTiter-Glo ATP

assay (Promega Corporation, Madison, WI, USA, #G7573). IC50 and the area under the curve (AUC) were calculated using GraphPad Prism software (La Jolla, CA, USA).

Intracellular Calcium Measurement

Cytosolic Ca^{2+} concentration was measured using the Indo-1 AM probe (ThermoFisher Scientific, Waltham MA, USA, #I1223). Cells were washed twice with a calcium free solution (D-PBS Life Technologies, Carlsbad, CA, USA, #10010015) and loaded at 37°C in 5% CO_2 for 30 min with 5 μM of Indo-1 AM. Then, cells were washed twice with D-PBS and equilibrated in RPMI 1640 (Thermo Fisher Scientific, Waltham MA, USA, Waltham MA, USA #MT10040CV) with 10% FBS (Sigma-Aldrich, St. Louis, MO, USA, #F2442-500ML) and 1% penicillin-streptomycin (Thermo Fisher Scientific, Waltham MA, USA, #3MT30002CI) for 5 min at 37°C. Baseline fluorescence of Indo-1 AM loaded cells was acquired for 1 min LSR Fortessa X20 flow cytometer (BD Biosciences, San Jose, CA, USA). Subsequently DMSO (0.1%), CAD204520 1 μM, or thapsigargin 1 μM were added and measurement was resumed for a total of 10 min. Data analysis was performed using FlowJo V10 (Tree Star LLC, Ashland, OR, USA) analytical software.

ER Ca^{2+} release and re-uptake was measured with the IonOptix system (IonOptix, Milton, MA, USA). Ca^{2+} signals were detected by epifluorescence after loading T-ALL cells (ALL/SIL, DND41) with Fluo-3-AM (10 μM; Invitrogen, Carlsbad, CA, USA) in PBS (Gibco, Thermo Fisher Scientific, Waltham, MA, USA) for 20 min, at RT. After removing the fluorophore, cells were washed with PBS for 30 min and then placed ($1x10^6$; 1ml volume) in a chamber mounted on the stage of an inverted microscope (Nikon-Eclipse TE2000-U, Nikon Instruments, Florence, Italy). The recording started with measurement of baseline fluorescence. Then, 1 μM CAD204520, 1 μM thapsigargin, or DMSO (0.1%) were manually

added with a pipette, and the recording was continued for up to 15 min (during the first 7 min: 5 seconds of recording followed by 5 seconds of rest; in the remaining 8 min: 5 seconds of recording followed by 30 seconds of rest). Excitation length was 480 nm, with emission collected at 535 nm. The following parameters were evaluated: (i) peak fluorescence normalized to baseline fluorescence (f/f0_peak), (ii) time at 50% of fluorescence signal decay, measured from the peak time (time_50%-f/f0), and normalized fluorescence computed at 3, 5, and 10 min from the peak time (f/f0_3min, f/f0_5min, and f/f0_10 min).

Western Blot

Protein lysates for western blotting were incubated with antibodies specific for g-secretase-cleaved NOTCH1 (Val1744, #4147 or #2421 Cell Signaling, Beverly, MA, USA) or the C-terminus of NOTCH1 (#SC-6014 (C-20), Santa Cruz Biotechnology, Santa Cruz, CA, USA). Cleaved form of Poly (ADP-ribose) polymerase was detected using an antibody specific for the cleaved peptide of PARP (#9541, Cell Signaling, Beverly, MA, USA). The expression of SERCA isoforms in ALL/SIL were detected using SERCA2 (#9580, Cell Signaling, Beverly, MA, USA) and SERCA3 (#sc-81759, Santa Cruz Biotechnology, Santa Cruz, CA, USA) antibodies while glucocorticoid receptor expression was detected using Glucocorticoid Receptor (D8H2) XP antibody (#3660; Cell Signaling, Beverly, MA, USA. Loading controls were performed with antibodies specific for β-Actin, (#BK3700S, Cell Signaling, Beverly, MA, USA), GAPDH (#137179, Santa Cruz Biotechnology, Santa Cruz, CA, USA) or HSP90 (# sc-69703 (4F10)), Santa Cruz Biotechnology, Santa Cruz, CA, USA). Effects on the endoplasmic reticulum stress pathway (ER stress) we used the following antibodies: BiP, (#BK3177S), phospho-eIF2α (Ser51) (#9721S), eIF2α (#9722S) (Cell Signaling, Beverly, MA, USA). Blots were developed using species specific fluorescent antibodies obtained from

LI-COR (Biosciences, Lincoln, NE, USA) such as IRDye 680LT Goat anti-Mouse IgG (#925-68020); IRDye 800CW goat anti-rabbit IgG (#925-32211); IRDye 680RD goat anti-rabbit IgG (#925-68071). Cell surface NOTCH1 was evaluated by staining non-permeabilized cells with monoclonal anti-human NOTCH1 antibody (#FAB5317P, R&D, Minneapolis, MN, USA).

Indirect Immunofluorescence Microscopy

DND41, REC-1 and ALL/SILL cells were resuspended in PBS, spotted on immunofluorescence slides (Thermo Fisher Scientific, Waltham, MA) by a cytospin centrifuge (CR2000, Small Prime Centrifuge, Centurion) fixed for 10 min in 4% paraformaldehyde (#28908, Thermo Fisher Scientific, Waltham MA, USA), permeabilized in 0.2% Triton X-100 for 5 min, and blocked in 5% bovine serum albumin for 1 hour. Then, the cells were incubated with primary antibodies against full length NOTCH1 (#SC-6014 (C-20) Santa Cruz Biotechnology, Santa Cruz, CA, USA or #ab44986 (A6) Abcam, Cambridge, United Kingdom), GOLGA1 (#SAB1409131, Sigma-Aldrich, St. Louis, MO, USA), and ATF6 (#37149, Abcam, Cambridge, United Kingdom). Alexa Fluor 488 (#A11029, Invitrogen, Carlsbad, CA, USA) and Alexa Fluor 568 (#A11036, Invitrogen, Carlsbad, CA, USA) were used as secondary antibodies and cells were incubated 1 hour at RT protected by the light. Nuclei were stained with DAPI (#D9542, Sigma-Aldrich, St. Louis, MO, USA). Coverslips were mounted with Prolong Gold Antifade reagent (#P36934, Thermo Fisher Scientific, Waltham MA, USA). Images were captured using a EVOS FL microscope (Thermo Fisher Scientific, Waltham MA, USA) and analyzed using ImageJ software (http://rsbweb.nih.gov/ij/).

Real-time RT-PCR

Primers and probes for real-time RT-PCR were obtained from Applied Biosystems (Foster City, CA, USA) (*RPL13A* #Hs01926559_g1, *MYC* #Hs00153401_m1, *DTX1* #Hs00269995_m1). Primers and probes used for glucocorticoid receptor quantitative RT-PCR were obtained from Thermo Fisher Scientific (Waltham MA, USA) as following. For human GR alpha, forward primer: GAG-GAA-GTT-ATC-CTCTGC-CTC; reverse primer: TGT-AAG-CAC-CAC-CTTCCT-GTC-T; probe: 6FAM-TTC-CAA-CAG-TGA-GTCTGT-CAG-CGC-A-QSY; for human GR beta, forward primer: GCT-GGA-TAA-TTA-GCA-TGG-GAT-G; reverse primer: AAT-TGC-TCC-CTG-CCT-CTG-A; probe: 6FAM-ATGAAG-GAA-AGC-CAC-GCT-CCC-T-QSY. The data were analyzed using the $\Delta\Delta$CT method and plotted as percentage of transcript compared to vehicle. Values were considered statistically significant at $P < 0.05$.

Whole Exome Sequencing

DNA was extracted from about 10 x 10^6 ALL/SIL o ALL/SIL thapsigargin resistant using a Promega Maxwell™ kit as per the manufacturer's protocol (Promega Corporation, Madison WI, USA, #AS1010). A total amount of 1.0 μg genomic DNA per sample was used as input material for the DNA library preparation. Sequencing libraries were generated using Agilent SureSelect Human all exon kit (Agilent Technologies, CA, USA) following manufacturer's recommendations and index codes were added to each sample. Briefly, fragmentation was carried out by hydrodynamic shearing system (Covaris, Massachusetts, USA) to generate 180-280bp fragments. Remaining overhangs were converted into blunt ends via exonuclease/polymerase activities and enzymes were removed. After adenylation of 3' ends of DNA fragments, adapter oligonucleotides were ligated. DNA fragments with ligated

adapter molecules on both ends were selectively enriched in a PCR reaction. After PCR reaction, library hybridizes with liquid phase with biotin labeled probe, after which streptomycin-coated magnetic beads are used to capture the exons of genes. Captured libraries were enriched in a PCR reaction to add index tags to prepare for hybridization. Products were purified using AMPure XP system (Beckman Coulter, Beverly, USA) and quantified using the Agilent high sensitivity DNA assay on the Agilent Bioanalyzer 2100 system and sequenced with Hiseq PE 150 (Illumina®, San Diego, CA, USA). Paired-end clean reads were aligned to the reference genome (hg38) with Burrows-Wheeler aligner (B.W.A.). SAMtool was used to sort and index the original BAM files and Picard marked duplicates reads. Coverage and depth were calculated based on the final BAM files. If a read or reads pair were mapped to multiple positions, B.W.A. will choose the most likely position. If two or more likely position were present B.W.A. will choose one randomly. This multiple hit strategy has significant impact on SNP, INDEL and CNV detection, and variant calling accuracy. Following genomic variant detection, we performed annotation of variants with the tool ANNOVAR (132) in multiple aspects, including protein coding changes, affected genomic regions, allele frequency etc.

Virus Production and Transduction of T-ALL Cell Lines

3 x 10^6 293T were plated in 10 cm plates and maintained in DMEM media (Life Technologies, Carlsbad, CA, USA, #11965118), 10% FBS (Sigma-Aldrich, St. Louis, MO, USA, #F2442-500ML), 1% penicillin-streptomycin (Thermo Fisher Scientific, Waltham MA, #3MT30002CI) and incubated at 37°C with 5% CO_2, until sub confluent. Cells were transfected with 2 μg of pCMV-VSV-G envelope vector, Delta 8.9 packaging plasmid and pXPR-011-GFP, a vector expressing a green fluorescent protein (GFP), according to the

FuGENE 6 protocol (Promega Corporation, Madison WI, USA, #E2691). The tissue culture medium was changed to RPMI 1640 24 hours post-transfection, and viral supernatant was harvested and filtered (0.2 μm) 48 hours post-transfection. 4 x 10^6 SKW-3/KE-37 T-ALL cells were resuspended in 100 μL of RPMI 1640 and spin-infected for 1 hour at 37°C with 100 μL lentivirus particles and 8 μg/mL polybrene (Sigma-Aldrich, St. Louis, MO, USA). Cells were selected 48 hours later with 1 μg/mL puromycin (Sigma-Aldrich, St. Louis, MO, USA).

Cardiomyocyte Isolation and Treatment

Individual left ventricular (LV) myocytes were enzymatically isolated by collagenase perfusion, following a procedure previously described (133). Briefly, after sacrifice, the rat heart was rapidly removed, mounted on a Langendorff apparatus and perfused at 37°C with the following sequence of solutions: solution 1: calcium-free solution for 5 min containing the following (expressed in mM/L): 126 NaCl, 22 dextrose, 5.0 $MgCl_2$, 4.4 KCl, 20 taurine, 5 creatine, 5 Na pyruvate, 1 NaH_2PO_4, and 24 HEPES (pH = 7.4, adjusted with NaOH); solution 2: solution 1 plus 0.1 mM Ca^{2+}, 1 mg/ml type 2 collagenase (Worthington Biochemical, USA), and 0.1 mg/ml type XIV protease (Sigma, Milan, Italy) for about 15 min, and solution 3: solution 1 plus 0.1 mM Ca^{2+} (enzyme-free) for 5 min. All solutions were gassed with 100% O_2. Afterward, the LV was minced and shaken for 5 min. The cells were filtered through nylon net and re-suspended in the low calcium solution for 30 min, then slowly brought to a final calcium concentration of 1 mM (maintenance solution).

A total of 8 rats (male) were scarified for these experiments. Specifically, cardiomyocytes isolated from the heart of 6 rats were either untreated (Control group) or incubated with 5 μM CAD204520 for 2 hours ($CAD204520_{2hr}$) or 4 hours ($CAD204520_{4hr}$) and then used for recording cell mechanics (IonOptix, Milton, MA, USA) (133, 134). Cardiomyocytes isolated

from additional 2 rats were incubated with thapsigargin, at two different concentrations, 200 nM or 500nM for 2 hours and then submitted to the same experimental protocol (Control number of cells n=63; $Thapsigargin_{200nM}$, n=28; $Thapsigargin_{500nM}$; n=25. Left ventricular myocytes were placed in a chamber mounted on the stage of an inverted microscope (Nikon-Eclipse TE2000-U, Nikon Instruments, Florence, Italy) and superfused (1 mL/min at 37°C) with a Tyrode solution containing (in mM): 140 NaCl, 5.4 KCl, 1 $MgCl_2$, 5 HEPES, 5.5 glucose, and 1 $CaCl_2$ (pH 7.4, adjusted with NaOH) (Sigma-Aldrich, Milan, Italy). The cells were field stimulated at a frequency of 0.5 Hz by constant current pulses (2 milli seconds in duration, and twice diastolic threshold in intensity; MyoPacer Field Stimulator, IonOptix). Load-free contraction of myocytes was measured with the IonOptix system, which captures sarcomere length dynamics via a Fast Fourier Transform algorithm. The following parameters were computed: mean diastolic sarcomere length, fraction of shortening (FS), and the maximal rates of shortening (-dl/dtmax) and re-lengthening (+dl/dtmax). Steady-state contraction of myocytes was achieved before data recording by means of a 10 seconds conditioning stimulation. Sampling rate was set at 1 kHz. In a fraction of cells from each experimental group, calcium transients were measured simultaneously with cell motion, after loading the myocytes with Fluo-3 AM (10 μmol/L; Invitrogen, Carlsbad, CA, USA) for 30 min. Excitation wavelength was 480 nm, with emission collected at 535 nm. Fluo3 signals were expressed as normalized fluorescence (f/f0: fold increase). The time course of the fluorescence signal decay was described by a single exponential equation, and the time constant (Tau) was used as a measure of the rate of intracellular calcium clearing. Only rod-shaped myocytes exhibiting cross striations and no spontaneous contractions were selected for physiological measurements. Cardiomyocyte subgroups were washed three times with low-calcium solution and centrifuged (42 x g for 5 min). After removing the supernatant, the pellet was stored at -80°C for intracellular ATP content detection (as described below).

Intracellular ATP Content Detection

The intracellular content of ATP was measured by the luminescence ATP-lite assay (PerkinElmer, Waltham, MA, USA, #6016943) according to the manufacturer's protocol, using an EnSpire™ multimode plate reader (PerkinElmer, Waltham, MA, USA). Briefly, a frozen pellet of cardiomyocytes (both untreated or incubated with 5 μM CAD204520 for 2 or 4 hours) was re-suspended in 1 mL of PBS, and then 20 μL of this suspension were further diluted 20 times in PBS. 100 μL of each diluted sample were lysed and assayed for ATP content in triplicate, as previously detailed (134). The row luminescence data were normalized for the total protein content measured by the DC Protein assay kit (Bio-Rad, Hercules, CA, USA).

***In Vivo* Studies**

In brief 6 male, 7-9 weeks old CD1 (ICR) in-house breed mice (Aurigene, India) were treated with 30 mg/Kg/diem CAD204520 in fed state by oral gavage dissolved in Tween-80 0.5% w/v (Sigma-Aldrich, Missouri, USA) and hydroxypropyl-methylcellulose (HPMC) 1.0% w/v (Shin-Etsu Chemical Co., Tokyo, Japan) to model PK and biodistribution data. Samples from the plasma and brain were collected at eight time points (5 min to 24 hours). CAD204520 concentration was assessed by LC/MS-MS method and PK parameters (Tmax, Cmax, T1/2, AUC, etc.) were calculated with Analyst 1.6.1 software using a one-compartment model. Lambda Z PK parameters was reviewed by LD ADME consult (Copenhagen, Denmark) to model multiple doses PO infusion and time-concentration data. For tolerability studies, 6-8 weeks BALB/cAnNCr mice per group (3 male and 3 female) were treated BID with 30 mg/Kg CAD204520 or vehicle (see above) by oral gavage at 8 hours interval. CAD204520 and

vehicle were administered from day 1 to day 21 by oral route. Daily body weight measurement before dosing and adverse events were recorded. Animals were sacrificed on day 21. In a subsequent experiment, 6 BALB/cAnNCr mice per group (3 male and 3 female) were treated with 30 mg/Kg CAD204520 (BID) for 7 days and for the remaining of the study (day 7 to day 21) with 60 mg/Kg (BID).

To generate *NOTCH1*-dependent T-ALL tumors in mice, 10 x 10^6 SKW-3/KE-37 cells were transplanted via the retro-orbital venous sinus in adult (10-12 weeks old) non-irradiated NSG mice (day 0) (118). Once disease was established at day 12 after transplant, animals were divided into two treatment groups of eight mice each (3 male and 5 female): vehicle [tween-80 0.5% w/v (Sigma-Aldrich, Missouri, USA) and hydroxypropyl-methylcellulose (HPMC) 1.0% w/v (Shin-Etsu Chemical Co., Tokyo, Japan)] or 30 mg/kg BID of CAD204520. Animals were treated with either vehicle or CAD204520 at 30 mg/kg BID (PO) for 4 days. Antileukemic activity of CAD204520 was assessed by measuring human CD45+ expression (clone HI30, BD Biosciences, New Jersey, USA) on peripheral blood blast cells by flow cytometry (FACS CANTO, BD Biosciences, San Jose, CA, USA) and by quantification of hCD45+ cells in formalin-fixed, paraffin-embedded spleen sections [(clones 2B11 + PD7/26 Dako, Agilent, Stevens Creek Blvd Santa Clara, CA, USA)]. Complete blood count was performed using an XE-2100 hematology automated analyzer (Dasit). Formalin-fixed, paraffin-embedded heart and gut sections were stained using hematoxylin and eosin. Images were acquired at different magnifications using a Leica DM750 microscope (Leica Microsystems, Wetzlar, Germany).

Small molecule screening assay

Human T-ALL cell lines ALL/SIL and ALL/SIL R were screened with the European Chemical Biology Library (ECBL), provided by EU-OPENSCREEN. The 2465 biologically active compounds were used at 100 nM and 1 μM concentrations. Etoposide was used as positive control, dimethyl-sulfoxide (DMSO) as negative control. Thapsigargin was tested at 100 nM and 1 μM concentration as positive control for ALL/SIL cell line. CAD204520 was tested at 1 μM and 10 μM concentration as rescue treatment for ALL/SIL R. The base medium for both cell lines was 90% RPMI 1640, 10% heat inactivated FBS, 1% penicillin-streptomycin and 2 mM L-Glutamine. After 72 hours incubation, a resazurin fluorescence method was used as viability assay and presented as a percentage of viable cells over control (POC).

Quantification and Statistical Analysis

Assumption of normal distribution was not determined, and P-value was calculated by non-parametric t-test (Mann-Whitney) by comparing treated samples to untreated controls. Significance across groups was determined by one-way or two-way ANOVA using Bonferroni correction for multiple comparisons testing when appropriate. Statistics were performed using GraphPad Prism software. Graphs show means and standard deviation (±SD) as indicated in the figure legends. Statistical significance, group size, and experimental details are described in the figure legends and/or in Materials and Methods section.

RESULTS

Identification of CAD204520 as a Selective Ca^{2+} ATPase Inhibitor

P-type ATPases are a group of evolutionarily conserved proteins that transport a variety of charged substrates, such as H^+, Na^+, K^+, Ca^{2+}, Zn^{2+}, and Cu^+ or phospholipids across membranes (135). Because P-type ATPases control active ion transport across cellular membranes, their altered activity is associated with the development of pathophysiological conditions, including cardiovascular, neurological, renal, and metabolic diseases. Consequently, P-type ATPases are compelling therapeutic targets. For example, the cardiac Na^+/K^+-ATPase inhibitor, digoxin (136), and gastric H^+, K^+-ATPase inhibitor, omeprazole (137), are among the most clinically successful therapeutics in this target class (138).

In recent years, P-type ATPases (e.g., SERCA) have emerged as potential dependencies in cancer (139) and as mediators of chemotherapy resistance in solid tumors (140, 141). Their importance for cell survival has furthermore sparked an interest in inhibiting P-type ATPases of pathogenic fungi and bacteria (142). To identify potent P-type ATPase inhibitors in this context, Kjellerup et al. screened a library containing nearly 191,000 compounds for inhibition of the fungal H^+-ATPase (143). A total of 407 compounds inhibited ATP hydrolysis activity of the H^+-ATPase by greater than 50% and were subsequently counter-screened for P-type ATPase specificity, by testing their effect on mammalian SERCA (rabbit SERCA1a, which shares 96.6% protein similarity with human SERCA orthologs) and pig Na^+/K^+-ATPase (143-145) (Figure 4A).

The initial hit compound, 2-(2-pyridyl)-6-(trifluoromethoxy)-1H-indole (Figures 4BI, and S1A), was a weak inhibitor of SERCA ATPase (half maximal inhibitory concentration [IC50] = 236 μM) but with an attractive low molecular weight. An extensive exploration of the chemical space occupied by the pyridine core was performed through a systematic

replacement with commercially available alternative heteroaromatic and heterocyclic systems, as well as pyridines substituted with small functional groups capable of picking up polar interactions. As a result, the piperidine analog 2-(2-piperidyl)-6-(trifluoromethoxy)-1H-indole (Figure 4BII) was identified as the minimum pharmacophore with improved SERCA ATPase potency, selectivity against Na^+/K^+-ATPase, and a reasonable ligand efficiency of 0.28. Options for diversity in substitution of indole C4-C7 were limited and C6-OCF3 was ‘‘locked’’ to continue exploration of more promising points of substitution. Furthermore, indole N1 had been extensively explored in a closely related chemical program with an overlapping pharmacophore, and for reasons of concern about target selectivity it was decided not to explore the indole N1 chemical space with the identified compound II. Conversely, compound II was explored in R^1 of the indole system and R^2 of the piperidine system (Figure S1B) for reasons detailed below.

Compounds with substitution on piperidine N1 (R^2) with R^1 = H were subsequently produced and, among them, CAD204522, CAD307496, and CAD204521 (Figure 4B) showed various degrees of Ca^{2+}-ATPase activity (Table S1). Interestingly, CAD204521 (Figure 4BIII; Table S1) was closely related to a previously reported potent fungal H^+-ATPase inhibitor, Compound 7 (144). Similarly to Compound 7, CAD204521 showed an improved potency against Ca^{2+} ATPase but not a desired selectivity or drugability profile. Because indole C3 had the potential to provide Ca^{2+}-ATPase selectivity, we decided to explore indole R^1 with R^2 = p-bromobenzyl (derivatives of CAD204521, Figure 4BIV). For example, CAD204519 was by far the most potent inhibitor of Ca^{2+}-ATPase; however, with an unfavorable Na^+/K^+ Ca^{2+} selectivity. Nevertheless, substitutions with certain hydrophilic groups on the R^2 on piperidine N1 (Figure 4B; Table S1, CAD306750, CAD306749, and CAD204520) increased the selectivity toward mammalian SERCA.

Notably, CAD204520 (Figure 4BV and S1C) preferentially inhibited the Ca^{2+}-ATPase by reducing its ATP hydrolysis activity with an IC50 of 0.34 ± 0.03 μM as compared with Na^+/K^+-ATPase (IC50 = 8.30 ± 0.94 μM) and H^+-ATPase (IC50 = 26.90 ± 2.98 μM) (Figure S1D; Table S1). Furthermore, CAD204520 displayed the overall most promising drug properties of the synthesized compounds with a calculated LogP of 4.4 and $LogD_{7.4}$ of 2.2 (ACD/Labs 18.1.1). This compound was thus selected for further studies as a selective SERCA inhibitor.

To assess the binding mode of CAD204520 to SERCA, we then crystallized it in complex with SERCA and determined the crystal structure at 3.4 Å resolution. The crystals were of the same space group as previously reported thapsigargin-bound SERCA (PDB: 2AGV), and the overall conformation of SERCA bound to CAD204520 is very similar to the thapsigargin-bound form. The CAD204520 ligand binds to a groove at the membrane interface of SERCA, between transmembrane helices M1, M2, M3, and M4 (Figures 4C and 4D), with two polar interactions to Asp^{59} on M1 (2.9 Å) and Asn^{101} on M2 (2.7 Å), and with several hydrophobic interactions involving Leu^{61}, Val^{62}, Ile^{307}, Pro^{308}, and Pro^{312} (Figure 4C). Interestingly, the CAD204520 binding groove is different from that of thapsigargin (Figure S1E), but similar to the binding of other SERCA inhibitors, such as CPA (6) (Figure S1F) and 2,5-di-t-butyl-1,4-benzohydroquinone (DBHQ) (28) (Figure S1G), and to that of the Compound 7 previously reported by Bublitz et al. (144) (Figure S1H). In fact, the indole system (core structure) of CAD204520 superposes very closely on the tetrahydrocarbazole core of Compound 7, including the central interaction of the indole N1 nitrogen with Asp59. The morpholinoethyl group, interacting with Asn^{101}, occupies the same space as one of the two alternative positions found for the bromophenyl moiety of Compound 7 (Figure S1H). In contrast to Compound 7, however, there is no interaction with Asp^{245}. Despite this similarity, CAD204520 does not induce the same overall SERCA conformation as Compound 7, but a

conformation almost identical to thapsigargin-inhibited SERCA. The thapsigargin-binding site lies adjacent to the CAD204520 site, separated by M3 (Figure S1I).

Collectively, these data show that CAD204520 selectively binds SERCA in the same binding pocket as DBHQ, CPA, and Compound 7. This pocket has been identified as the pathway for Ca^{2+} ion entry into the pump from the cytosolic side of the membrane (29), and compound binding at this site locks SERCA in a Ca^{2+}-free (so-called *E2*) conformation.

CAD204520 Rescues T-ALL Cells from Thapsigargin Resistance

SERCA can be inhibited by different small molecules, such as thapsigargin, DBHQ, 1,3-dibromo-2,4,6-tris (methyl-isothio-uronium) benzene, and CPA. These compounds have specific binding sites in the ATPase protein and hence different inhibitory mechanisms (146). A first question is whether CAD204520 binding to SERCA mimics thapsigargin ATPase inhibitory kinetics or, rather, the two molecules act independently as predicted by structural data.

To test our hypothesis, we took two different approaches. First, we generated a T-ALL cell line (ALL/SIL) resistant to thapsigargin (ALL/SIL R) by selecting cells growing under increasing concentration of this molecule. At approximately days 90, 120, and 150, T-ALL cells displayed 2-, 10-, and 27-fold increased IC50 values, respectively (Figure S2A). To rule out that this drug resistance was mediated by altered expression of the target, we demonstrated that naive and resistant cell lines showed similar levels of SERCA2 and SERCA3 proteins (Figure S2B). To evaluate for thapsigargin-induced gene mutations within the *ATP2A1–3* genes, we performed whole-exome sequencing and limited our analysis to single-nucleotide exonic missense variation with a Phred-scaled quality score >30 (standard error = 1/1,000 = 0.1%; accuracy 99.9%) (Figure S2C). Previous work had demonstrated

that mutations occurring in the third stalk (M3) segment of SERCA determine the sensitivity of ATPase to thapsigargin (26, 147, 148). In particular, mutations in the M3 segment between Asp^{254} and Leu^{260} increase the thapsigargin concentrations required for inhibiting SERCA by more than three orders of magnitude (148, 149) (Figure S2D). Interestingly, in ALL/SIL R cells we identified, within the Asp^{254}-Leu^{260} hotspot, a missense single-nucleotide polymorphism occurring in *ATP2A2* exon 8 (c.G770T) caused a glycine257/valine mutation in the M3 helix (Figures 5A and S1I highlighted in red). No mutations occurred in *ATP2A1* (Figure 5A, top panel), while missense mutations in *ATP2A3* were present both in the naive and resistant lines, indicating a pre-existing mechanism of allelic variance (Figure 5A, bottom panel). Similarly, no acquired mutations were identified in *SEC24A*, a gene involved in ER-Golgi protein trafficking and previously identified as an essential mediator of thapsigargin-induced cell death in a genome-wide CRISPR/Cas9 screen in HAP1 cancer cells (150). According to our crystal structure, Gly^{257} faces a hydrophobic part of CAD204520 at a distance that could probably accommodate a valine residue without interfering with CAD204520 binding (Figure S1I). The introduction of the bulky valine side chain will, however, very likely limit the freedom of movement of the neighboring residue Phe^{256}, which has to swing sideways to accommodate thapsigargin binding (Figures S1E and S1I), thus providing a potential explanation for the resistance effect.

Next, we treated ALL/SIL naive and resistant cells at ALL/SIL IC50 (as shown in the following sections) concentrations and demonstrated that $G^{257}\rightarrow V$ rescues ALL/SIL cells from thapsigargin-induced cytotoxicity while it does not interfere with CAD204520 effects (Figure 5B). Accordingly, because CAD204520 binds to SERCA in a pocket similar to that of CPA but distinct to that of thapsigargin, we anticipated that the combined inhibition might result in a synergistic effect with thapsigargin but not with cyclopiazonic acid. To avoid the

limitations and biases associated with any one algorithm used to study drug-drug interactions, we used comprehensive approaches, including the Loewe additivity model, the Chou and Talalay index, and the Bivariate Response to Additive Interacting Doses (BRAID) analysis. The Loewe additivity is a commonly used dose-effect-based model to quantify a zero-interactive state for the combination of two drugs (151). The Chou-Talalay method (152) for drug combination is based on the median-effect equation and provides a mechanism-independent method for quantitative determination, combination index (CI), of drug interactions. A CI ranging from 0.9 to 1.1 is considered additive, a CI < 0.9 indicates synergy, and a CI > 1.1 resistance. Finally, we used a response surface method, the BRAID model of combined action (153, 154). A κ BRAID index > 0 shows synergy between the compounds tested. Unlike most methods that reduce combination analysis to a simple decision between synergy, additivity, and antagonism, surface models use non-linear optimization to fit a response surface model to the effects of combined compounds. We tested CAD204520 and thapsigargin both individually and in combinations at the indicated concentrations for a total of 60 combinatorial points in T-ALL cell lines and in primary *NOTCH1*-mutated T-ALL samples. We found that simultaneous exposure to CAD204520 and thapsigargin for 72 h resulted in a robust synergistic inhibition of cell viability in T-ALL cells. Loewe, CI, and BRAID models established a synergistic effect at low-dose combinations and support the notion that CAD204520 binds at a site within SERCA that is distinct from the thapsigargin-binding sites (Figures 5C–5E). Consistent with our hypothesis, combined CAD204520 and CPA treatment did not demonstrate the same degree of synergistic activity (Figure S2E).

Collectively, these data indicate that G257V mutation in the M3 helix of SERCA do not interfere with CAD204520 activity and that a greater anti-leukemia effect may be achieved

by the simultaneous binding of CAD204520 and thapsigargin to their respective sites in SERCA.

CAD204520 Suppresses Leukemia Growth in *NOTCH1*-Mutated T-ALL and MCL

We previously demonstrated that SERCA inhibitors decrease T-ALL growth both in vitro and in vivo (75). To validate CAD204520 as a potential modulator of Notch-dependent cancers we initially tested the effect of CAD204520 in a panel of T-ALL or MCL cell lines that contain activating mutations in the HD of *NOTCH1* and/or deletions in the degradation domain (PEST) (Figure S3A). *NOTCH1*-mutated T-ALL (Figure 6A) (ALL/SIL, CTV-1, DND41, PF382, and RPMI-8402) or MCL cell lines suppressed by GSI (REC-1) (Figure 6B) (91) were more sensitive to CAD204520 as measured by inhibition of cell viability compared with *NOTCH1* wild-type tumor cells (Figures S3B and S3C). Seventy-two hours of CAD204520 treatment triggered concentration-dependent apoptosis as determined by the increase of Annexin V/PI+ cells (Figure 6C) and the cleavage of PARP proteins (Figure 6D).

An additional phenotypic consequence of NOTCH1 inhibition with GSI is that T-ALL cells undergo cell-cycle arrest (91). As shown in Figure 6E, CAD204520 induced a G0/G1 arrest preferentially in *NOTCH1*-mutated tumors (Figure S3D), and together with the data described above it supports the notion that CAD204520 inhibits lymphoid-derived cancer cells carrying clinically relevant *NOTCH1* HD or PEST mutations.

CAD204520 Suppresses Notch1 Signaling

NOTCH receptors undergo several processing events, including a first cleavage by a furin-like convertase (S1) in the *trans*-Golgi network that generates full-length heterodimers (155, 156) ready to be conveyed to the plasma membrane (157). The correct folding of these

heterodimers requires Ca^{2+} that, in physiological condition, is tightly regulated across the ER storage by SERCA (68).

To support the hypothesis that CAD204520-mediated SERCA inhibition impairs mutant NOTCH1 maturation, we evaluated the expression of NOTCH1 full-length and transmembrane portions of CAD204520-treated cells by western blotting. Lysates from T-ALL cell lines treated with 5 μM CAD204520 for 24 h were immunoblotted with an antibody specific for the cytoplasmic portion of NOTCH1 that recognizes both unprocessed NOTCH1 (FL-N1) (270 kDa) and the furin-processed transmembrane subunit (TM-N1) (110 kDa). CAD204520 reduced the levels of the furin-processed transmembrane NOTCH1 subunit, but not the unprocessed full-length NOTCH1 precursor, in multiple T-ALL cell lines (Figure 7A). As expected from our structural data, combined CAD204520 and thapsigargin treatment resulted in an enhanced reduction in ICN1 and TM-NOTCH1 levels (Figure S4A).

In addition, we demonstrated that treatment of T-ALL with CAD204520 resulted in a concentration-dependent decrease in NOTCH1 expression on the cell surface by flow cytometry (Figure 7B). As expected, we did not observe this effect with a known GSI Notch inhibitor N-[N-(3,5-difluorophenacetyl)-1-alanyl]-(S)-phenylglycine (DAPT). Consistent with our hypothesis that CAD204520 affects NOTCH1 maturation rather than expression, NOTCH1 only decreases at the surface of the cells upon CAD204520 treatment but co-localizes at the ER-Golgi intermediate compartment as shown by immunofluorescence co-localization studies (Figures 7C and S4B–S4E). An immediate consequence of the decrement in NOTCH1 on the surface of the cells is the reduction of the catalytic activity of the γ-secretase complex because of the lack of NOTCH1 substrate. Here, we would expect a reduction in the level of ICN1. Indeed, CAD204520 ultimately leads to loss of ICN1 (Figure 7D) and results in the suppression of NOTCH1 target genes *MYC* and *DTX1* as measured

by RT-PCR (Figure 7E). Furthermore, testing CAD204520 in MCL *NOTCH1*-mutated cells yielded results comparable with the one described in T-ALL, suggesting a conserved mechanism across different *NOTCH1*-mutated cancers (Figure S4D-F).

In summary, these data show that CAD204520 inhibits Notch1 maturation, demonstrating that SERCA inhibitors with a binding mode different from thapsigargin can efficiently suppress NOTCH1 maturation.

CAD204520 Preferentially Inhibits *NOTCH1*-Mutated Cancers

SERCA inhibitors increase the Notch therapeutic index by targeting clinically relevant *NOTCH1* mutations in leukemia cells (75, 119, 158). In fact, leukemia cells carrying *NOTCH1* alleles with HD mutations are more sensitive to SERCA inhibition than cells with wild-type *NOTCH1* alleles (75, 119).

To verify the hypothesis that CAD204520 preferentially targets mutant *NOTCH1*, we used two T-ALL cell lines carrying the same t(8; 14) (q24; q32)/*TRAD@-MYC* translocation but different Notch mutational status (Figures 8A and S5A). SKW-3/KE-37 harbors an isolated *NOTCH1* mutation in the PEST domain, while MOLT16 is *NOTCH1* wild type (91, 159). First, we determined that the mutant T-ALL cell line was more sensitive to CAD204520 growth inhibition as measured by an ATP-based cell viability assay (Figure S5B). To validate this observation, we established a flow cytometry-based competition assay. SKW-3/KE-37 were transduced with a GFP lentiviral expressing vector and co-cultured with MOLT16 T-ALL cells in a 1:1 ratio. Next, we treated SKW-3/KE-37-GFP and MOLT16 cocultured cells with increasing concentrations of CAD204520 and demonstrated that the mutated T-ALL cell line, SKW-3/KE-37-GFP, was more sensitive to growth suppression compared with wild-type MOLT16, as quantified by flow cytometric analysis of alive versus dead cells (Figure

8B). Analysis of caspase-3 and -7 activities indicates that the *NOTCH1* mutational status sensitizes cells to CAD204520-mediated apoptotic cell death (Figure 8C). Consistent with the hypothesis that SKW-3/KE-37 relies on Notch signaling for growth and survival, we observed a decrement of NOTCH1 protein only in mutant T-ALL cells compared with wild-type cells (Figure 8D).

To further support the preclinical development of CAD204520, we tested it (dose range = 0.6–8 μM) in a collection of T cell lymphoblasts isolated from T-ALL patients. As shown in Figure 8E, CAD204520 preferentially affects T-ALL viability compared with normal lymphocytes. Primary blasts, derived from a patient suffering from a *NOTCH1*-mutated T-ALL, exposed to 5 μM CAD204520, rapidly underwent apoptosis (Figure S5C). In addition, T-ALL primary cases for which we confirmed a *NOTCH1* mutation (no. 1 *NOTCH1* ex 27, c.5101G > C p.A1701P; no. 2 *NOTCH1* ex 26, c.4793G > C p.1598P and *FBXW7* ex 9, c.1514G > T p.R505L) were more sensitive to CAD204520 compared with *NOTCH1* wild-type B cell ALL (Figure 8F).

Collectively, these results indicate that CAD204520 retains anti-tumor activity preferentially in cells carrying *NOTCH1* alleles with HD or PEST mutations, holding great promise for CAD204520 future development against this indication.

Consequences of Ca^{2+} Release upon CAD204520 Treatment

A consequence of SERCA inhibition is the rise of intracellular Ca^{2+} followed by the depletion of Ca^{2+} stored in the ER. ER Ca^{2+} exhaustion triggers a number of secondary events, including the activation of the unfolded protein response (UPR) pathway (160), the activation of store-operated Ca^{2+} entry (161), and ultimately cell death (162).

To quantify the consequences of CAD204520 or thapsigargin treatment at the level of cytosolic Ca^{2+}, we transferred ALL/SIL or DND41 in Ca^{2+}-free media and loaded with Indo-1 a ratiometric sensitive indicator fluorescent dye for measuring intracellular Ca^{2+}. As shown in Figure 9A compared with DMSO, CAD204520 slightly increases cytosolic Ca^{2+}. However, if compared with the thapsigargin effect, the extent of the increase appears modest with broad and flat peaks. In fact, thapsigargin causes a sharp rise in Ca^{2+} concentration at ~ 200 s upon drug injections. The next question is whether SERCA is still able to re-load Ca^{2+} from the cytosol inside the ER upon CAD204520 treatment. This hypothesis would explain why the increase of Ca^{2+} upon CAD204520 treatment is moderate and why thapsigargin triggers delayed on-target Ca^{2+} effects such as UPR activation and apoptosis (163). In this case we used a different approach and measured Ca^{2+} Fluo-3 AM epifluorescence using an IonOptix system. This approach is ideal to measure fluctuations of ER Ca^{2+}. As reported in Figure 9B, the peak fluorescence (f/f0_peak) was similar in the three groups of cells, indicating that the different compounds did not modify the Ca^{2+} release from the ER. Conversely, the fluorescence signal decay was significantly prolonged in thapsigargin-treated cells in comparison with both CAD204520 and DMSO (time_50%-f/f0; $p < 0.05$). In accordance with this finding, the fluorescence computed at 3, 5, and 10 min from the peak time (f/f0_3 min, 5 min, and 10 min) or the area under the dose curve calculated within the same time frame (control versus CAD204520 Δmean = 0.4188; control versus thapsigargin Δmean = -2.658; CAD204520 versus thapsigargin Δmean = -3.077), was significantly higher only in the thapsigargin group ($p < 0.05$ and $p < 0.0001$, respectively), suggesting that CAD204520 did not delay the cytosolic Ca^{2+} reuptake.

As previously mentioned, in addition to the effects on Ca^{2+} dynamics, thapsigargin and thapsigargin analogs activate the ER-related stress pathway of the UPR (164). To compare

the effects of CAD204520 and thapsigargin on UPR activation we treated ALL/SIL, DND41, and RPMI-8402 at concentrations causing a similar ICN1 decrement (Figures 9C and S6A). Interestingly, only thapsigargin sustained the expression of validated UPR markers, such as P-eIF2α and the ER chaperone BiP (Grp78) (Figures 9C and S6A) or the proteolytic cleavage of ATF6 and its re-location in the nucleus (Figures 9D and S6B).

Sustained Ca^{2+} increase and UPR activation is associated with caspase-mediated apoptosis and cell death in several tissues (165), including cardiac cells (166). For example, Ca^{2+} release from the ER can induce delayed after-depolarizations leading to cardiac arrhythmias. Similarly, UPR activation has been found to play a role in arrhythmogenesis during human heart failure by affecting cardiac ion channel expression (167). Thus, we hypothesized, based on our Ca^{2+} dynamics studies, that cardiac cells may be more tolerant to CAD204520 compared with thapsigargin treatment. To validate this hypothesis, we tested CAD204520 and thapsigargin in HL-1 cardiac cells and demonstrated that HL-1 are less sensitive to SERCA inhibition compared with a *NOTCH1*-mutated cancer cell line, confirming that SERCA represents a strong dependency in T-ALL (Figures 9E and S6C). However, only cells treated with thapsigargin at IC50 concentrations displayed activation of the UPR pathway (Figure 9F), suggesting that CAD204520 further improves the therapeutic index of SERCA inhibitors because of its mild effect on Ca^{2+} dynamics and ER/UPR activation.

Modeling Preclinical Toxicity and Efficacy of CAD204520 in a T-ALL Leukemia Model

Because altered ER Ca^{2+} levels lead to heart failure (168), we measured the extent to which CAD204520 alters the function of heart cells. First, we isolated cardiomyocytes from Wistar rats and the cells were either untreated or incubated with CAD204520 or thapsigargin. The

average diastolic sarcomere length (expressed in μm) exhibited comparable values in all cell groups, independent of the treatment and the time of exposure to the inhibitors (Control, 1.74 ± 0.006; $CAD204520_{2h}$, 1.75 ± 0.008; $CAD204520_{4h}$, 1.74 ± 0.007; Control, 1.76 ± 0.004; $Thapsigargin_{200nM}$, 1.76 ± 0.005; $Thapsigargin_{500nM}$, 1.76 ± 0.009). Compared with control cells, cardiomyocytes incubated with 5 μM CAD204520 for 2 h ($CAD204520_{2h}$) showed a reduced contractile efficiency, as reflected by the decrease in the rate of shortening ($-dl/dt_{max}$; Figure 10A; -27%) and re-lengthening ($+dl/dt_{max}$; Figure 10B; -25%), coupled with a lower fraction of shortening (FS; (Figure 10C; -27%)). A further slight decline (approximately an additional 10% decrease) in cell mechanical performance was observed after 4 h exposure (data not shown). In accordance with cell contractile properties, $CAD204520_{2h}$ cardiomyocytes exhibited a modest (16%) decrease in the amplitude of the Ca^{2+} transient (Figure S7A) associated with a prolongation (+19%) of the time required for cytosolic Ca^{2+} removal (Figure S7B (Tau)). Choosing a thapsigargin dose for these comparative studies has been difficult due to the paucity of the in vivo studies reported in the literature. The dose selected for thapsigargin (200 nM) is in the mid-range of doses used by our group and others that assessed consequences of thapsigargin both *in vitro* and *in vivo* in different cancer models (75, 169, 170). Nevertheless, thapsigargin induced a greater negative effect in treated cardiomyocytes. In fact, the rate of contraction, relengthening and the fraction of shortening were reduced by 77%, 89%, and 66%, respectively, compared with the control group, suggesting that thapsigargin, at the tested concentrations, causes a marked impairment of cardiac cell mechanics (Figures 10A–10C). The thapsigargin-induced cell damage altered Ca^{2+} dynamics, as shown in the representative tracing reported in Figure S7C, hampering the measurement of Ca^{2+} transient parameters. Next, we evaluated the cytotoxic effect of CAD204520 on isolated cardiomyocytes by measuring the ability of the cells to produce ATP. Interestingly CAD204520 treatment only minimally affected the

cellular metabolic capacity (10%) compared with vehicle-treated cells, suggesting that CAD204520 does not induce marked effects on cardiomyocyte viability at the times and conditions tested (Figure S7D).

We then assessed the translational significance of our results. To explore the utility of the CAD204520 as an *in vivo* chemical probe, we performed a bioavailability and tissue distribution study (pharmacokinetic study) of CAD204520 in CD1 mice and found the compound to have a T½ of 11 h, and C_{max} of 1.1 ng/mL (2.5 μM) at T_{max} = 1 h. Next, we completed a tolerability study in male and female BALB/c mice after administration of 30 mg/kg of CAD204520 BID by oral gavage for 21 days. Importantly, no adverse clinical symptoms or cardiac toxicity events were seen in animals dosed with vehicle or 30 mg/kg of CAD204520 (Figure 10D). Mice treated with double that dose (60 mg/kg) had mild reduction of weight (Figure S7E), without incurring cardiac failure, consistent with our *ex vivo* results. Animals were sacrificed at day 21. No gross pathological abnormalities were detected on visceral organs, including the heart, lungs, liver, brain, or kidney in treated animals. With this dosing schedule, we determined a C_{max} within the range of CAD204520 for biological activities as established *in vitro* (1–10 μM) and, therefore, initiated treatment studies of CAD204520 in a preclinical model of T-ALL.

To assess the *in vivo* efficacy of CAD204520, we established T-ALL-derived xenografts from SKW-3/KE-37 human T-ALL cell lines and confirmed leukemia engraftment by the quantification of hCD45+cells in peripheral blood of transplanted mice (0.3% – 0.2% circulating hCD45+ cells 1 week before the start of treatment). Then, we treated our cohort at a dose of 45 mg/kg twice a day at 8 h intervals, for 4 days by oral gavage (Figure S7F). CAD204520 treatment resulted in a significant 56-fold reduction of the percentage of hCD45+ SKW-3/KE-37 cells in circulating leukemic cells of xenotransplanted mice

compared with the vehicle-administered control group (1.42% ± 2.6% versus 80.36% ± 4.5%; $p < 0.0001$) (Figures 10E and S7G) and, consistently, a reduction of leukemic infiltration in the spleen (Figures 10F and S7H). CAD204520-treated mice showed no decrease in body weight and no adverse effects on behavior. Importantly, no signs of acute cardiac toxicities (Figure 10G) or gastrointestinal metaplasia (Figure 10H) were documented. Furthermore, there were no changes in the complete blood counts between the control and treatment groups (Figure 10I).

Collectively these data demonstrate that CAD204520 reduces circulating leukemic cells without cardiac-related toxicity during short-term treatment in leukemia xenograft models, supporting further preclinical optimization in Notch1-dependent tumors.

Identification of glucocorticoids as potential rescue treatment in *NOTCH1*-mutated cell line carrying *ATP2A2* mutation

To anticipate the potential mechanism of resistance to SERCA inhibitors and identify synthetic lethality in the thapsigargin-resistant T-ALL cell line, we then performed a small molecule screening with nearly 2500 bioactive compounds from the European Chemical Biology Library provided by EU-OPENSCREEN. The library compounds were tested with 1 µM (data not shown) and 100 nM concentration. Thapsigargin, etoposide and DMSO were also tested as positive and negative control, respectively. Compound hits were flagged by their ability to preferentially inhibits ALL/SIL, ALL/SIL R or both. Surprisingly, we found a greater sensitivity of ALL/SIL R to several compounds that were not effective in the parental cell line (Figure 11A). Only 3 compounds, birinapant (IAP inhibitor) GSK461364 (PLK inhibitor) and zotarolimus (rapamycin analog that targets the FKBP12 binding protein upstream to mTOR) were active specifically in ALL/SIL compared to the resistant cell line

(Figure 11A). We then restricted the analysis to the top classes specifically active in the resistant cell line. Among these, small molecules targeting the steroid hormone receptors subfamily 3 were clearly represented by glucocorticoids (GC), including dexamethasone, clobetasol and fluticasone. While naïve cells were resistant to GC, ALL/SIL R cells showed an enhanced sensitivity at low nanomolar concentrations (Figure 11B).

ATP2A2 mutation induces upregulation of glucocorticoid receptor

To test whether the increased sensitivity to GCs resided in an upregulation of the specific nuclear receptor, we performed an immunoblotting in six different human T-ALL cell lines for glucocorticoid receptor (GR) and identified a significant increasing of the protein level in ALL/SIL R compared to the others (Figure 11C). In line with this finding, a RT-PCR confirmed an increased expression of both GR isoforms, α and β, in ALL/SILR compared to the parental cell line ALL/SIL (Figure 11 C). Surprisingly, a further validation showed that the same T-ALL cell lines were resistant to the treatment with dexamethasone, clobetasol and fluticasone while ALL/SIL R cells showed an enhanced sensitivity at low nanomolar concentrations (Figure 11D).

To tested whether the sensitivity to GCs was mediated by a soluble factor induced by SERCA mutation, we used ALL/SIL R conditioned medium for incubating different T-ALL cell lines and subsequently treated them with GCs: ALL/SIL R medium failed to restore corticosteroid sensitivity in the parental line and in other T-ALL cell lines (Figure 11E). On the other side, we showed that the sensitivity to GCs of the resistant cell line is related to the GR upregulation. In fact, the blockade of GR by RU486, a well-known GR antagonist, induced a reduction of GC activity in ALL/SIL R with a complete abolition of the effect of dexamethasone and a strong reduction of clobetasol (Figure 11F) and fluticasone

cytotoxicity (data not shown). These findings pointed out that *ATP2A2* mutation induces a metabolic adjustment with upregulation of GR and a subsequent higher sensitivity to glucocorticoids treatment.

SERCA inhibitors synergize with glucocorticoids with a better profile in *ATP2A2* mutated cells

Previous works showed an activity of GSI in reverting glucocorticoid-resistance, supporting combinatorial therapy against glucocorticoid-resistant T-ALL (171, 172). To test whether glucocorticoids can synergize with SERCA inhibitors regardless the presence of an *ATP2A2* mutation, overcoming in this way the resistance to SERCA inhibition, we treated sensitive and resistant cell lines with a combination of a SERCA inhibitor (thapsigargin or CAD204520) and a glucocorticoid (dexamethasone, clobetasol, fluticasone, prednisolone, methylprednisolone) for 72 h. To avoid the limitations and biases associated with any algorithm used to study drug-drug interactions, we used two approaches including the Loewe model and the Chou and Talalay index. The Loewe additivity is a commonly used dose-effect-based model to quantify a zero-interactive state for the combination of two drugs (151). The Chou-Talalay method for drug combination is based on the median-effect equation and provides a mechanism-independent method for quantitative determination, combination index (CI), of drug interactions (152). Consequently, the association of SERCA inhibitors plus GCs displayed a synergistic effect at low dose with a more pronounced activity in ALL/SIL R that harbors the *ATP2A2* mutation (Figure 11G), even with glucocorticoids that display an insufficient single compound activity, such as prednisolone and methylprednisolone (data not shown). These data highlight that the modulation of SERCA-Ca^{2+} activity and the impairment of Notch1 trafficking potentially revert GC resistance in *NOTCH1*-mutated T-ALL.

DISCUSSION

Although the prognosis of T-ALL has improved over the last two decades, the outcome of T-ALL patients with primary resistant or relapsed disease remains poor (173, 174). Therefore, current research goals are focused on the identification of targets to develop more effective and less-toxic anti-leukemic agents (100, 175-177).

Several studies strongly support the development of Notch inhibitors for targeted therapy in hematological malignancies and solid tumors where Notch signaling is deregulated (178). For example, pan Notch pathway antagonism with GSIs reduces leukemia growth in mutant cancer cell lines and in mouse models (91, 179). Thus, modulators of Notch would be expected to have clinical efficacy particularly in T-ALL where recurrent *NOTCH1* mutations are common and cancer dependency has been well established. However, prolonged suppression of the canonical Notch pathway in normal tissue may cause dose-limiting gastrointestinal toxicity (103) or increase the risk of skin cancers (180, 181), underscoring the need for new therapeutic modalities to preferentially suppress the oncogenic signal. In recent years, we have pursued this approach and demonstrated that selective inhibitors of SERCA, such as thapsigargin and CPA, uniquely among Notch inhibitors, preferentially affect mutated NOTCH1 proteins compared with the wild-type ones (75, 119).

Thapsigargin, a plant-derived sesquiterpene-γ-lactone, has been used extensively as a pharmacological tool to trigger Ca^{2+}-dependent and UPR pathways in several disease models (182). Because the increase of cytosolic Ca^{2+} and sustained UPR activation (ER stress) are important mediators of apoptosis, SERCA inhibitors have been considered for cancer therapies (183). However, large-scale isolation from *Thapsia* or scalable synthesis of thapsigargin is complex, requiring a 5- to 42-step process depending on the protocol used

(184-186). Similarly, the synthesis of thapsigargin-based derivatives presents significant challenges. In fact, thapsigargin itself possesses a polyoxygenated 5-7-5 tricyclic core linked to four diverse ester groups and eight stereogenic centers not suitable for structural modeling (184, 187). Structure-activity studies revealed that only few thapsigargin groups, for example, the ester bond at *O*(8), can be hydrolyzed to generate intermediate derivatives that can be used for conjugation with a peptide (188, 189) or with a cleavable ester linkage (119). In addition, modification of the thapsigargin ester acyl group, or of the lactone carbonyl, significantly reduces thapsigargin activity in cells or biochemical assays, preventing their broad applicability in cancer (190, 191).

A further limitation is that native thapsigargin is not tractable as a therapeutic agent due to expected Ca^{2+} shifts that can be prevented, for example, by creating inactive pro-drugs activated in a hysto-specific manner (116, 192). This is the mode of action of mipsagargin, a thapsigargin derivative currently undergoing clinical trials for solid tumors (183). Our group has developed JQ-FT, a folate-thapsigargin derivative that leverages the dependency of leukemia cells on folate metabolism to direct the inhibitor into T-ALL cells (119). Another strategy is to exploit analogs that possess an enhanced selectivity toward SERCA isoforms preferentially expressed in cancer cells (115, 193), while keeping the activity of SERCA2a, the major cardiac isoform, unaffected (194-196) (Figure 3).

An alternative is the development of small molecules that retain SERCA inhibitory capacities but have only transient effects on cytosolic Ca^{2+} shifts. This idea emerged from recent studies from the laboratory of Møller and colleagues that challenged the consensus idea that the elevation of cytosolic Ca^{2+} — rather than the depletion of ER Ca^{2+} — led to the cell death induced by thapsigargin and analogs (164, 197). Contrary to what is generally thought, the rapid rise of cytosolic Ca^{2+}, as observed with thapsigargin, and its role in the short-term

side effect on cardiac contractility, is not required for apoptosis after SERCA inhibition. It is rather the ER Ca^{2+} depletion and sustained UPR activation that contributes to cell death (164).

The effect of a given SERCA inhibitor on cytosolic and ER Ca^{2+} levels depends strongly on its molecular mechanism of interaction with the ATPase. For example, the thapsigargin derivative substituted with a 12-aminododecanoyl linker, Boc-8ADT, did not show measurable changes in Ca^{2+} levels even though it strongly inhibited SERCA ATPase activity (164) leading to apoptosis in LNCaP cells (198). This is probably due to the very slow binding kinetics of this compound leading to a slow net leakage of Ca^{2+} from the ER, which likely enables the maintenance of constant, stable cytosolic Ca^{2+} levels. Other possible causes for the lack of cytosolic Ca^{2+} peaks are a moderate decrease in SERCA's Ca^{2+} affinity or a residual Ca^{2+} transport activity in the presence of the compound. It is tempting to speculate that other SERCA inhibitors that have advanced to clinical testing might have a similar mode of action. Curcumin, a small molecule derived from the turmeric spice that stabilizes SERCA in the *E1* conformational state has been extensively tested in multiple cancer models and clinical trials (199) without causing major cardiac events. Cisplatin is a widely used platinum-containing compound that, among other effects, inhibits SERCA and Na^+/K^+-ATPase simultaneously (200). Given the large number or rotating bonds in CAD204520, slow binding kinetics to SERCA, as with Boc-8ADT, can also be anticipated. From our structural data, the interaction of CAD204520 with SERCA involves only two polar contacts, and one single hydrophobic contact within a distance of 3 Å. Overall, the interaction looks surprisingly ''loose'', perhaps indicating a concentration-dependent competition with Ca^{2+} binding and transport rather than an irreversible inhibition.

Our data also show that CAD204520 binds to SERCA differently from thapsigargin: it occupies a pocket between the transmembrane helices M1, M2, M3, and M4 of SERCA, whereas thapsigargin binds between M3, M5, and M7 (59). This observation agrees with our finding that thapsigargin, but not CPA, co-treatment enhances CAD204520's inhibitory effect, a feature that can be used for further medicinal chemistry optimization. In this regard, however, CAD204520 maintains the same thapsigargin ''property'' to preferentially alter mutated NOTCH1 trafficking. Remarkably, this ability has not yet been explored in two of the most recently synthesized putative SERCA inhibitors: the natural tricyclic clerodane diterpene casearin J (201) or ethyl 2-amino-6-(3,5-dimethoxyphenyl)-4-(2-ethoxy-2-oxoethyl)-4H-chromene-3-carboxylate (CXL017) (202), both active in T-ALL cell lines.

The next question is whether CAD204520 activity has limitations *in vivo* due to Ca^{2+} shifts. For example, mice exposed to a thapsigargin analog, L12-ADT, at 0.8 mg/kg, die within 8 h, putatively from cardiac toxicity (73). Cardiac SR Ca^{2+} ATPase (SERCA2a) plays a central role in myocardial contractility. SERCA2a actively transports Ca^{2+} into the SR and regulates cytosolic Ca^{2+} concentration, SR Ca^{2+} load, and thus the rate of contraction and relaxation of the heart (203). The amount of Ca^{2+} release from the SR, dictating the extent of cell shortening, is also a steep function of SR Ca^{2+} content (204). It follows that pharmacological inhibition of SERCA2a activity should reduce the amplitude of the transient calcium and the rate of SERCA-mediated Ca^{2+} removal, resulting in altered cardiomyocyte mechanics, as we observed in isolated unloaded ventricular myocytes exposed to CAD204520 or thapsigargin. However, the impairment of cellular contractile performance and Ca^{2+} dynamics was more pronounced after thapsigargin incubation compared with CAD204520 exposure (80%–90% reduction in functional performance versus 25%–30%, on average),

indicating that CAD204520 should have a better therapeutic window than thapsigargin *in vivo*.

An important question is whether and to what extent the depressed cardiomyocyte function secondary to pharmacological inhibition of SERCA2 activity would translate into decreased cardiac function *in vivo*. Based on previous experience from our group in a rat model of induced cardiomyopathy (205), a 20%–30% decline in cellular mechanics *ex vivo* results in a comparable moderate hemodynamic impairment in the intact animal. In fact, while CAD204520 exerts an anti-leukemia effect *in vivo* it does not induce heart failure in the two different mouse models (BALB/c CD1 and IL2-NSG) used for this study.

Although most *NOTCH1* mutations are found in exons 26 and 27 coding for the HD region, mutations in the PEST domain are present in 20%–30% of tumors resulting in an increased Notch activation due to the prolonged stabilization of ICN1 (91). Activating mutations clustered in the PEST sequence have been described in CLL and in MCL, and several efforts are ongoing to target NOTCH1 in these diseases (92, 118). Our study demonstrates that CAD204520 is active in cell lines carrying a PEST mutation (SKW-3/KE-37). This result supports testing SERCA inhibitors in disease models with this recurrent abnormality, such as CLL (206) and MCL (92). To this end, we extended testing CAD204520 in the REC-1 MCL cell line, one of the few representative models of *NOTCH1*-dependent MCL (92) carrying a H2428Pfs*7 PEST mutation. We showed that REC-1 is sensitive to CAD204520 inhibition compared with *NOTCH1* wild-type MCL lines. In REC-1, CAD204520 reduces Notch activation with a mechanism similar to the one observed in T-ALL. Because in MCL *NOTCH1* mutations are associated with significantly shorter survival rates (92, 207), the development of Notch-targeted therapy may represent an effective strategy to tackle this aggressive disease.

Finally, since SERCA inhibitors display a favorable therapeutic index by targeting mutated NOTCH1 proteins, the development of new SERCA inhibitors, such as CAD204520 is a reasonable strategy for *NOTCH1*-mutated malignancies. For this reason, to anticipate the potential mechanism of resistance to SERCA inhibitors can improve the deep characterization of this class of molecule and speed up the translation into a clinical setting. To this purpose, we performed a small molecule screening on two T-ALL cell lines, respectively sensitive and resistant to the effect of thapsigargin, and identified glucocorticoids among the top classes with high activity in the resistant cell line. The modulation of SERCA activity due to the hotspot mutation in the thapsigargin binding site induced an upregulation of glucocorticoid receptor with the subsequent reversal of steroid resistance. Furthermore, glucocorticoids showed a synergistic activity with SERCA inhibitors especially in the resistant cell line, paving the way to a better understanding of SERCA activity and modulation in *NOTCH1*-mutated cancer.

CONCLUSIONS

Modulation of intracellular Ca^{2+} homeostasis plays critical roles in key processes that regulate cellular survival, growth, differentiation, metabolism, and death in normal and cancer cells. Thus, it is not surprising that several anti-cancer agents suppress pro-survival and activate pro-apoptotic pathways through modulation of Ca^{2+} signaling-dependent mechanisms. This is, for example, the case for chemotherapeutics such as cytotoxic alkylating agents (208) or anti-metabolites that rely on a Ca^{2+} signaling component to induce cancer cell death (209). Similarly, natural compounds including alkaloids, flavonoids, diterpenoids, and polyphenolics have been extensively investigated for their ability to modulate intracellular Ca^{2+} concentration and participate in apoptotic signaling pathways. Among them SL, such as thapsigargin have been long regarded as target compounds for drug development. In fact, thapsigargin has a broad spectrum of growth suppressing activity in several tumor types including poorly dividing cells (210). However, we have demonstrated the SERCA inhibition may efficiently control the trafficking of NOTCH1 and that this blockade can be achieved without causing overt cardiac toxicities in preclinical leukemia models. Importantly the effects of SERCA suppression can be rescued by the overexpression of unprocessed NOTCH1 peptides such as ICN1 indicating that the anti-leukemia effect is on target for Notch inhibition rather than for more generic Ca^{2+} fluxes. An important standing question is why mutated *NOTCH1* appears more sensitive to SERCA suppression compared to wild type isoform or other proteins more broadly. One hypothesis to explain NOTCH1 and SERCA functional dependency is by mechanisms of co-regulation. It has been previously shown that presenilin (PSEN) and SERCA co-localize in the ER (211). Since PSEN1 is a key regulator of NOTCH1 maturation and preferentially binds FL-N1 polypeptides processed through the ER, it is possible that NOTCH1-PSEN1-SERCA are

part of a co-functional protein complex. Interestingly, in a recent paper, treatment of T-ALL cell lines with the selective PSEN1 inhibitor MRK-560 inhibited mutant NOTCH1 processing and led to cell cycle arrest. MRK-560 treatment decreases leukemia burden and increased overall survival with no associated gut toxicity in T-ALL patient-derived xenografts *in vivo* suggesting that, similar to SERCA inhibition, disruption of PSEN1 may preferentially affect mutated proteins. The second hypothesis is a Ca^{2+} mediated one. In fact, Malecki and colleagues previously demonstrated that clinically relevant activating *NOTCH1* HD mutations destabilize the NOTCH negative regulatory region and have deleterious effects on NOTCH1 folding and maturation. Because EGF and LNR repeats of NOTCH1 rely on Ca^{2+} for folding and activation, it may be possible that changes in ER Ca^{2+} may preferentially impair unstable NOTCH mutant proteins (212) compared to wild type providing a therapeutic window for SERCA inhibitors. Finally, a hypothesis not yet explored to explain FL-N1 accumulation at concentrations not sufficient to trigger the general mechanism of UPR is through a Ca^{2+} mediated transcriptional activation of inhibitors of furin-like proteases. This would explain for example why CAD204520 efficiently target cancers with isolated PEST deletions that would not be predicted to be unstable given a normal LNR and HD protein sequence.

In conclusion, this study presents CAD204520 as an orally bioavailable SERCA inhibitor with tolerable off-target toxicity in NOTCH1-dependent tumors. This work provides a foundation for further development of novel drugs targeting Notch-dependent cancers. It also provides a deeper understanding of how different SERCA modulators affect cardiac tissue physiology and how SERCA-Ca^{2+} modulation can pharmacologically modulate glucocorticoid resistance in T-ALL.

BIBLIOGRAPHY

1. Toyoshima C, Sasabe H, Stokes DL. Three-dimensional cryo-electron microscopy of the calcium ion pump in the sarcoplasmic reticulum membrane. Nature. 1993;362(6419):469.
2. Zhang P, Toyoshima C, Yonekura K, Green NM, Stokes DL. Structure of the calcium pump from sarcoplasmic reticulum at 8-Å resolution. Nature. 1998;392(6678):835.
3. Toyoshima C, Nakasako M, Nomura H, Ogawa H. Crystal structure of the calcium pump of sarcoplasmic reticulum at 2.6 Å resolution. Nature. 2000;405(6787):647.
4. Moncoq K, Trieber CA, Young HS. The molecular basis for cyclopiazonic acid inhibition of the sarcoplasmic reticulum calcium pump. Journal of Biological Chemistry. 2007;282(13):9748-57.
5. Toyoshima C, Nomura H. Structural changes in the calcium pump accompanying the dissociation of calcium. Nature. 2002;418(6898):605-11.
6. Laursen M, Bublitz M, Moncoq K, Olesen C, Møller JV, Young HS, et al. Cyclopiazonic acid is complexed to a divalent metal ion when bound to the sarcoplasmic reticulum Ca2+-ATPase. Journal of Biological Chemistry. 2009;284(20):13513-8.
7. Bublitz M, Musgaard M, Poulsen H, Thøgersen L, Olesen C, Schiøtt B, et al. Ion pathways in the sarcoplasmic reticulum Ca2+-ATPase. Journal of Biological Chemistry. 2013;288(15):10759-65.
8. Lipskaia L, Hulot J-S, Lompré A-M. Role of sarco/endoplasmic reticulum calcium content and calcium ATPase activity in the control of cell growth and proliferation. Pflügers Archiv-European Journal of Physiology. 2009;457(3):673-85.
9. Bobe R, Bredoux R, Corvazier E, Lacabaratz-Porret C, Martin V, Kovacs T, et al. How many Ca2+ ATPase isoforms are expressed in a cell type? A growing family of membrane proteins illustrated by studies in platelets. Platelets. 2005;16(3-4):133-50.
10. Papp B, Brouland JP, Arbabian A, Gelebart P, Kovacs T, Bobe R, et al. Endoplasmic reticulum calcium pumps and cancer cell differentiation. Biomolecules. 2012;2(1):165-86.
11. Vandecaetsbeek I, Vangheluwe P, Raeymaekers L, Wuytack F, Vanoevelen J. The Ca2+ pumps of the endoplasmic reticulum and Golgi apparatus. Cold Spring Harb Perspect Biol. 2011;3(5).
12. Wuytack F, Raeymaekers L, Missiaen L. Molecular physiology of the SERCA and SPCA pumps. Cell Calcium. 2002;32(5-6):279-305.

13. Baba-Aissa F, Raeymaekers L, Wuytack F, Dode L, Casteels R. Distribution and isoform diversity of the organellar Ca2+ pumps in the brain. Mol Chem Neuropathol. 1998;33(3):199-208.
14. Wootton LL, Michelangeli F. The effects of the phenylalanine 256 to valine mutation on the sensitivity of sarcoplasmic/endoplasmic reticulum Ca2+ ATPase (SERCA) Ca2+ pump isoforms 1, 2, and 3 to thapsigargin and other inhibitors. Journal of Biological Chemistry. 2006;281(11):6970-6.
15. Brini M, Calì T, Ottolini D, Carafoli E. Calcium pumps: why so many? Comprehensive Physiology. 2011;2(2):1045-60.
16. Primeau JO, Armanious GP, M'Lynn EF, Young HS. The sarcoendoplasmic reticulum calcium ATPase. Membrane Protein Complexes: Structure and Function: Springer; 2018. p. 229-58.
17. Albers R. Biochemical aspects of active transport. Annual review of biochemistry. 1967;36(1):727-56.
18. Møller JV, Olesen C, Winther A-ML, Nissen P. The sarcoplasmic Ca 2+-ATPase: design of a perfect chemi-osmotic pump. Quarterly reviews of biophysics. 2010;43(4):501-66.
19. Toyoshima C. Ion pumping by calcium ATPase of sarcoplasmic reticulum. Regulatory mechanisms of striated muscle contraction: Springer; 2007. p. 295-303.
20. Gorski PA, Ceholski DK, Young HS. Structure-function relationship of the SERCA pump and its regulation by phospholamban and sarcolipin. Membrane Dynamics and Calcium Signaling: Springer; 2017. p. 77-119.
21. Clausen JD, McIntosh DB, Vilsen B, Woolley DG, Andersen JP. Importance of Conserved N-domain Residues Thr441, Glu442, Lys515, Arg560, and Leu562 of Sarcoplasmic Reticulum Ca2+-ATPase for MgATP Binding and Subsequent Catalytic Steps PLASTICITY OF THE NUCLEOTIDE-BINDING SITE. Journal of Biological Chemistry. 2003;278(22):20245-58.
22. Ma H, Lewis D, Xu C, Inesi G, Toyoshima C. Functional and structural roles of critical amino acids within the "N","P", and "A" domains of the Ca2+ ATPase (SERCA) headpiece. Biochemistry. 2005;44(22):8090-100.
23. Olesen C, Picard M, Winther A-ML, Gyrup C, Morth JP, Oxvig C, et al. The structural basis of calcium transport by the calcium pump. Nature. 2007;450(7172):1036.

24. Clausen JD, Vilsen B, McIntosh DB, Einholm AP, Andersen JP. Glutamate-183 in the conserved TGES motif of domain A of sarcoplasmic reticulum Ca2+-ATPase assists in catalysis of E2/E2P partial reactions. Proceedings of the National Academy of Sciences. 2004;101(9):2776-81.
25. Xu C, Ma H, Inesi G, Al-Shawi MK, Toyoshima C. Specific structural requirements for the inhibitory effect of thapsigargin on the Ca2+ ATPase SERCA. Journal of Biological Chemistry. 2004;279(17):17973-9.
26. Yu M, Zhang L, Rishi AK, Khadeer M, Inesi G, Hussain A. Specific substitutions at amino acid 256 of the sarcoplasmic/endoplasmic reticulum Ca2+ transport ATPase mediate resistance to thapsigargin in thapsigargin-resistant hamster cells. Journal of Biological Chemistry. 1998;273(6):3542-6.
27. Laursen M, Bublitz M, Moncoq K, Olesen C, Moller JV, Young HS, et al. Cyclopiazonic acid is complexed to a divalent metal ion when bound to the sarcoplasmic reticulum Ca2+-ATPase. The Journal of biological chemistry. 2009;284(20):13513-8.
28. Obara K, Miyashita N, Xu C, Toyoshima I, Sugita Y, Inesi G, et al. Structural role of countertransport revealed in Ca(2+) pump crystal structure in the absence of Ca(2+). Proc Natl Acad Sci U S A. 2005;102(41):14489-96.
29. Winther A-ML, Bublitz M, Karlsen JL, Møller JV, Hansen JB, Nissen P, et al. The sarcolipin-bound calcium pump stabilizes calcium sites exposed to the cytoplasm. Nature. 2013;495(7440):265-9.
30. Jensen AML, Sørensen TLM, Olesen C, Møller JV, Nissen P. Modulatory and catalytic modes of ATP binding by the calcium pump. The EMBO journal. 2006;25(11):2305-14.
31. Sørensen TL-M, Møller JV, Nissen P. Phosphoryl transfer and calcium ion occlusion in the calcium pump. Science. 2004;304(5677):1672-5.
32. Toyoshima C. How Ca2+-ATPase pumps ions across the sarcoplasmic reticulum membrane. Biochimica et Biophysica Acta (BBA)-Molecular Cell Research. 2009;1793(6):941-6.
33. Sagara Y, Fernandez-Belda F, de Meis L, Inesi G. Characterization of the inhibition of intracellular Ca2+ transport ATPases by thapsigargin. J Biol Chem. 1992;267(18):12606-13.

34. Nørregaard A, Vilsen B, Andersen JP. Transmembrane segment M3 is essential to thapsigargin sensitivity of the sarcoplasmic reticulum Ca (2+)-ATPase. Journal of Biological Chemistry. 1994;269(43):26598-601.
35. Post R, Kume S, Tobin T, Orcutt B, Sen A. Flexibility of an active center in sodium-plus-potassium adenosine triphosphatase. The Journal of general physiology. 1969;54(1):306-26.
36. Toyoshima C, Norimatsu Y, Iwasawa S, Tsuda T, Ogawa H. How processing of aspartylphosphate is coupled to lumenal gating of the ion pathway in the calcium pump. Proceedings of the National Academy of Sciences. 2007;104(50):19831-6.
37. Musgaard M, Thøgersen L, Schiøtt B. Protonation states of important acidic residues in the central Ca2+ ion binding sites of the Ca2+-ATPase: a molecular modeling study. Biochemistry. 2011;50(51):11109-20.
38. Kósa M, Brinyiczki K, Van Damme P, Goemans N, Hancsák K, Mendler L, et al. The neonatal sarcoplasmic reticulum Ca 2+-ATPase gives a clue to development and pathology in human muscles. Journal of muscle research and cell motility. 2015;36(2):195-203.
39. Ji Y, Loukianov E, Loukianova T, Jones LR, Periasamy M. SERCA1a can functionally substitute for SERCA2a in the heart. American Journal of Physiology-Heart and Circulatory Physiology. 1999;276(1):H89-H97.
40. Jane Lalli M, Yong J, Prasad V, Hashimoto K, Plank D, Babu GJ, et al. Sarcoplasmic reticulum Ca2+ ATPase (SERCA) 1a structurally substitutes for SERCA2a in the cardiac sarcoplasmic reticulum and increases cardiac Ca2+ handling capacity. Circulation research. 2001;89(2):160-7.
41. Loukianov E, Ji Y, Grupp IL, Kirkpatrick DL, Baker DL, Loukianova T, et al. Enhanced myocardial contractility and increased Ca2+ transport function in transgenic hearts expressing the fast-twitch skeletal muscle sarcoplasmic reticulum Ca2+-ATPase. Circulation research. 1998;83(9):889-97.
42. He H, Giordano FJ, Hilal-Dandan R, Choi D-J, Rockman HA, McDonough PM, et al. Overexpression of the rat sarcoplasmic reticulum Ca2+ ATPase gene in the heart of transgenic mice accelerates calcium transients and cardiac relaxation. The Journal of clinical investigation. 1997;100(2):380-9.
43. Novelli A, Valente EM, Bernardini L, Ceccarini C, Sinibaldi L, Caputo V, et al. Autosomal dominant Brody disease cosegregates with a chromosomal (2;7)(p11.2;p12.1) translocation in an Italian family. Eur J Hum Genet. 2004;12(7):579-83.

44. Odermatt A, Taschner PE, Khanna VK, Busch HF, Karpati G, Jablecki CK, et al. Mutations in the gene-encoding SERCA1, the fast-twitch skeletal muscle sarcoplasmic reticulum Ca2+ ATPase, are associated with Brody disease. Nat Genet. 1996;14(2):191-4.
45. Vangheluwe P, Louch WE, Ver Heyen M, Sipido K, Raeymaekers L, Wuytack F. Ca2+ transport ATPase isoforms SERCA2a and SERCA2b are targeted to the same sites in the murine heart. Cell calcium. 2003;34(6):457-64.
46. Minamisawa S, Wang Y, Chen J, Ishikawa Y, Chien KR, Matsuoka R. Atrial chamber-specific expression of sarcolipin is regulated during development and hypertrophic remodeling. Journal of Biological Chemistry. 2003;278(11):9570-5.
47. Vangheluwe P, Schuermans M, Zádor E, Waelkens E, Raeymaekers L, Wuytack F. Sarcolipin and phospholamban mRNA and protein expression in cardiac and skeletal muscle of different species. Biochemical Journal. 2005;389(1):151-9.
48. Babu GJ, Bhupathy P, Carnes CA, Billman GE, Periasamy M. Differential expression of sarcolipin protein during muscle development and cardiac pathophysiology. Journal of molecular and cellular cardiology. 2007;43(2):215-22.
49. Stammers AN, Susser SE, Hamm NC, Hlynsky MW, Kimber DE, Kehler DS, et al. The regulation of sarco (endo) plasmic reticulum calcium-ATPases (SERCA). Canadian journal of physiology and pharmacology. 2015;93(10):843-54.
50. Anderson DM, Makarewich CA, Anderson KM, Shelton JM, Bezprozvannaya S, Bassel-Duby R, et al. Widespread control of calcium signaling by a family of SERCA-inhibiting micropeptides. Sci Signal. 2016;9(457):ra119-ra.
51. Anderson DM, Anderson KM, Chang C-L, Makarewich CA, Nelson BR, McAnally JR, et al. A micropeptide encoded by a putative long noncoding RNA regulates muscle performance. Cell. 2015;160(4):595-606.
52. Chandrasekera PC, Kargacin ME, Deans JP, Lytton J. Determination of apparent calcium affinity for endogenously expressed human sarco(endo)plasmic reticulum calcium-ATPase isoform SERCA3. Am J Physiol Cell Physiol. 2009;296(5):C1105-14.
53. Gunteski-Hamblin A-M, Greeb J, Shull G. A novel Ca2+ pump expressed in brain, kidney, and stomach is encoded by an alternative transcript of the slow-twitch muscle sarcoplasmic reticulum Ca-ATPase gene. Identification of cDNAs encoding Ca2+ and other cation-transporting ATPases using an oligonucleotide probe derived from the ATP-binding site. Journal of Biological Chemistry. 1988;263(29):15032-40.

54. Gelebart P, Martin V, Enouf J, Papp B. Identification of a new SERCA2 splice variant regulated during monocytic differentiation. Biochem Biophys Res Commun. 2003;303(2):676-84.
55. Dally S, Bredoux R, Corvazier E, Andersen JP, Clausen JD, Dode L, et al. Ca2+-ATPases in non-failing and failing heart: evidence for a novel cardiac sarco/endoplasmic reticulum Ca2+-ATPase 2 isoform (SERCA2c). The Biochemical journal. 2006;395(2):249-58.
56. Kimura T, Nakamori M, Lueck JD, Pouliquin P, Aoike F, Fujimura H, et al. Altered mRNA splicing of the skeletal muscle ryanodine receptor and sarcoplasmic/endoplasmic reticulum Ca2+-ATPase in myotonic dystrophy type 1. Hum Mol Genet. 2005;14(15):2189-200.
57. Foggia L, Hovnanian A. Calcium pump disorders of the skin. Am J Med Genet C Semin Med Genet. 2004;131c(1):20-31.
58. Dhitavat J, Fairclough RJ, Hovnanian A, Burge SM. Calcium pumps and keratinocytes: lessons from Darier's disease and Hailey-Hailey disease. Br J Dermatol. 2004;150(5):821-8.
59. Brini M, Carafoli E. Calcium pumps in health and disease. Physiological reviews. 2009;89(4):1341-78.
60. Burge SM, Wilkinson JD. Darier-White disease: a review of the clinical features in 163 patients. Journal of the American Academy of Dermatology. 1992;27(1):40-50.
61. Wuytack F, Dode L, Baba-Aissa F, Raeymaekers L. The SERCA3-type of organellar Ca 2+ pumps. Bioscience reports. 1995;15(5):299-306.
62. Dally S, Corvazier E, Bredoux R, Bobe R, Enouf J. Multiple and diverse coexpression, location, and regulation of additional SERCA2 and SERCA3 isoforms in nonfailing and failing human heart. Journal of molecular and cellular cardiology. 2010;48(4):633-44.
63. Dode L, Vilsen B, Van Baelen K, Wuytack F, Clausen JD, Andersen JP. Dissection of the functional differences between sarco(endo)plasmic reticulum Ca2+-ATPase (SERCA) 1 and 3 isoforms by steady-state and transient kinetic analyses. J Biol Chem. 2002;277(47):45579-91.
64. Arbabian A, Brouland JP, Gelebart P, Kovacs T, Bobe R, Enouf J, et al. Endoplasmic reticulum calcium pumps and cancer. BioFactors. 2011;37(3):139-49.
65. Mekahli D, Bultynck G, Parys JB, De Smedt H, Missiaen L. Endoplasmic-reticulum calcium depletion and disease. Cold Spring Harb Perspect Biol. 2011;3(6).

66. Periasamy M, Kalyanasundaram A. SERCA pump isoforms: their role in calcium transport and disease. Muscle & nerve. 2007;35(4):430-42.
67. Casemore D, Xing C. SERCA as a target for cancer therapies. Integr Cancer Sci Ther. 2015;2:100-3.
68. Chemaly ER, Troncone L, Lebeche D. SERCA control of cell death and survival. Cell Calcium. 2018;69:46-61.
69. Fan L, Li A, Li W, Cai P, Yang B, Zhang M, et al. Novel role of Sarco/endoplasmic reticulum calcium ATPase 2 in development of colorectal cancer and its regulation by F36, a curcumin analog. Biomed Pharmacother. 2014;68(8):1141-8.
70. Gelebart P, Kovacs T, Brouland JP, van Gorp R, Grossmann J, Rivard N, et al. Expression of endomembrane calcium pumps in colon and gastric cancer cells. Induction of SERCA3 expression during differentiation. J Biol Chem. 2002;277(29):26310-20.
71. Pacifico F, Ulianich L, De Micheli S, Treglia S, Leonardi A, Vito P, et al. The expression of the sarco/endoplasmic reticulum Ca2+-ATPases in thyroid and its down-regulation following neoplastic transformation. J Mol Endocrinol. 2003;30(3):399-409.
72. Furuya Y, Isaacs JT. Proliferation-dependent vs. independent programmed cell death of prostatic cancer cells involves distinct gene regulation. The Prostate. 1994;25(6):301-9.
73. Denmeade SR, Jakobsen CM, Janssen S, Khan SR, Garrett ES, Lilja H, et al. Prostate-specific antigen-activated thapsigargin prodrug as targeted therapy for prostate cancer. Journal of the National Cancer Institute. 2003;95(13):990-1000.
74. Liu LH, Boivin GP, Prasad V, Periasamy M, Shull GE. Squamous cell tumors in mice heterozygous for a null allele of Atp2a2, encoding the sarco (endo) plasmic reticulum Ca2+-ATPase isoform 2 Ca2+ pump. Journal of Biological Chemistry. 2001;276(29):26737-40.
75. Roti G, Carlton A, Ross KN, Markstein M, Pajcini K, Su AH, et al. Complementary genomic screens identify SERCA as a therapeutic target in NOTCH1 mutated cancer. Cancer cell. 2013;23(3):390-405.
76. Launay S, Gianni M, Kovacs T, Bredoux R, Bruel A, Gelebart P, et al. Lineage-specific modulation of calcium pump expression during myeloid differentiation. Blood. 1999;93(12):4395-405.
77. Akl H, Vervloessem T, Kiviluoto S, Bittremieux M, Parys JB, De Smedt H, et al. A dual role for the anti-apoptotic Bcl-2 protein in cancer: mitochondria versus endoplasmic reticulum. Biochimica et biophysica acta (BBA)-molecular cell research. 2014;1843(10):2240-52.

78. Pierro C, Cook SJ, Foets TC, Bootman MD, Roderick HL. Oncogenic K-Ras suppresses IP3-dependent Ca2+ release through remodelling of the isoform composition of IP3Rs and ER luminal Ca2+ levels in colorectal cancer cell lines. J Cell Sci. 2014;127(7):1607-19.
79. Giorgi C, Bonora M, Sorrentino G, Missiroli S, Poletti F, Suski JM, et al. p53 at the endoplasmic reticulum regulates apoptosis in a Ca2+-dependent manner. Proceedings of the National Academy of Sciences. 2015;112(6):1779-84.
80. Rodriguez-Mora O, LaHair MM, Howe CJ, McCubrey JA, Franklin RA. Calcium/calmodulin-dependent protein kinases as potential targets in cancer therapy. Expert opinion on therapeutic targets. 2005;9(4):791-808.
81. Park KC, Kim SW, Jeon JY, Jo AR, Choi HJ, Kim J, et al. Survival of Cancer Stem-Like Cells Under Metabolic Stress via CaMK2alpha-mediated Upregulation of Sarco/Endoplasmic Reticulum Calcium ATPase Expression. Clin Cancer Res. 2018;24(7):1677-90.
82. Michelangeli F, East JM. A diversity of SERCA Ca2+ pump inhibitors. Biochem Soc Trans. 2011;39(3):789-97.
83. Brouland J-P, Gélébart P, Kovacs T, Enouf J, Grossmann J, Papp B. The loss of sarco/endoplasmic reticulum calcium transport ATPase 3 expression is an early event during the multistep process of colon carcinogenesis. The American journal of pathology. 2005;167(1):233-42.
84. Lipskaia L, Keuylian Z, Blirando K, Mougenot N, Jacquet A, Rouxel C, et al. Expression of sarco (endo) plasmic reticulum calcium ATPase (SERCA) system in normal mouse cardiovascular tissues, heart failure and atherosclerosis. Biochimica et Biophysica Acta (BBA)-Molecular Cell Research. 2014;1843(11):2705-18.
85. Lacabaratz-Porret C, Launay S, Corvazier E, Bredoux R, Papp B, Enouf J. Biogenesis of endoplasmic reticulum proteins involved in Ca2+ signalling during megakaryocytic differentiation: an in vitro study. Biochem J. 2000;350 Pt 3:723-34.
86. Korošec B, Glavač D, Rott T, Ravnik-Glavač M. Alterations in the ATP2A2 gene in correlation with colon and lung cancer. Cancer genetics and cytogenetics. 2006;171(2):105-11.
87. Toki H, Minowa O, Inoue M, Motegi H, Karashima Y, Ikeda A, et al. Novel allelic mutations in murine Serca2 induce differential development of squamous cell tumors. Biochemical and biophysical research communications. 2016;476(4):175-82.

88. Prasad V, Boivin GP, Miller ML, Liu LH, Erwin CR, Warner BW, et al. Haploinsufficiency of Atp2a2, encoding the sarco (endo) plasmic reticulum Ca2+-ATPase isoform 2 Ca2+ pump, predisposes mice to squamous cell tumors via a novel mode of cancer susceptibility. Cancer research. 2005;65(19):8655-61.
89. Brou C, Logeat F, Gupta N, Bessia C, LeBail O, Doedens JR, et al. A novel proteolytic cleavage involved in Notch signaling: the role of the disintegrin-metalloprotease TACE. Molecular cell. 2000;5(2):207-16.
90. Ellisen LW, Bird J, West DC, Soreng AL, Reynolds TC, Smith SD, et al. TAN-1, the human homolog of the Drosophila notch gene, is broken by chromosomal translocations in T lymphoblastic neoplasms. Cell. 1991;66(4):649-61.
91. Weng AP, Ferrando AA, Lee W, Morris JP, Silverman LB, Sanchez-Irizarry C, et al. Activating mutations of NOTCH1 in human T cell acute lymphoblastic leukemia. Science. 2004;306(5694):269-71.
92. Kridel R, Meissner B, Rogic S, Boyle M, Telenius A, Woolcock B, et al. Whole transcriptome sequencing reveals recurrent NOTCH1 mutations in mantle cell lymphoma. Blood. 2012;119(9):1963-71.
93. Arruga F, Gizdic B, Serra S, Vaisitti T, Ciardullo C, Coscia M, et al. Functional impact of NOTCH1 mutations in chronic lymphocytic leukemia. Leukemia. 2014;28(5):1060.
94. Fabbri G, Holmes AB, Viganotti M, Scuoppo C, Belver L, Herranz D, et al. Common nonmutational NOTCH1 activation in chronic lymphocytic leukemia. Proceedings of the National Academy of Sciences. 2017;114(14):E2911-E9.
95. Lobry C, Oh P, Aifantis I. Oncogenic and tumor suppressor functions of Notch in cancer: it's NOTCH what you think. Journal of Experimental Medicine. 2011;208(10):1931-5.
96. Stransky N, Egloff AM, Tward AD, Kostic AD, Cibulskis K, Sivachenko A, et al. The mutational landscape of head and neck squamous cell carcinoma. Science. 2011;333(6046):1157-60.
97. Wang Z, Da Silva TG, Jin K, Han X, Ranganathan P, Zhu X, et al. Notch signaling drives stemness and tumorigenicity of esophageal adenocarcinoma. Cancer research. 2014;74(21):6364-74.
98. Roy M, Pear WS, Aster JC. The multifaceted role of Notch in cancer. Current opinion in genetics & development. 2007;17(1):52-9.

99. Klinakis A, Lobry C, Abdel-Wahab O, Oh P, Haeno H, Buonamici S, et al. A novel tumour-suppressor function for the Notch pathway in myeloid leukaemia. Nature. 2011;473(7346):230.
100. Roti G, Stegmaier K. New approaches to target T-ALL. Frontiers in oncology. 2014;4:170.
101. van Es JH, van Gijn ME, Riccio O, van den Born M, Vooijs M, Begthel H, et al. Notch/γ-secretase inhibition turns proliferative cells in intestinal crypts and adenomas into goblet cells. Nature. 2005;435(7044):959.
102. Golde TE, Koo EH, Felsenstein KM, Osborne BA, Miele L. γ-Secretase inhibitors and modulators. Biochimica et Biophysica Acta (BBA)-Biomembranes. 2013;1828(12):2898-907.
103. Deangelo D, Stone R, Silverman L, Stock W, Attar E, Fearen I, et al. A phase I clinical trial of the notch inhibitor MK-0752 in patients with T-cell acute lymphoblastic leukemia/lymphoma (T-ALL) and other leukemias. Journal of Clinical Oncology. 2006;24(18_suppl):6585-.
104. Riccio O, Van Gijn ME, Bezdek AC, Pellegrinet L, Van Es JH, Zimber-Strobl U, et al. Loss of intestinal crypt progenitor cells owing to inactivation of both Notch1 and Notch2 is accompanied by derepression of CDK inhibitors p27Kip1 and p57Kip2. EMBO reports. 2008;9(4):377-83.
105. Knoechel B, Bhatt A, Pan L, Pedamallu CS, Severson E, Gutierrez A, et al. Complete hematologic response of early T-cell progenitor acute lymphoblastic leukemia to the γ-secretase inhibitor BMS-906024: genetic and epigenetic findings in an outlier case. Molecular Case Studies. 2015;1(1):a000539.
106. Yuan X, Wu H, Xu H, Xiong H, Chu Q, Yu S, et al. Notch signaling: an emerging therapeutic target for cancer treatment. Cancer letters. 2015;369(1):20-7.
107. Schott AF, Landis MD, Dontu G, Griffith KA, Layman RM, Krop I, et al. Preclinical and clinical studies of gamma secretase inhibitors with docetaxel on human breast tumors. Clinical cancer research. 2013;19(6):1512-24.
108. Mukherjee N, Almeida A, Partyka KA, Lu Y, Schwan JV, Lambert K, et al. Combining a GSI and BCL-2 inhibitor to overcome melanoma's resistance to current treatments. Oncotarget. 2016;7(51):84594.

109. Groeneweg JW, DiGloria CM, Yuan J, Richardson WS, Growdon WB, Sathyanarayanan S, et al. Inhibition of notch signaling in combination with Paclitaxel reduces platinum-resistant ovarian tumor growth. Frontiers in oncology. 2014;4:171.
110. Ghantous A, Gali-Muhtasib H, Vuorela H, Saliba NA, Darwiche N. What made sesquiterpene lactones reach cancer clinical trials? Drug Discov Today. 2010;15(15-16):668-78.
111. Zhang Z, Yu S, Miao L, Huang X, Zhang X, Zhu Y, et al. Artesunate combined with vinorelbine plus cisplatin in treatment of advanced non-small cell lung cancer: a randomized controlled trial. Zhong xi yi jie he xue bao= Journal of Chinese integrative medicine. 2008;6(2):134-8.
112. Berger TG, Dieckmann D, Efferth T, Schultz ES, Funk J-O, Baur A, et al. Artesunate in the treatment of metastatic uveal melanoma-first experiences. Oncology reports. 2005;14(6):1599-603.
113. Singh N, Verma K. Case report of a laryngeal squamous cell carcinoma treated with artesunate. Archive of Oncology. 2002;10(4):279-80.
114. Singh NP, Panwar VK. Case report of a pituitary macroadenoma treated with artemether. Integrative cancer therapies. 2006;5(4):391-4.
115. Denmeade SR, Isaacs JT. The SERCA pump as a therapeutic target: making a “smart bomb” for prostate cancer. Cancer biology & therapy. 2005;4(1):21-9.
116. Christensen SB, Skytte DM, Denmeade SR, Dionne C, Moller JV, Nissen P, et al. A Trojan horse in drug development: targeting of thapsigargins towards prostate cancer cells. Anti-Cancer Agents in Medicinal Chemistry (Formerly Current Medicinal Chemistry-Anti-Cancer Agents). 2009;9(3):276-94.
117. Periz G, Fortini ME. Ca(2+)-ATPase function is required for intracellular trafficking of the Notch receptor in Drosophila. EMBO J. 1999;18(21):5983-93.
118. Baldoni S, Del Papa B, Dorillo E, Aureli P, De Falco F, Rompietti C, et al. Bepridil exhibits anti-leukemic activity associated with NOTCH1 pathway inhibition in chronic lymphocytic leukemia. International journal of cancer. 2018;143(4):958-70.
119. Roti G, Qi J, Kitara S, Sanchez-Martin M, Conway AS, Varca AC, et al. Leukemia-specific delivery of mutant NOTCH1 targeted therapy. Journal of Experimental Medicine. 2018;215(1):197-216.

120. La Starza R, Borga C, Barba G, Pierini V, Schwab C, Matteucci C, et al. Genetic profile of T-cell acute lymphoblastic leukemias with MYC translocations. Blood. 2014;124(24):3577-82.
121. La Starza R, Barba G, Demeyer S, Pierini V, Di Giacomo D, Gianfelici V, et al. Deletions of the long arm of chromosome 5 define subgroups of T-cell acute lymphoblastic leukemia. haematologica. 2016;101(8):951-8.
122. Andersen J, Lassen K, Møller J. Changes in Ca2+ affinity related to conformational transitions in the phosphorylated state of soluble monomeric Ca2+-ATPase from sarcoplasmic reticulum. Journal of Biological Chemistry. 1985;260(1):371-80.
123. Kabsch W. xds. Acta Crystallographica Section D: Biological Crystallography. 2010;66(2):125-32.
124. Evans PR, Murshudov GN. How good are my data and what is the resolution? Acta Crystallographica Section D: Biological Crystallography. 2013;69(7):1204-14.
125. McCoy AJ. Solving structures of protein complexes by molecular replacement with Phaser. Acta Crystallographica Section D: Biological Crystallography. 2007;63(1):32-41.
126. Drachmann ND, Olesen C, Møller JV, Guo Z, Nissen P, Bublitz M. Comparing crystal structures of Ca2+-ATP ase in the presence of different lipids. The FEBS journal. 2014;281(18):4249-62.
127. Adams PD, Afonine PV, Bunkóczi G, Chen VB, Davis IW, Echols N, et al. PHENIX: a comprehensive Python-based system for macromolecular structure solution. Acta Crystallographica Section D: Biological Crystallography. 2010;66(2):213-21.
128. Emsley P, Cowtan K. Coot: model-building tools for molecular graphics. Acta crystallographica section D: biological crystallography. 2004;60(12):2126-32.
129. Cid A, Perona R, Serrano R. Replacement of the promoter of the yeast plasma membrane ATPase gene by a galactose-dependent promoter and its physiological consequences. Current genetics. 1987;12(2):105-10.
130. Hill JE, Myers AM, Koerner T, Tzagoloff A. Yeast/E. coli shuttle vectors with multiple unique restriction sites. Yeast. 1986;2(3):163-7.
131. Klodos I, Esmann M, Post RL. Large-scale preparation of sodium-potassium ATPase from kidney outer medulla. Kidney international. 2002;62(6):2097-100.
132. Wang K, Li M, Hakonarson H. ANNOVAR: functional annotation of genetic variants from high-throughput sequencing data. Nucleic acids research. 2010;38(16):e164-e.

133. Meraviglia V, Bocchi L, Sacchetto R, Florio MC, Motta BM, Corti C, et al. HDAC inhibition improves the sarcoendoplasmic reticulum Ca2+-ATPase activity in cardiac myocytes. International journal of molecular sciences. 2018;19(2):419.
134. Bocchi L, Savi M, Naponelli V, Vilella R, Sgarbi G, Baracca A, et al. Long-term oral administration of theaphenon-e improves cardiomyocyte mechanics and calcium dynamics by affecting phospholamban phosphorylation and ATP production. Cellular Physiology and Biochemistry. 2018;47(3):1230-43.
135. Bublitz M, Morth JP, Nissen P. P-type ATPases at a glance. J Cell Sci. 2011;124(15):2515-9.
136. Hauptman PJ, Kelly RA. Digitalis. Circulation. 1999;99(9):1265-70.
137. Sachs G. Proton pump inhibitors and acid-related diseases. Pharmacotherapy: The Journal of Human Pharmacology and Drug Therapy. 1997;17(1):22-37.
138. Burghoorn HP, Soteropoulos P, Paderu P, Kashiwazaki R, Perlin DS. Molecular evaluation of the plasma membrane proton pump from Aspergillus fumigatus. Antimicrobial agents and chemotherapy. 2002;46(3):615-24.
139. Yatime L, Buch-Pedersen MJ, Musgaard M, Morth JP, Winther A-ML, Pedersen BP, et al. P-type ATPases as drug targets: tools for medicine and science. Biochimica et Biophysica Acta (BBA)-Bioenergetics. 2009;1787(4):207-20.
140. Li Z-h, Qiu M-z, Zeng Z-l, Luo H-y, Wu W-j, Wang F, et al. Copper-transporting P-type adenosine triphosphatase (ATP7A) is associated with platinum-resistance in non-small cell lung cancer (NSCLC). Journal of translational medicine. 2012;10(1):21.
141. Samimi G, Safaei R, Katano K, Holzer AK, Rochdi M, Tomioka M, et al. Increased expression of the copper efflux transporter ATP7A mediates resistance to cisplatin, carboplatin, and oxaliplatin in ovarian cancer cells. Clinical Cancer Research. 2004;10(14):4661-9.
142. Seto-Young D, Monk B, Mason AB, Perlin DS. Exploring an antifungal target in the plasma membrane H+-ATPase of fungi. Biochimica et Biophysica Acta (BBA)-Biomembranes. 1997;1326(2):249-56.
143. Kjellerup L, Gordon S, Cohrt KOH, Brown WD, Fuglsang AT, Winther A-ML. Identification of antifungal H+-ATPase inhibitors with effect on plasma membrane potential. Antimicrobial agents and chemotherapy. 2017;61(7):e00032-17.

144. Bublitz M, Kjellerup L, Cohrt KOH, Gordon S, Mortensen AL, Clausen JD, et al. Tetrahydrocarbazoles are a novel class of potent P-type ATPase inhibitors with antifungal activity. PloS one. 2018;13(1):e0188620.
145. Clausen JD, Kjellerup L, Cohrt KOH, Hansen JB, Dalby-Brown W, Winther A-ML. Elucidation of antimicrobial activity and mechanism of action by N-substituted carbazole derivatives. Bioorganic & medicinal chemistry letters. 2017;27(19):4564-70.
146. Christensen SB, Andersen A, Poulsen J-CJ, Treiman M. Derivatives of thapsigargin as probes of its binding site on endoplasmic reticulum Ca2+ ATPase: Stereoselectivity and important functional groups. FEBS letters. 1993;335(3):345-8.
147. Yu M, Lin J, Khadeer M, Yeh Y, Inesi G, Hussain A. Effects of various amino acid 256 mutations on sarcoplasmic/endoplasmic reticulum Ca2+ ATPase function and their role in the cellular adaptive response to thapsigargin. Archives of biochemistry and biophysics. 1999;362(2):225-32.
148. Zhong L, Inesi G, editors. Involvement of the S3 stalk segment in the sensitivity of serca ATPase to thapsigargin. BIOPHYSICAL JOURNAL; 1998: BIOPHYSICAL SOCIETY 9650 ROCKVILLE PIKE, BETHESDA, MD 20814-3998 USA.
149. Horn M, Kroef V, Allmeroth K, Schuller N, Miethe S, Peifer M, et al. Unbiased compound-protein interface mapping and prediction of chemoresistance loci through forward genetics in haploid stem cells. Oncotarget. 2018;9(11):9838.
150. Chidawanyika T, Sergison E, Cole M, Mark K, Supattapone S. SEC24A identified as an essential mediator of thapsigargin-induced cell death in a genome-wide CRISPR/Cas9 screen. Cell death discovery. 2018;4(1):1-13.
151. Loewe S. The problem of synergism and antagonism of combined drugs. Arzneimittelforschung. 1953;3:285-90.
152. Chou T-C. Drug combination studies and their synergy quantification using the Chou-Talalay method. Cancer research. 2010;70(2):440-6.
153. Twarog NR, Stewart E, Hammill CV, Shelat AA. BRAID: a unifying paradigm for the analysis of combined drug action. Scientific reports. 2016;6:25523.
154. Twarog NR, Stewart E, Hammill CV, Shelat AA. Erratum: BRAID: A Unifying Paradigm for the Analysis of Combined Drug Action. Scientific reports. 2018;8:46970.
155. Blaumueller CM, Qi H, Zagouras P, Artavanis-Tsakonas S. Intracellular cleavage of Notch leads to a heterodimeric receptor on the plasma membrane. Cell. 1997;90(2):281-91.

156. Logeat F, Bessia C, Brou C, LeBail O, Jarriault S, Seidah NG, et al. The Notch1 receptor is cleaved constitutively by a furin-like convertase. Proceedings of the National Academy of Sciences. 1998;95(14):8108-12.
157. Le Borgne R. Regulation of Notch signalling by endocytosis and endosomal sorting. Current opinion in cell biology. 2006;18(2):213-22.
158. Sharma A, Gadkari RA, Ramakanth SV, Padmanabhan K, Madhumathi DS, Devi L, et al. A novel monoclonal antibody against Notch1 targets leukemia-associated mutant Notch1 and depletes therapy resistant cancer stem cells in solid tumors. Scientific reports. 2015;5:11012.
159. Minowada J, Kohno K, Matsuo Y, Drexler H, Ohnuma T, Tax W, et al. Characteristics of 27 Human T-Cell Leukemia Cell Lines With/Without T-Cell Receptors of T3-Tiαβ or T3-Tiγδ Complex. Modern Trends in Human Leukemia VIII: Springer; 1989. p. 233-6.
160. Wang M, Kaufman RJ. The impact of the endoplasmic reticulum protein-folding environment on cancer development. Nature Reviews Cancer. 2014;14(9):581-97.
161. Parekh AB, Putney Jr JW. Store-operated calcium channels. Physiological reviews. 2005;85(2):757-810.
162. Orrenius S, Zhivotovsky B, Nicotera P. Regulation of cell death: the calcium–apoptosis link. Nature reviews Molecular cell biology. 2003;4(7):552-65.
163. Lu M, Lawrence DA, Marsters S, Acosta-Alvear D, Kimmig P, Mendez AS, et al. Opposing unfolded-protein-response signals converge on death receptor 5 to control apoptosis. Science. 2014;345(6192):98-101.
164. Sehgal P, Szalai P, Olesen C, Praetorius HA, Nissen P, Christensen SB, et al. Inhibition of the sarco/endoplasmic reticulum (ER) Ca2+-ATPase by thapsigargin analogs induces cell death via ER Ca2+ depletion and the unfolded protein response. Journal of Biological Chemistry. 2017;292(48):19656-73.
165. Sovolyova N, Healy S, Samali A, Logue SE. Stressed to death–mechanisms of ER stress-induced cell death. Biological chemistry. 2014;395(1):1-13.
166. Liu M, Dudley Jr SC. Role for the unfolded protein response in heart disease and cardiac arrhythmias. International journal of molecular sciences. 2015;17(1):52.
167. Dally S, Monceau V, Corvazier E, Bredoux R, Raies A, Bobe R, et al. Compartmentalized expression of three novel sarco/endoplasmic reticulum Ca2+ ATPase 3 isoforms including the switch to ER stress, SERCA3f, in non-failing and failing human heart. Cell calcium. 2009;45(2):144-54.

168. Yano M, Ikeda Y, Matsuzaki M. Altered intracellular Ca 2+ handling in heart failure. The Journal of clinical investigation. 2005;115(3):556-64.
169. Abdullahi A, Stanojcic M, Parousis A, Patsouris D, Jeschke MG. Modeling acute ER stress in vivo and in vitro. Shock (Augusta, Ga). 2017;47(4):506.
170. Ma Z, Fan C, Yang Y, Di S, Hu W, Li T, et al. Thapsigargin sensitizes human esophageal cancer to TRAIL-induced apoptosis via AMPK activation. Scientific reports. 2016;6:35196.
171. Real PJ, Ferrando AA. NOTCH inhibition and glucocorticoid therapy in T-cell acute lymphoblastic leukemia. Leukemia. 2009;23(8):1374-7.
172. Samon J, Castillo-Martin M, Jakubczak J, Randolph S, Cordon-Cardo C, Ferrando A. Reversal of glucocorticoid resistance by the g-secretase inhibitor PF-03084014 in T-cell acute lymphoblastic leukemia. Journal of Clinical Oncology. 2011;29(15_suppl):9553-.
173. Litzow MR, Ferrando AA. How I treat T-cell acute lymphoblastic leukemia in adults. Blood. 2015;126(7):833-41.
174. Marks DI, Rowntree C. Management of adults with T-cell lymphoblastic leukemia. Blood. 2017;129(9):1134-42.
175. Follini E, Marchesini M, Roti G. Strategies to overcome resistance mechanisms in T-cell acute lymphoblastic leukemia. International journal of molecular sciences. 2019;20(12):3021.
176. Roti G, Stegmaier K. Targeting NOTCH1 in hematopoietic malignancy. Critical Reviews™ in Oncogenesis. 2011;16(1-2).
177. La Starza R, Cambò B, Pierini A, Bornhauser B, Montanaro A, Bourquin J-P, et al. Venetoclax and bortezomib in relapsed/refractory early T-cell precursor acute lymphoblastic leukemia. JCO precision oncology. 2019;3.
178. Brzozowa-Zasada M, Piecuch A, Michalski M, Segiet O, Kurek J, Harabin-Słowińska M, et al. Notch and its oncogenic activity in human malignancies. European Surgery. 2017;49(5):199-209.
179. Palomero T, Lim WK, Odom DT, Sulis ML, Real PJ, Margolin A, et al. NOTCH1 directly regulates c-MYC and activates a feed-forward-loop transcriptional network promoting leukemic cell growth. Proceedings of the National Academy of Sciences. 2006;103(48):18261-6.

180. Doody RS, Raman R, Sperling RA, Seimers E, Sethuraman G, Mohs R, et al. Peripheral and central effects of γ-secretase inhibition by semagacestat in Alzheimer's disease. Alzheimer's research & therapy. 2015;7(1):36.
181. Extance A. Alzheimer's failure raises questions about disease-modifying strategies. Nature Publishing Group; 2010.
182. Lytton J, Westlin M, Hanley MR. Thapsigargin inhibits the sarcoplasmic or endoplasmic reticulum Ca-ATPase family of calcium pumps. Journal of Biological Chemistry. 1991;266(26):17067-71.
183. Mahalingam D, Cetnar J, Wilding G, Denmeade S, Sarantopoulos J, Kurman M, et al. Abstract B244: A first-in-human phase 1 clinical study of G-202, a thapsigargin-based Prostate-Specific Membrane Antigen (PSMA) activated prodrug, in patients with advanced solid tumors. AACR; 2013.
184. Ball M, Andrews SP, Wierschem F, Cleator E, Smith MD, Ley SV. Total synthesis of thapsigargin, a potent SERCA pump inhibitor. Organic letters. 2007;9(4):663-6.
185. Chen D, Evans PA. A concise, efficient and scalable total synthesis of thapsigargin and nortrilobolide from (R)-(−)-carvone. Journal of the American Chemical Society. 2017;139(17):6046-9.
186. Chu H, Smith JM, Felding J, Baran PS. Scalable synthesis of (−)-thapsigargin. ACS central science. 2016;3(1):47-51.
187. Ley SV, Antonello A, Balskus EP, Booth DT, Christensen SB, Cleator E, et al. Synthesis of the thapsigargins. Proceedings of the National Academy of Sciences of the United States of America. 2004;101(33):12073-8.
188. Andersen T, López C, Manczak T, Martinez K, Simonsen H. Thapsigargin—from Thapsia L. to mipsagargin. Molecules. 2015;20(4):6113-27.
189. Mahalingam D, Peguero J, Cen P, Allgood V, Shazer R, Campos L. Mipsagargin, a PSMA-directed prodrug, provides clinical benefit in patients with advanced sorafenib-refractory hepatocellular carcinoma. Journal of Hepatology. 2017;66(1):S207.
190. Thi Quynh Doan N, Brogger Christensen S. Thapsigargin, origin, chemistry, structure-activity relationships and prodrug development. Current pharmaceutical design. 2015;21(38):5501-17.
191. Treiman M, Caspersen C, Christensen SB. A tool coming of age: thapsigargin as an inhibitor of sarco-endoplasmic reticulum Ca2+-ATPases. Trends in pharmacological sciences. 1998;19(4):131-5.

192. Doan NTQ, Paulsen ES, Sehgal P, Møller JV, Nissen P, Denmeade SR, et al. Targeting thapsigargin towards tumors. Steroids. 2015;97:2-7.
193. Arbabian A, Brouland JP, Gélébart P, Kovàcs T, Bobe R, Enouf J, et al. Endoplasmic reticulum calcium pumps and cancer. Biofactors. 2011;37(3):139-49.
194. Clark JH, Kinnear NP, Kalujnaia S, Cramb G, Fleischer S, Jeyakumar LH, et al. Identification of functionally segregated sarcoplasmic reticulum calcium stores in pulmonary arterial smooth muscle. Journal of Biological Chemistry. 2010;285(18):13542-9.
195. Dally S, Corvazier E, Bredoux R, Bobe R, Enouf J. Multiple and diverse coexpression, location, and regulation of additional SERCA2 and SERCA3 isoforms in nonfailing and failing human heart. Journal of molecular and cellular cardiology. 2010;48(4):633-44.
196. Lipskaia L, Chemaly ER, Hadri L, Lompre A-M, Hajjar RJ. Sarcoplasmic reticulum Ca2+ ATPase as a therapeutic target for heart failure. Expert opinion on biological therapy. 2010;10(1):29-41.
197. Szalai P, Parys JB, Bultynck G, Christensen SB, Nissen P, Møller JV, et al. Nonlinear relationship between ER Ca2+ depletion versus induction of the unfolded protein response, autophagy inhibition, and cell death. Cell calcium. 2018;76:48-61.
198. Dubois C, Vanden Abeele F, Sehgal P, Olesen C, Junker S, Christensen SB, et al. Differential effects of thapsigargin analogues on apoptosis of prostate cancer cells: complex regulation by intracellular calcium. The FEBS journal. 2013;280(21):5430-40.
199. Wilken R, Veena MS, Wang MB, Srivatsan ES. Curcumin: A review of anti-cancer properties and therapeutic activity in head and neck squamous cell carcinoma. Molecular cancer. 2011;10(1):12.
200. Tadini-Buoninsegni F, Sordi G, Smeazzetto S, Natile G, Arnesano F. Effect of cisplatin on the transport activity of P II-type ATPases. Metallomics. 2017;9(7):960-8.
201. De Ford C, Heidersdorf B, Haun F, Murillo R, Friedrich T, Borner C, et al. The clerodane diterpene casearin J induces apoptosis of T-ALL cells through SERCA inhibition, oxidative stress, and interference with Notch1 signaling. Cell death & disease. 2016;7(1):e2070.
202. Bleeker NP, Cornea RL, Thomas DD, Xing C. A novel SERCA inhibitor demonstrates synergy with classic SERCA inhibitors and targets multidrug-resistant AML. Molecular pharmaceutics. 2013;10(11):4358-66.

203. Periasamy M, Bhupathy P, Babu GJ. Regulation of sarcoplasmic reticulum Ca2+ ATPase pump expression and its relevance to cardiac muscle physiology and pathology. Cardiovascular research. 2007;77(2):265-73.
204. Bassani J, Yuan W, Bers DM. Fractional SR Ca release is regulated by trigger Ca and SR Ca content in cardiac myocytes. American Journal of Physiology-Cell Physiology. 1995;268(5):C1313-C9.
205. Savi M, Bocchi L, Mena P, Dall'Asta M, Crozier A, Brighenti F, et al. In vivo administration of urolithin A and B prevents the occurrence of cardiac dysfunction in streptozotocin-induced diabetic rats. Cardiovascular diabetology. 2017;16(1):80.
206. Di Ianni M, Baldoni S, Rosati E, Ciurnelli R, Cavalli L, Martelli MF, et al. A new genetic lesion in B-CLL: a NOTCH1 PEST domain mutation. British journal of haematology. 2009;146(6):689-91.
207. Beà S, Valdés-Mas R, Navarro A, Salaverria I, Martín-Garcia D, Jares P, et al. Landscape of somatic mutations and clonal evolution in mantle cell lymphoma. Proceedings of the National Academy of Sciences. 2013;110(45):18250-5.
208. Tadini-Buoninsegni F, Sordi G, Smeazzetto S, Natile G, Arnesano F. Effect of cisplatin on the transport activity of PII-type ATPases. Metallomics. 2017;9(7):960-8.
209. Can G, Akpinar B, Baran Y, Zhivotovsky B, Olsson M. 5-Fluorouracil signaling through a calcium-calmodulin-dependent pathway is required for p53 activation and apoptosis in colon carcinoma cells. Oncogene. 2013;32(38):4529-38.
210. Baliakas P, Hadzidimitriou A, Sutton LA, Rossi D, Minga E, Villamor N, et al. Recurrent mutations refine prognosis in chronic lymphocytic leukemia. Leukemia. 2015;29(2):329-36.
211. Green KN, Demuro A, Akbari Y, Hitt BD, Smith IF, Parker I, et al. SERCA pump activity is physiologically regulated by presenilin and regulates amyloid beta production. J Cell Biol. 2008;181(7):1107-16.
212. Malecki MJ, Sanchez-Irizarry C, Mitchell JL, Histen G, Xu ML, Aster JC, et al. Leukemia-associated mutations within the NOTCH1 heterodimerization domain fall into at least two distinct mechanistic classes. Mol Cell Biol. 2006;26(12):4642-51.

FIGURE LEGENDS

Figure 1. SERCA catalytic cycle

A) SERCA pumps Ca^{2+} from the cytoplasm to the endoplasmic reticulum (ER) to create an ion gradient of ~ 10,000-fold across the cell membranes. During the catalytic cycle the Ca^{2+}-ATPase switches between diverse oriented structures (*E1* and *E2*) characterized by a different affinity for Ca^{2+} ions. The enzymatic transition between conformations catalyzes ATP in a stoichiometric ratio with Ca^{2+} of 1:2. *E1* binds two molecules of cytoplasmic Ca^{2+} ($2Ca^{2+}$-*E1*, top right) and hydrolyzes one molecule of ATP to induce the high energy state of SERCA (*E1* ~ P). Following the decay in ADP, *E2* ~ P releases Ca^{2+} in the ER lumen. The cycle is closed and reopened along with the dephosphorylation of SERCA.

B) Thapsigargin (or other SERCA inhibitors) locks SERCA in the ground *E2* state ("dead-end") preventing Ca^{2+} binding and ATP hydrolysis. Thapsigargin blockade causes a continuum leakage of Ca^{2+} from the ER to the cytosol reverting the physiological polarization of Ca^{2+} across these two components.

Figure 2. SERCA and Notch trafficking

A) Schematic representation of the effects of SERCA inhibition on the maturation and trafficking of NOTCH1. In physiologic conditions, SERCA pumps Ca^{2+} into the ER required for the proper folding of NOTCH1 proteins. A furin-like protease (S1) releases from the ER/Golgi the non-covalent heterodimer NOTCH1-FL1 that migrates through the cytosol toward the cell membrane. Following the interaction of the extracellular NOTCH1-extracellular domain (ECD-N1) with the NOTCH ligands, NOTCH1 is cleaved sequentially

by metalloproteases (S2) and γ-secretase [GS (S3)]. The final cleaved protein ICN1 migrates to the nucleus to complex with co-activators and activates transcription.

B) SERCA blockade by SERCA inhibitors (e.g., thapsigargin) induces a leak of ER Ca^{2+} and accumulation of the full-length isoform of NOTCH1 at the ER/Golgi level. Consequently, no substrate for metalloprotease or GS is available with the result of a reduced level of nuclear ICN1 protein.

Figure 3. Strategy to overcome thapsigargin toxicity

A) Mipsagargin is a thapsigargin derivative coupled with a masking peptide that is a substrate for the carboxypeptidase prostate-specific membrane antigen (PSMA). This peptide reduces the affinity of these molecules toward SERCA in non-neoplastic cells. However, if mipsagargin intercepts PSMA on tumor cells or neoplastic neoangiogenic vessels, it is cleaved into a cytotoxic analog of thapsigargin (12-ADT-Asp) and diffuses into the cancer cells.

B) JQ-FT is a derivative of thapsigargin, 8-*O*-debutanoyl-thapsigargin, linked with folic acid (FA). In tumor cells expressing folate receptor (FR), JQ-FT enters through endocytosis and proteases release the 8-*O*-debutanoyl-thapsigargin from FA directly into the cytosol of target cells.

C) Identification of SERCA inhibitors by high-throughput screening. ATPase activity assays (Ca^{2+}-ATPase vs Na^{+}/K^{+}-ATPase vs H^{+}/K^{+}-ATPase) or *in silico* prediction.

Figure 4. Identification, Structure-Activity Relationship and Co-crystal Structure of CAD204520

A) Identification of CAD204520. A total of 191,000 small molecules were screened for inhibition of the fungal H^+-ATPase Pma1. Molecules with an enzymatic inhibition of the H^+-ATPase that exceed 50% were retained for subsequent hit validation. The 407 molecules were counter screened for (Pma1 over SERCA or Na^+/K^+) ATPase selectivity and minimum growth inhibitory capacity (MIC) <150 μM. Hits were then characterized as described in (143). From a subsequent hit optimization program (see B), CAD204520 was identified as the most promising candidate against mammalian Ca^{2+}-ATPase (SERCA).

B) Structure-activity relationship (SAR) of CAD204520.

C) Crystal structure of the SERCA-CAD204520 complex. Right panel: cartoon and surface representation of SERCA (light blue) with CAD204520 bound at the membrane interface (orange surface representation). Left panels: close-up of the CAD204520 binding sites, as seen parallel to the membrane (upper panel) or along the membrane normal (lower panel). Dashed lines indicate polar interactions with Asp^{59} (2.9 Å) and Asn^{101} (2.7 Å). Nitrogen is shown in blue, oxygen in red, and fluorine in cyan. Carbon is light blue for SERCA and orange for CAD204520.

D) Simulated annealing omit map (green mesh) of CAD204520 (orange), contoured at 3.0 sigma. Top panel, viewed roughly along the membrane plane; bottom panel, viewed roughly perpendicular to the membrane.

Figure 5. CAD204520 Overcomes Thapsigargin Resistance in T-ALL

A) Lollipop graphs showing sequenced mutations in the exonic region of *ATP2A1*, *ATP2A2*, and *ATP2A3* genes. Allelic variants are depicted with a circle (black, synonymous; red, missense) relative to their amino acid position (gray bottom bar, aa) and to their protein domains (color coded). The length of the lollipop (number of mutations) bar indicates: if 0, no mutations occur; if 1, mutations occur in one sample; if 2, mutations occur in both samples.

B) Effect of CAD204520 and thapsigargin and CAD204520 treatment in naive and resistant ALL/SIL cells lines. Histograms show percentage of cells alive after 72 h of treatment at the indicated concentrations (~IC50). Error bar denotes the mean ± SD of a minimum of three replicates. Statistical significance among groups (****$p \leq 0.0001$) was determined by one-way ANOVA.

C) Surface plots analysis of ALL/SIL, DND41, and RPMI-8402 T-ALL cell lines and a primary *NOTCH1*-mutated T-ALL sample treated with vehicle, CAD204520, thapsigargin, or CAD204520 plus thapsigargin. Each point represents an independent measurement representative of three biological replicates. Plots were generated using the Combenefit script by MATLAB R201, which represents the Loewe (dose-effect-based approach) analysis. A color scale bar represents the level of drug antagonism or synergism.

D) Combination index analysis for the combinations of CAD204520 with thapsigargin in ALL/SIL, DND41 and RPMI-8402 T-ALL cell lines and a primary *NOTCH1*-mutated T-ALL treated for 3 days. On the y axis is represented the combination index, on the x axis the fraction of cells inhibited.

E) BRAID index analysis for the combinations of CAD204520 with thapsigargin in ALL/SIL, DND41, and RPMI-8402 T-ALL cell lines and a primary *NOTCH1*-mutated T-ALL treated for

3 days. A color scale bar represents the level of drug antagonism or synergism. K index is indicated.

Figure 6. CAD204520 Impairs T-ALL Proliferation

A) Effect of CAD204520 on cell viability after 72 h of treatments in the indicated T-ALL cell lines. Error bars denote ± SD of two replicates.

B) Effect of CAD204520 on cell viability after 72 h of treatments in the indicated MCL cell lines. Error bars denote ± SD of two replicates.

C) Effect of CAD204520 treatment on induction of apoptosis. Annexin V/propidium iodide staining of T-ALL cells after 72 h of treatment with the indicated concentrations of CAD204520. A minimum of 20,000 events was collected for each condition.

D) Western immunoblot showing expression of cleaved PARP in *NOTCH1*-mutated cell lines (ALL/SIL, DND41, RPMI-8402, and REC-1) cells treated at the indicated concentrations of CAD204520 for 24 h. β-Actin was used as a loading control.

E) Effect of CAD204520 treatments on cycling ALL/SIL, DND41, RPMI-8402, and REC-1 cells. Percentage of DNA content after 4 days of treatment with the indicated concentrations of CAD204520 on each cell-cycle phase is indicated. A minimum of 20,000 events was collected for each condition.

Figure 7. CAD204520 Modulates Notch1 Signaling

A) Effect of CAD204520 treatment for 24 h on NOTCH1 (N1) processing and activation in T-ALL cell lines all with heterodimerization mutations (ALL/SIL [L1575PΔPEST], DND41

[L1594PΔPEST] and RPMI-8402 [ins1584PVELMPPE]). The blot was incubated with an antibody against the C terminus of NOTCH1 that recognizes both the furin-processed NOTCH1 transmembrane subunit (TM) and the unprocessed NOTCH1 precursor (FL).

B) Effect of 24 h of CAD204520 and GSI (N-[N-(3,5-difluorophenacetyl)-1-alanyl]-(S)-phenylglycine [DAPT]) treatments on NOTCH1 cell surface staining as assessed by flow cytometry.

C) Effect of CAD204520 and GSI (DAPT) treatment (24 h) on the subcellular localization of NOTCH1. Immunofluorescence images of permeabilized ALL/SIL incubated with anti-Notch1 (C20-red) and anti-Golgin (green) are shown. Co-localization is indicated by yellow signal. Scale bar, 100 μm magnification.

D) Western immunoblot showing the expression of cleaved NOTCH1 (ICN1) in ALL/SIL, DND41, and RPMI-8402 cells treated at the indicated concentrations of CAD204520 for 24 h. HSP90 was used as a loading control.

E) CAD204520 treatment for 24 h downregulates expression of NOTCH1 target genes in ALL/SIL, DND41, and RPMI-8402 T-ALL cells as assessed by qRT-PCR. Error bars indicate the mean ± SD of four replicates. Data were analyzed using the ΔΔCT method and plotted as a percentage relative to the control gene *RPL13A*. Statistical significance (***$p \leq 0.001$, ****$p \leq 0.0001$) was determined by one-way ANOVA using Bonferroni's correction for multiple comparison testing. GSI (DAPT) was used as a positive control.

Figure 8. *NOTCH1* Mutation Sensitizes T-ALL Cells to CAD204520 Inhibition

A) Interphase and metaphase FISH, with the LSI MYC probe, show split signals between der(8) (red signal) and der(14) (green signal), in the MOLT-16 (left) and SKW-3/KE-37 (right) cell lines. (b) SKW-3/KE-37 has two der(8).

B) Left: cell-based competition assay. SKW-3/KE-37 and MOLT16 were transduced with a GFP-containing vector or an empty control vector, respectively, and co-cultured at a 1:1 ratio. Right: normalized effect of CAD204520 on cellular viability in co-cultured SKW-3/KE-37-GFP and MOLT16 cells treated for 72 h. Error bars denote the mean ± SD of two replicates for vehicle-treated (DMSO) cells and for CAD204520-treated cells. Statistical significance (*$p \leq 0.05$) was determined by one-way ANOVA using Bonferroni's correction for multiple comparison testing.

C) Caspase-3/-7 luminescence fold induction in SKW-3/KE-37 and MOLT16 cells. Error bars denote the mean ± SD of six replicates for vehicle-treated (DMSO) cells and for CAD204520-treated cells. Statistical significance (***$p \leq 0.001$) was determined by one-way ANOVA using Bonferroni's correction for multiple comparison testing.

D) Effect of CAD204520 treatment for 24 h on NOTCH1 (N1) processing and activation in SKW-3/KE-37 and MOLT16 cell lines. The immunoblot was stained with an antibody against the C terminus of NOTCH1 that recognizes the furin-processed NOTCH1 TM and the unprocessed NOTCH1 precursor (FL). HSP90 was used as a loading control.

E) Effect of the CAD204520 in primary T-ALL cells (n = 9) or isolated lymphocytes (n = 6). The whisker plot represents the effect of small molecules on cellular viability calculated using the area under the curve (AUC) model of log-transformed dose-responses data using GraphPad v.7. The line in the whisker diagram represents the AUC median. The upper edge (hinge) indicates the 75th percentile of the dataset, and the lower hinge the 25th percentile.

The ends of the vertical line show the minimum and the maximum data values. Statistical significance (***p ≤ 0.001) was determined by a non-parametric t test (Mann-Whitney).

F) Normalized effect of the CAD204520 in primary *NOTCH1*-mutated T-ALL cells (n = 2) or primary B-ALL cells (n = 2) on cellular viability. Error bars denote the mean ± SD of four replicates. Statistical significance comparing each T-ALL versus B-ALL case to each dose (***p ≤ 0.001, ****p ≤ 0.0001) was determined by a non-parametric t test (Mann-Whitney).

Figure 9. Effects of CAD204520 on Ca^{2+} and UPR Activation

A) Indo-1 AM fluorescence traces of T-ALL cells loaded with 5 μM of Indo-1 AM and treated with DMSO, CAD204520 1 μM, or thapsigargin 1 μM. Baseline and post-treatment fluorescence is indicated by a black arrow. Cells were acquired for a minimum of 10 min on an LSR Fortessa X20 flow cytometer.

B) Time course of ER calcium release and reuptake traces recorded in DMSO, CAD204520, and thapsigargin T-ALL-treated cells. Each trace is representative of five (DMSO) or four (CAD204520 and thapsigargin) independent experiments. In green the area under the curve (AUC). Values are reported as mean ± SEM; f/f0_peak, peak fluorescence normalized to baseline fluorescence; time_50%-f/f0, time at 50% of fluorescence signal decay measured from the peak time; f/f0_3min, 5min, and 10 min, fluorescence computed at 3, 5, and 10 min from the peak time. *p < 0.05 versus DMSO; #p < 0.05 versus 1 μM CAD204520. Statistical significance was determined by a Kruskal-Wallis test and differences among groups were determined by a Mann-Whitney non-parametric t test.

C) Effect of CAD204520 and thapsigargin treatment for 24 h in ALL/SIL and DND41 cell lines. The blot was stained with an antibody against the C terminus of NOTCH1 that

recognizes the furin-processed NOTCH1 TM and the unprocessed NOTCH1 precursor (FL), an antibody that recognizes the cleaved NOTCH1 (ICN1), P-eIF2α, total eIF2α, BiP, and HSP90 used as a loading control.

D) Effect of CAD204520 and thapsigargin treatment for 24 h on ATF6 in ALL/SIL cell line. Immunofluorescence of permeabilized ALL/SIL cells stained with ATF6 (green) is shown. Cell nuclei were stained with DAPI (blue). Scale bar, 100 mm.

E) Effects of CAD204520 (left) and thapsigargin (right) on cell viability after 72 h of treatments in HL-1 and ALL/SIL cell lines. Error bars denote ± SD of a minimum of two replicates.

(F) Effect of CAD204520 and thapsigargin treatment for 24 h in HL-1 cell lines. The blot was stained with BiP. β-Actin was used as a loading control.

Figure 10. Effects of CAD204520 on Preclinical Model of T-ALL

A–C) Left panels: effect of CAD204520 treatment on rat cardiomyocyte mechanics. Single experiments are represented by two dots interconnected by a solid line. Specifically, the line between the dots connects the quantification of maximal rate of shortening (A) ($-dl/dt_{max}$), maximal rate of re-lengthening (B) ($+dl/dt_{max}$), and fraction of shortening (C) (FS%), before and after the CAD204520 (5 μM) or thapsigargin (200 nM) treatment compared with control (Control). (A–C) Right panels: mean percentage effect of CAD204520 ($CAD204520_{2h}$) and thapsigargin ($Thapsigargin_{200nM}$) on the same cardiac functions. Graph bars: mean ± SD of the six CAD204520-treated cardiomyocyte groups and mean ± SD of the two thapsigargin-treated cardiomyocyte groups. Statistical significance comparing CAD204520-treated cells

versus thapsigargin-treated cells (**p ≤ 0.001, *p ≤ 0.05) was determined by a non-parametric t test (Mann-Whitney).

D) Effect of daily 30 mg/kg administration of CAD204520 on body weight. Error bars denote the mean ± SD of six replicates (three male and three female mice). Statistical significance (n.s.) was determined by a two-way ANOVA analysis.

E) Effect of CAD204520 on T-ALL leukemia burden in an SKW-3/KE-37-xenografted murine model. Anti-leukemic activity of CAD204520 assessed by measuring hCD45+ cells after 4 days of CAD204520 treatment (45 mg/kg/OS BID) or vehicle (Tween 80 0.5%, w/v, and hydroxypropyl-methylcellulose [HPMC] 1.0%, w/v). Representative dot plot showing the effect of CAD204520 on T-ALL growth in an SKW-3/KE-37 murine model. A minimum of 20,000 events was collected for each condition.

F) Immunohistochemical analysis of the spleen in an SKW-3/KE-37-xenografted murine model treated with CAD204520 45 mg/kg or vehicle for 4 days. The spleens of all mice were examined; representative results for one control animal and one CAD204520-treated animal are shown. Formalin-fixed, paraffin-embedded tissue sections were stained with hCD45. Scale bars, 20 μm.

G) Representative images of hematoxylin/eosin-stained sections of the left ventricle from SKW-3/KE-37 xenograft treated with CAD204520 45 mg/kg or vehicle. CAD204520 treatment did not affect the gross structural components of the myocardium or induce focal areas of damage. Well-aligned myofibers in the absence of myocytolytic necrosis or interstitial inflammatory infiltrates are shown at higher magnification (inset). Scale bars, 0.2 mm (low magnification) and 0.05 mm (high magnification; insets).

H) Representative images of hematoxylin/eosin-stained histological sections of the small intestines from SKW-3/KE-37 xenograft treated with CAD204520 45 mg/kg or vehicle. Compared with controls, intestinal villi and crypts appear to be well preserved in CAD204520-treated animals. At higher magnification (inset), no morphological changes in goblet cells and enterocytes were observed in CAD204520-treated mice. Scale bars, 0.2 mm (low magnification) and 0.05 mm (high magnification; insets).

I) Effect of CAD204520 on cell blood count WBC, hemoglobin, and platelets in an SKW-3/KE-37 murine model after 4 days of CAD204520 treatment (45 mg/kg/OS BID) or vehicle (Tween 80 0.5%, w/v, and HPMC 1.0%, w/v). Error bars denote the mean ± SD of eight CAD204520-treated animals or the mean ± SD of eight replicates vehicle-treated mice. Statistical significance for treated versus vehicle (n.s.) was determined by non-parametric t test (Mann-Whitney).

Figure 11. Resistance to SERCA inhibitors sensitize T-ALL cells to glucocorticoids

A) Small molecule viability screen results of EU-OPENSCREEN (European Chemical Biology Library) in ALL/SIL (blue lines) and ALL/SIL R (red lines) cell lines. All molecules were tested at 100 nM concentration. Radar plot shows the effect of individual drugs. From the left: small molecules active (viability < 50%) on either ALL/SIL R, both cell lines or ALL/SIL only.

B) Radar plots reporting drug screening viability results of compounds active on NR3C receptors in ALL/SIL (blue lines) and ALL/SIL R (red lines). All drugs were tested at 100 nM. Each subgroup of NR3C receptor is indicated with a different color.

C) Left: Western blotting showing expression of Notch1 pathway and total glucocorticoids receptor (GR) in T-ALL cell lines. Right: Real-time PCR results comparing the fold change in gene expression of glucocorticoids receptor isoforms in ALL/SIL and ALL/SIL R cell lines in basal conditions. The y axis represents the fold change between each condition and β-actin expression as an internal control. Error bar denotes the mean ± SD of a minimum of three replicates. Statistical significance among groups (****$p < 0.0001$) was determined by one-way ANOVA.

D) Effects of glucocorticoids on cell viability after 72 hours of treatments in T-ALL cell lines. Error bars denote ± SD of 2 replicates.

E) Effects of glucocorticoids on cell viability after 72 hours of treatments in T-ALL cell lines in basal conditions and after a rescue with ALL/SIL R medium. Error bars denote ± SD of 2 replicates. Black: rescue conditions; pink: basal conditions.

F) Effects of glucocorticoids on cell viability in ALL/SIL and ALL/SIL R T-ALL cell lines with the following conditions: after 72 hours of treatments, after 72 hours of treatments in combination with thapsigargin 10 nM; after a pre-treatment with RU486 1 μM and thapsigargin 10 nM for 24 hours and a following treatment with glucocorticoids for 72 hours. Error bars denote ± SD of 2 replicates.

G) Combination index (left) and surface plots analysis (right) of ALL/SIL and ALL/SIL R T-ALL cell lines treated with vehicle, CAD204520, fluticasone, or CAD204520 plus fluticasone. Each point means an independent measurement representative of two biological replicates. Plots were generated using Combenefit script by MATLAB R2021, which represents the Loewe (dose-effect based approach) analysis. A color scale bar represents the level of drugs antagonism or synergism.

Figure S1 (Related to Figure 4 and Table S1): Synthesis Route, Activity and Binding Mode of CAD204520.

A) Chemical structure of the initial hit compound: 2-(2-pyridyl)-6-(trifluoromethoxy)-1H-indole.

B) Schematic representation for medicinal chemistry optimization. R^1 and R^2 substitutions are indicated.

C) Synthesis route of CAD204520 (4-[2-[2-[3-propyl-6-(trifluoromethoxy)-1H-indol-2-yl]-1-piperidyl]ethyl]morpholine). Synthetic route (a) to (e) is depicted and described in the methods section.

D) Determination of the protein ATP hydrolysis activity in the presence of compound CAD204520 at pH 7. The figure displays ATPase activity determined by measuring the amount of liberated phosphate from ATP hydrolysis. Data is presented as a fitted curve which has been normalized to the maximal enzyme activity with subtraction of background signal from spontaneous hydrolysis of ATP. Error bars denote the mean ± SD (standard deviation) of 3 replicates. Statistical significance (**P ≤ 0.01; ***P ≤ 0.001) was determined by two-way ANOVA using Bonferroni's correction for multiple comparison testing.

E) Binding sites of CAD204520 and thapsigargin. Superposition of the SERCA-CAD204520 complex with SERCA-thapsigargin (PDB ID: 2AGV). The binding sites are both in the transmembrane region, separated by transmembrane helix M3. Thapsigargin is shown as cyan surface representation.

F) Superposition of SERCA-CAD204520 with SERCA-CPA (PDB ID 3FGO), viewed roughly along the membrane normal. CAD204520 and CPA are shown as orange and green sticks, respectively.

G) Superposition of SERCA-CAD204520 with SERCA-DBHQ (PDB ID 2AGV) viewed roughly along the membrane normal. CAD204520 and DBHQ are shown as orange and light blue, respectively.

H) Superposition of SERCA-CAD204520 with SERCA-Cpd7 (PDB ID 5NCQ), viewed along the membrane plane. CAD204520 and Cpd7 are shown as orange and magenta sticks, respectively.

I) Binding sites of CAD204520 and thapsigargin, as seen roughly along the membrane normal. Superposition of SERCA bound to CAD204520 (light blue cartoon and orange sticks, respectively) with SERCA bound to thapsigargin (grey cartoon and sticks, respectively). Glycine^{257}, which is mutated to valine in the thapsigargin resistant mutant, is indicated by a red sphere. In the SERCA-thapsigargin complex, Phe^{256} has undergone a displacement that is likely to be impaired by a valine residue in position 257.

Figure S2 (Related to Figure 5): Identification of a thapsigargin-resistant T-ALL cell line.

A) Effects of Thapsigargin (left) and CAD204520 (right) on cell viability after 72 hours of treatments in ALL/SIL and ALL/SIL thapsigargin-resistant cell lines. Error bars denote ± SD of a minimum of 2 replicates.

B) Western blot showing the expression of SERCA2 and SERCA3 in naïve and resistant ALL/SIL. β-actin was used as a loading control.

C) Phred-scale analysis of exonic single nucleotide variation (SNV) occurring in the ALL/SIL thapsigargin resistant cell line. Inset shows number (N.) of variation (SNV) occurring per chromosome.

D) Thapsigargin resistance mutation hot spot region on helix M3. Thapsigargin and SERCA residues 254-260 are shown in stick representation and colored cyan and red, respectively.

E) Surface plots analysis of ALL/SIL, DND41 and RPMI-8402 T-ALL cell lines and a primary *NOTCH1*-mutated T-ALL sample treated vehicle, CAD204520, cyclopiazonic acid, or CAD204520 plus cyclopiazonic acid. Each point represents an independent measurement representative of three biological replicates. Plots were generated using Combenefit script by MATLAB R2018 and represent the Loewe (dose-effect based approach) analysis. A color scale bar represents level of drug antagonism or synergism.

Figure S3 (Related to Figure 6): Effect of CAD204520 on *NOTCH1* mutated and wild type T-ALL and MCL cell lines.

A) Table representing *NOTCH1* mutational status in T-ALL and MCL lines.

B) Scatter dot plot representing IC50 [μM] of CAD204520 in *NOTCH1* mutated (n = 5) or *NOTCH1* WT (n = 3) T-ALL or in *NOTCH1* mutated (n = 1) or *NOTCH1* WT (n = 3) MCL (shown in C) cell line. Statistical significance (*P ≤ 0.05) was determined by a non-parametric t-test (Mann-Whitney).

D) Effect of CAD204520 treatments on cycling MAVER-1 and MINO cells. Percentage of DNA content following four days of treatment with the indicated concentrations of CAD204520 on each cell cycle phase is indicated. A minimum of 20,000 events was collected for each condition.

Figure S4 (Related to Figure 7): Effect of CAD204520 on Notch1 Trafficking.

A) Effect of CAD204520 and thapsigargin treatment for 24 hours on NOTCH1 (N1) processing and activation in T-ALL cell lines. The immunoblot was incubated with an antibody against the C-terminus of NOTCH1 that recognizes the transmembrane subunit (TM) and an antibody that recognizes the cleaved NOTCH1 (ICN1). GAPDH was used as a loading control.

B) Effect of 24 hours of CAD204520 on NOTCH1 cell surface staining as assessed by immunofluorescence in DND41 T-ALL cells. Scale bars: 100 μm.

C) Quantitative immunofluorescence analysis of NOTCH1 surface signal in DND41 cells after 24 hours of CAD204520 treatment. Error bars denote the mean ± standard deviation (SD) of fluorescence of 70 single cells/nuclei (arbitrary units); Statistical significance among groups was determined by unpaired t-test (***P ≤ 0.001).

D) Effect of 24 hours of CAD204520 on NOTCH1 cell surface staining as assessed by immunofluorescence in REC-1 MCL cells. Scale bars: 100 μm.

E) Quantitative immunofluorescence analysis of NOTCH1 surface signal in REC-1 cells after 24 hours of CAD204520 treatment. Error bars denote the mean ± standard deviation (SD) of fluorescence of 70 single cells/nuclei (arbitrary units); Statistical significance among groups was determined by unpaired t-test (***P ≤ 0.001).

F) Effect of 24 hours treatment of CAD204520 on NOTCH1 (N1) processing and activation in REC-1 cell line. The blot was incubated with an antibody against the C-terminus of NOTCH1 that recognizes the NOTCH1 transmembrane subunit (TM). GAPDH was used as a loading control.

Figure S5 (Related to Figure 8): Genomic characterization of MOLT16 and SKW-3/KE-37 T-ALL cell lines.

A) Genomic characterization of MOLT16 and SKW-3/KE-37 T-ALL cell line. The karyotype and the mutational analysis are indicated.

B) Effects of CAD204520 on cell viability after 72 hours of treatments in MOLT16 and SKW/KE-37 T-ALL cell lines. Error bars denote ± SD of 2 replicates. Statistical significance among groups was determined by 2-way ANOVA (**P ≤ 0.01, ***P ≤ 0.001).

C) Pro-apoptotic effect of CAD204520 treatment. Annexin V/propidium iodide staining of primary *NOTCH1* mutated T-ALL cells following 72 hours of treatment with the indicated concentrations of CAD204520. A minimum of 20,000 events was collected for each condition.

Figure S6 (Related to Figure 9): Consequences of CAD204520 o UPR pathway.

A) Effect of CAD204520 and thapsigargin treatment for 24 hours in RPMI-8402 cell lines. The immunoblot was stained with an antibody against the C-terminus of NOTCH1 that recognizes the furin-processed NOTCH1 transmembrane subunit (TM) and the unprocessed NOTCH1 precursor (FL), an antibody that recognizes the cleaved NOTCH1 (ICN1), and antibodies that recognize the activation of the UPR pathway. P-eIF2α, eIF2α, total BiP. HSP90 was used as a loading control.

B) Quantitative immunofluorescence analysis of nuclear ATF6 signal in ALL/SIL cells after 24 hours of CAD204520 treatment. Error bars denote the mean ± standard deviation (SD)

of fluorescence of 70 single cells/nuclei (arbitrary units); Statistical significance among groups was determined using one-way ANOVA with Bonferroni's correction for multiple comparison testing (***P ≤ 0.001).

C) Effect of CAD204520 and thapsigargin treatment in HL-1 and ALL/SIL cell lines. Histograms show percentage of cell alive after 72 hours of treatment at indicates doses. Error bar denotes the mean ± SD of a minimum of three replicates. Statistical significance among groups (****P ≤ 0.0001) was determined by 2-way ANOVA.

Figure S7 (Related to Figure 10): Preclinical Toxicity and Activity of CAD204520.

A-B left panels) Effect of CAD204520 treatment on rat cardiomyocyte calcium transients. Single experiments are represented by two dots interconnected by a solid line. Specifically, the line between dots connects the quantification of the amplitude of the calcium transient (A: f/f0) and the time required for cytosolic calcium removal (B: TAU), before and after the CAD204520 (5 μM) treatment compared to control (Control). A-B right panels): Mean percentage variation of CAD204520 (CAD204520) on the same parameters. Graph bars: mean ± SD of the 5 CAD204520 treated cardiomyocyte groups. Statistical significance comparing CAD204520 treated cells vs. Control cells (*P ≤ 0.05) was determined by a non-parametric t-test (Mann-Whitney).

C) Representative examples of calcium transients (normalized traces: fold increase) recorded from control (solid lane), CAD204520 (5 μM) (dashed line), and thapsigargin (0.2 μM) (dotted line) ventricular myocytes.

D) ATP Luminescence induction normalized to cellular protein content in rat cardiomyocytes treated either with CAD204520 or vehicle (Control). Error bars denote the mean ± SD of 6

replicates. Statistical significance comparing CAD204520 treated cells vs. vehicle treated cells (not significant = n.s.) was determined by a non-parametric t-test (Mann-Whitney).

E) Effect of administration of CAD204520 on bodyweight. Error bars denote the mean ± SD of 6 replicates. Animals were treated for 6 days with 30mg/Kg of CAD204520 and subsequently treated with 60 mg/Kg daily. Statistical significance (**P ≤ 0.01) was determined by a 2-way ANOVA analysis. Representative schema of CAD204520 *in vivo* studies.

F) Effect of CAD204520 on T-ALL leukemia burden in a SKW-3/KE-37 xenografted murine model. Anti-leukemic activity of CAD204520 assessed by measuring hCD45+ cells after 4 days of CAD204520 treatment (45 mg/kg/OS BID) or vehicle (tween-80 0.5% w/v and HPMC 1.0% w/v). Error bars denote the mean ± SD of 9 CAD204520 treated animals or the mean ± SD of 8 replicates vehicles treated mice. Statistical significance for treated vs. vehicle (****P ≤ 0.0001) was determined by non-parametric t-test (Mann-Whitney).

H) Antileukemic activity of CAD204520 in hCD45+ spleen infiltrating cells in a SKW-3/KE-37 xenografted murine model after 5 days of CAD204520 treatment (45 mg/kg/OS BID) or vehicle (tween-80 0.5% w/v and HPMC 1.0% w/v). The number of hCD45+ cells per field were represented as percentage relative to vehicle control. Error bars denote the mean ± SD of 13 fields from 2 mice treated with CAD204520 or the mean ± SD of 12 fields from 3 vehicle treated mice. Statistical significance for treated vs. vehicle (****P ≤ 0.0001) was determined by non-parametric t-test (Mann-Whitney).

Table S1 (Related to Figure 4 and Figure S1): H^+, Na/K^+, Ca^{2+} ATP hydrolysis of 2-(2-pyridyl)-6-(trifluoromethoxy)-1H-indole derivatives.

Data of compounds fitted to the pharmacophore model. ATPase hydrolysis activity toward H^+, Ca^{2+} and Na^+/K^+-ATPase is indicated as the half maximal inhibitory concentration (IC50) and expressed in μM. The ligand efficiency index is equal to LE = 1.4(-logIC50)/N. N is the number of non-hydrogen atoms.

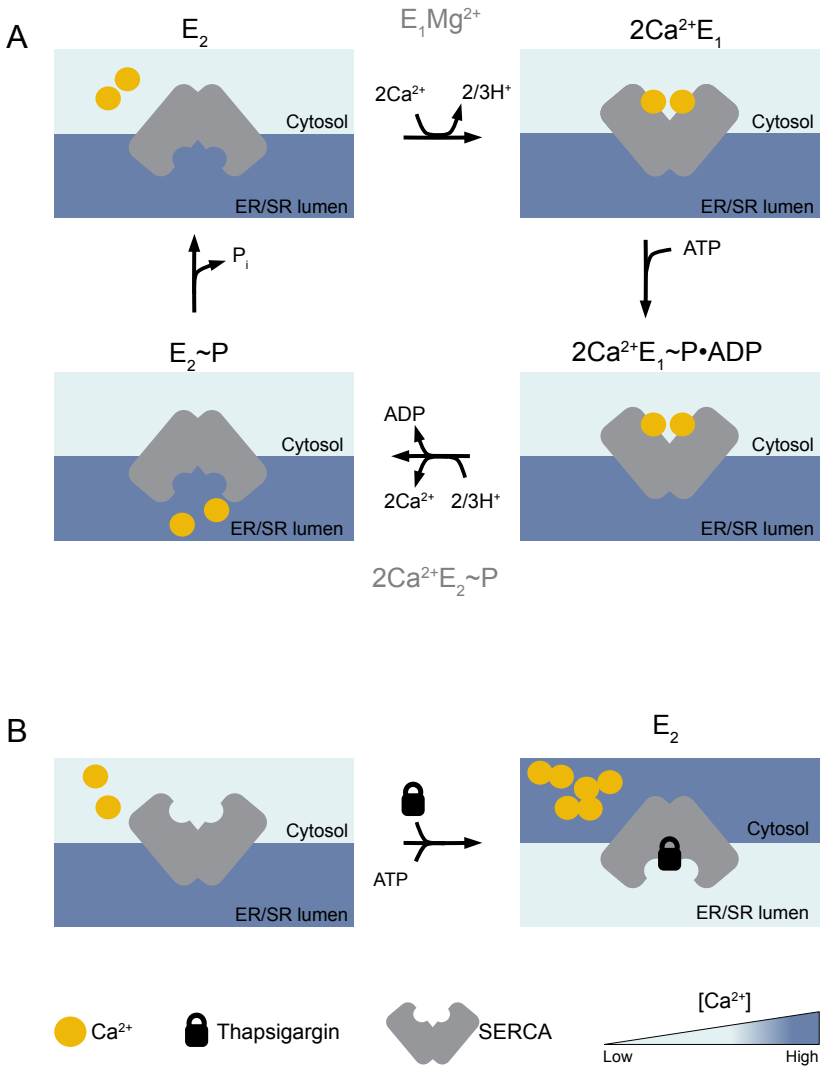
A
E2
E1Mg2+
2Ca2+E1
Cytosol
ER/SR lumen
2Ca2+
2/3H+
Pi
ATP
E2~P
2Ca2+E1~P•ADP
ADP
2Ca2+
2/3H+
2Ca2+E2~P
B
E2
ATP
Ca2+
Thapsigargin
SERCA
[Ca2+]
Low
High

Figure 1

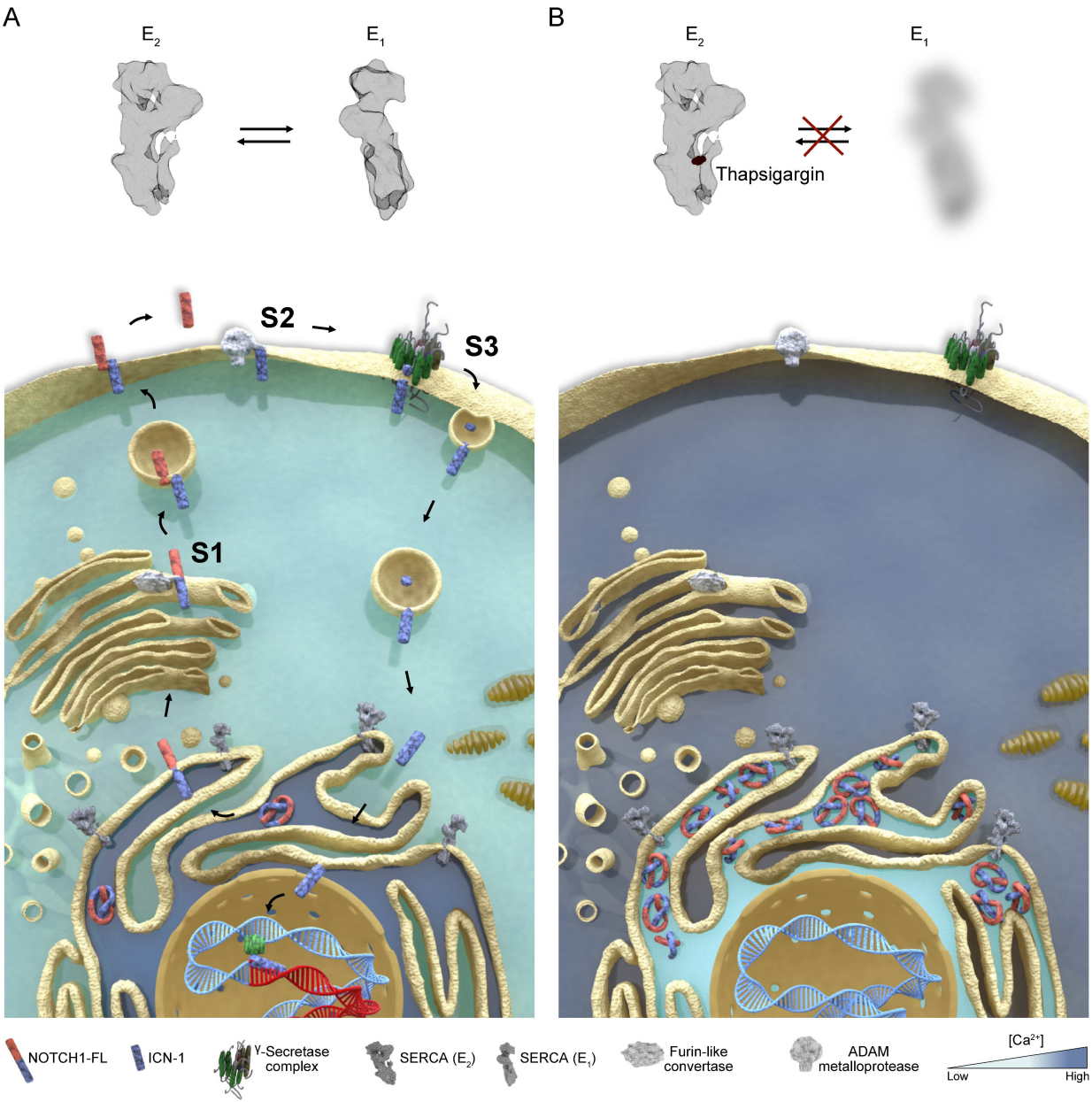
A
E2
E1
B
E2
E1
Thapsigargin
S1
S2
S3
NOTCH1-FL
ICN-1
γ-Secretase complex
SERCA (E2)
SERCA (E1)
Furin-like convertase
ADAM metalloprotease
[Ca2+]
Low
High

Figure 2

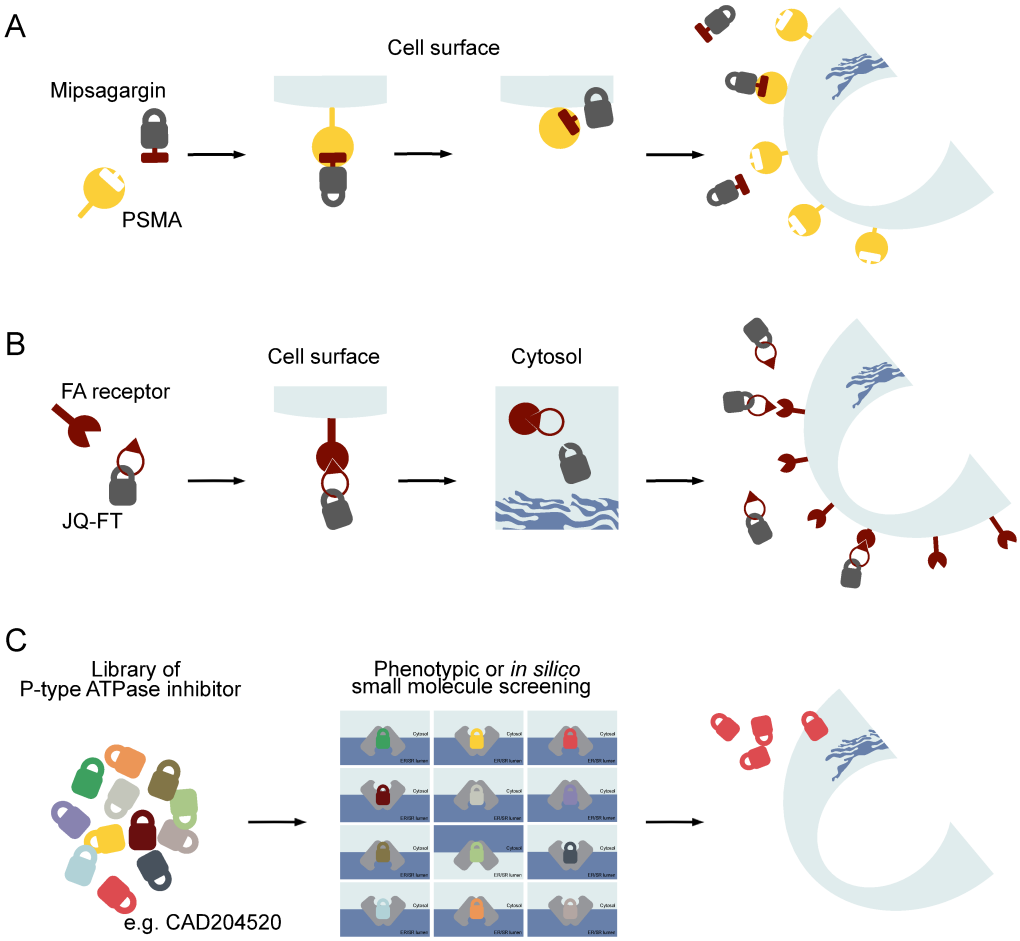
A
Cell surface
Mipsagargin
PSMA
B
Cell surface
Cytosol
FA receptor
JQ-FT
C
Library of
P-type ATPase inhibitor
Phenotypic or *in silico*
small molecule screening
e.g. CAD204520

Figure 3

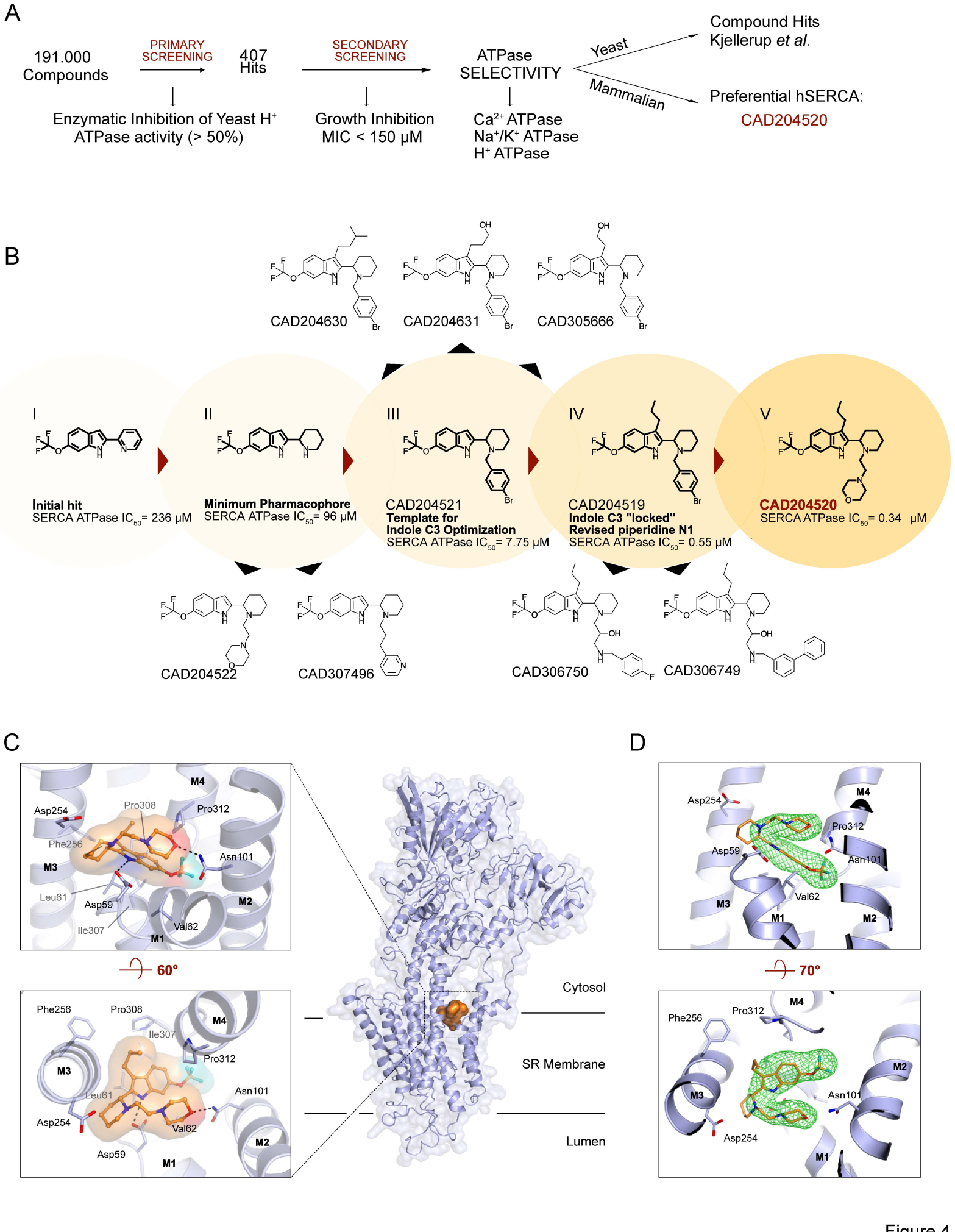
A
191.000 Compounds
PRIMARY SCREENING
407 Hits
SECONDARY SCREENING
ATPase SELECTIVITY
Yeast
Mammalian
Compound Hits Kjellerup et al.
Preferential hSERCA:
CAD204520
Enzymatic Inhibition of Yeast H+ ATPase activity (> 50%)
Growth Inhibition MIC < 150 µM
Ca2+ ATPase
Na+/K+ ATPase
H+ ATPase
B
CAD204630
CAD204631
CAD305666
I
II
III
IV
V
Initial hit
SERCA ATPase IC50= 236 µM
Minimum Pharmacophore
SERCA ATPase IC50= 96 µM
CAD204521
Template for Indole C3 Optimization
SERCA ATPase IC50= 7.75 µM
CAD204519
Indole C3 "locked" Revised piperidine N1
SERCA ATPase IC50= 0.55 µM
CAD204520
SERCA ATPase IC50= 0.34 µM
CAD204522
CAD307496
CAD306750
CAD306749
C
D
M4
Asp254
Pro308
Pro312
Phe256
Asn101
M3
Leu61
Asp59
M2
Ile307
Val62
M1
60°
70°
Cytosol
SR Membrane
Lumen

Figure 4

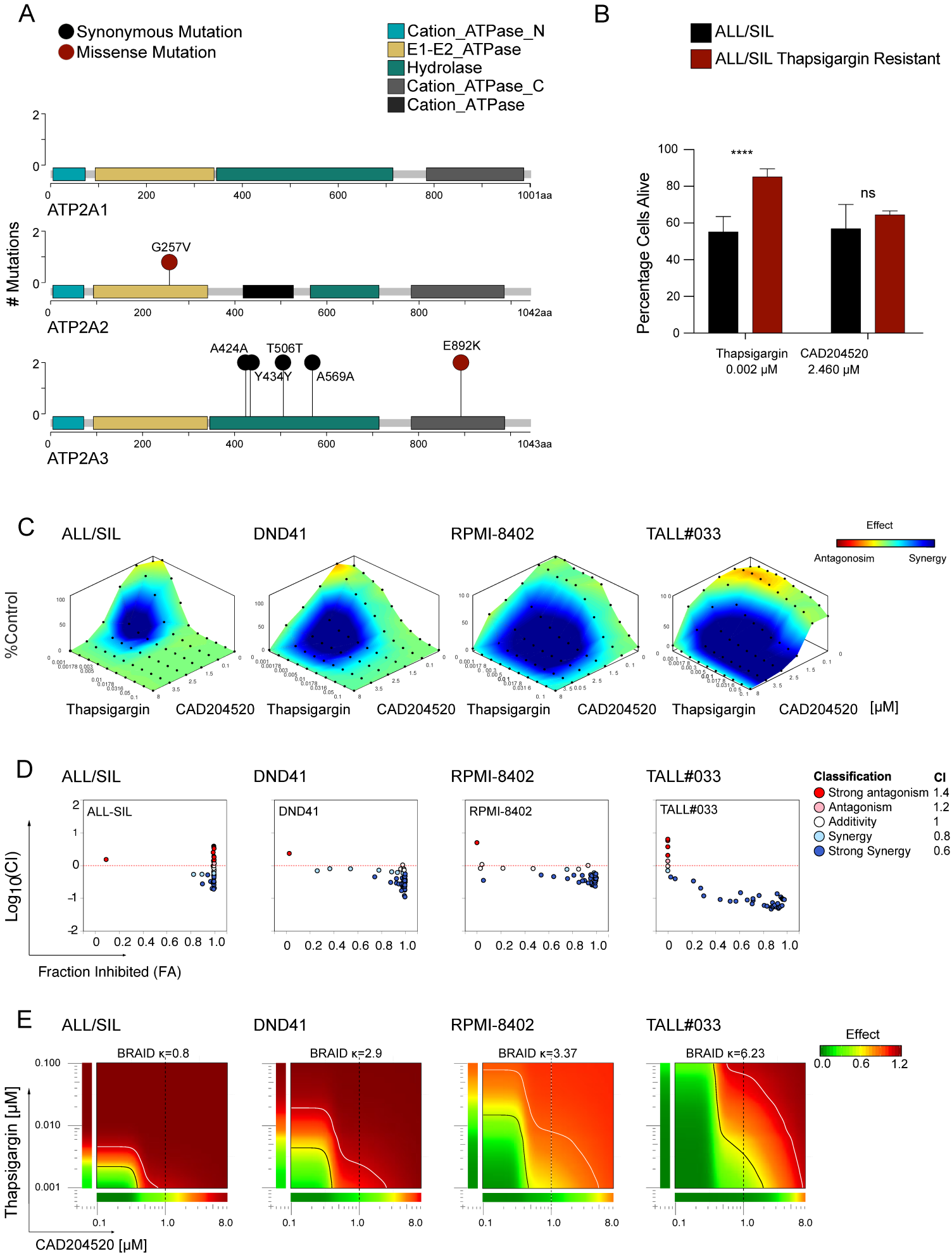
A
Synonymous Mutation
Missense Mutation
Cation_ATPase_N
E1-E2_ATPase
Hydrolase
Cation_ATPase_C
Cation_ATPase
Mutations
ATP2A1
1001aa
ATP2A2
G257V
1042aa
ATP2A3
A424A
T506T
Y434Y
A569A
E892K
1043aa
B
ALL/SIL
ALL/SIL Thapsigargin Resistant
Percentage Cells Alive
****
ns
Thapsigargin
0.002 µM
CAD204520
2.460 µM
C
ALL/SIL
DND41
RPMI-8402
TALL#033
Effect
Antagonosim
Synergy
%Control
Thapsigargin
CAD204520
[µM]
D
ALL/SIL
DND41
RPMI-8402
TALL#033
Log10(CI)
Fraction Inhibited (FA)
Classification
CI
log10(CI)
Strong antagonism 1.4 0.20
Antagonism 1.2 0.08
Additivity 1 0.00
Synergy 0.8 -0.10
Strong Synergy 0.6 -0.22
E
ALL/SIL
DND41
RPMI-8402
TALL#033
BRAID κ=0.8
BRAID κ=2.9
BRAID κ=3.37
BRAID κ=6.23
Effect
Thapsigargin [µM]
CAD204520 [µM]

Figure 5

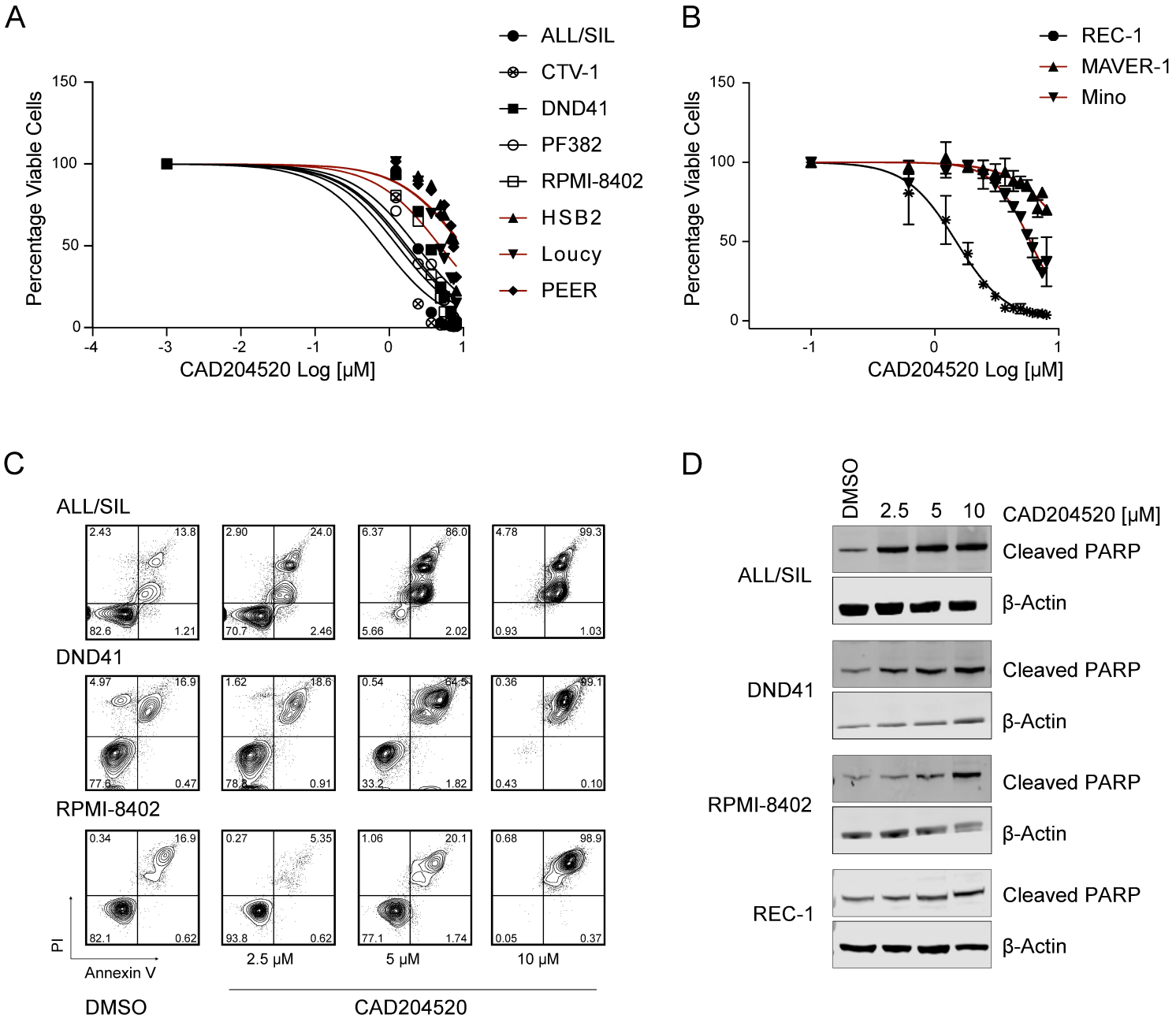
A
ALL/SIL
CTV-1
DND41
PF382
RPMI-8402
HSB2
Loucy
PEER
Percentage Viable Cells
CAD204520 Log [μM]
B
REC-1
MAVER-1
Mino
Percentage Viable Cells
CAD204520 Log [μM]
C
ALL/SIL
DND41
RPMI-8402
PI
Annexin V
DMSO
2.5 μM
5 μM
10 μM
CAD204520
D
DMSO
2.5
5
10
CAD204520 [μM]
ALL/SIL
DND41
RPMI-8402
REC-1
Cleaved PARP
β-Actin
E
% of Cells/Cell Cycle Phase
G1
S
G2
DMSO
1.25
10
CAD204520 [μM]
ALL/SIL
DND41
RPMI-8402
REC-1

Figure 6

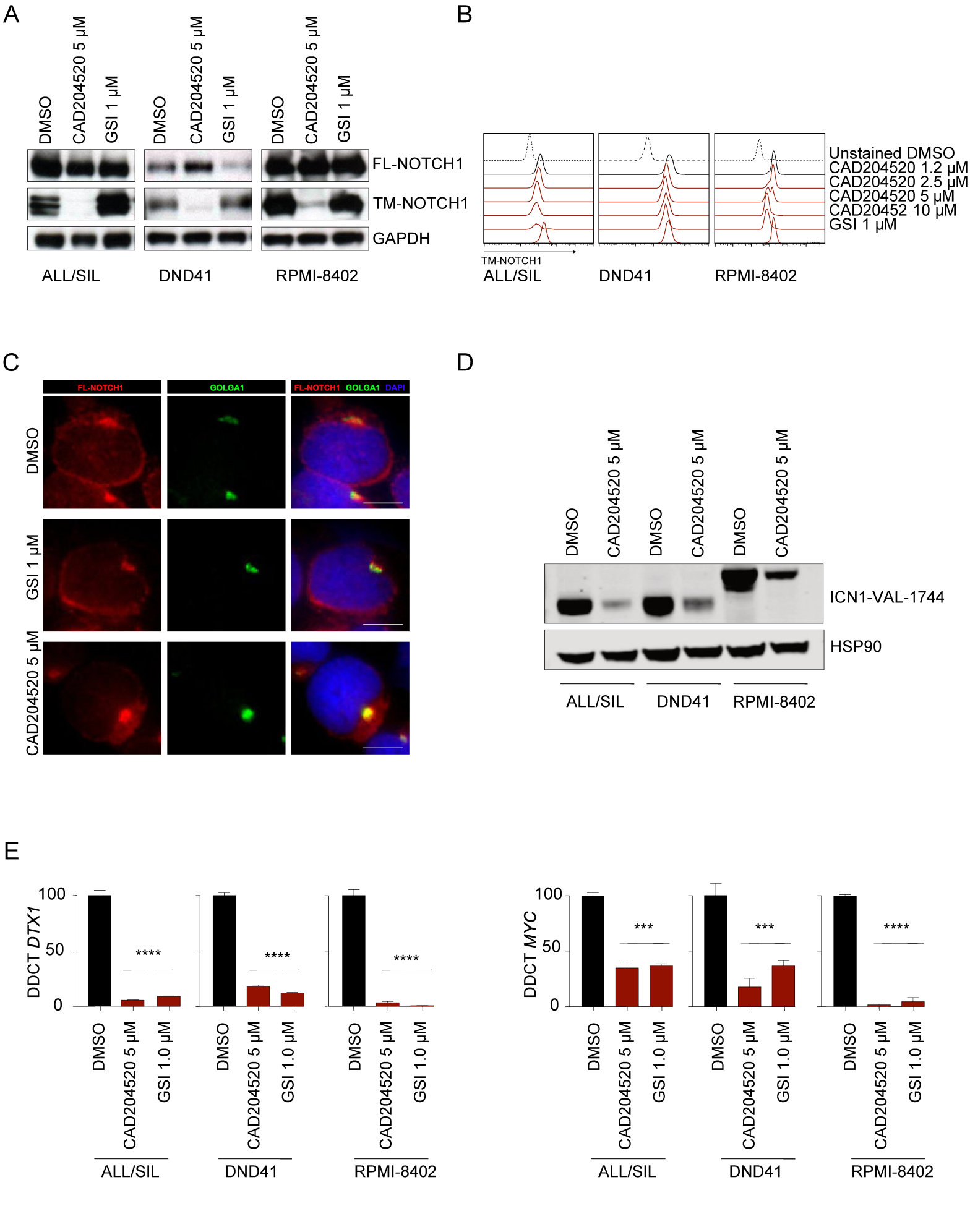
A
DMSO
CAD204520 5 µM
GSI 1 µM
FL-NOTCH1
TM-NOTCH1
GAPDH
ALL/SIL
DND41
RPMI-8402
B
Unstained DMSO
CAD204520 1.2 µM
CAD204520 2.5 µM
CAD204520 5 µM
CAD20452 10 µM
GSI 1 µM
TM-NOTCH1
ALL/SIL
DND41
RPMI-8402
C
FL-NOTCH1
GOLGA1
FL-NOTCH1 GOLGA1 DAPI
DMSO
GSI 1 µM
CAD204520 5 µM
D
DMSO
CAD204520 5 µM
ICN1-VAL-1744
HSP90
ALL/SIL
DND41
RPMI-8402
E
DDCT DTX1
100
50
0
****
DMSO
CAD204520 5 µM
GSI 1.0 µM
ALL/SIL
DND41
RPMI-8402
DDCT MYC
***
****

Figure 7

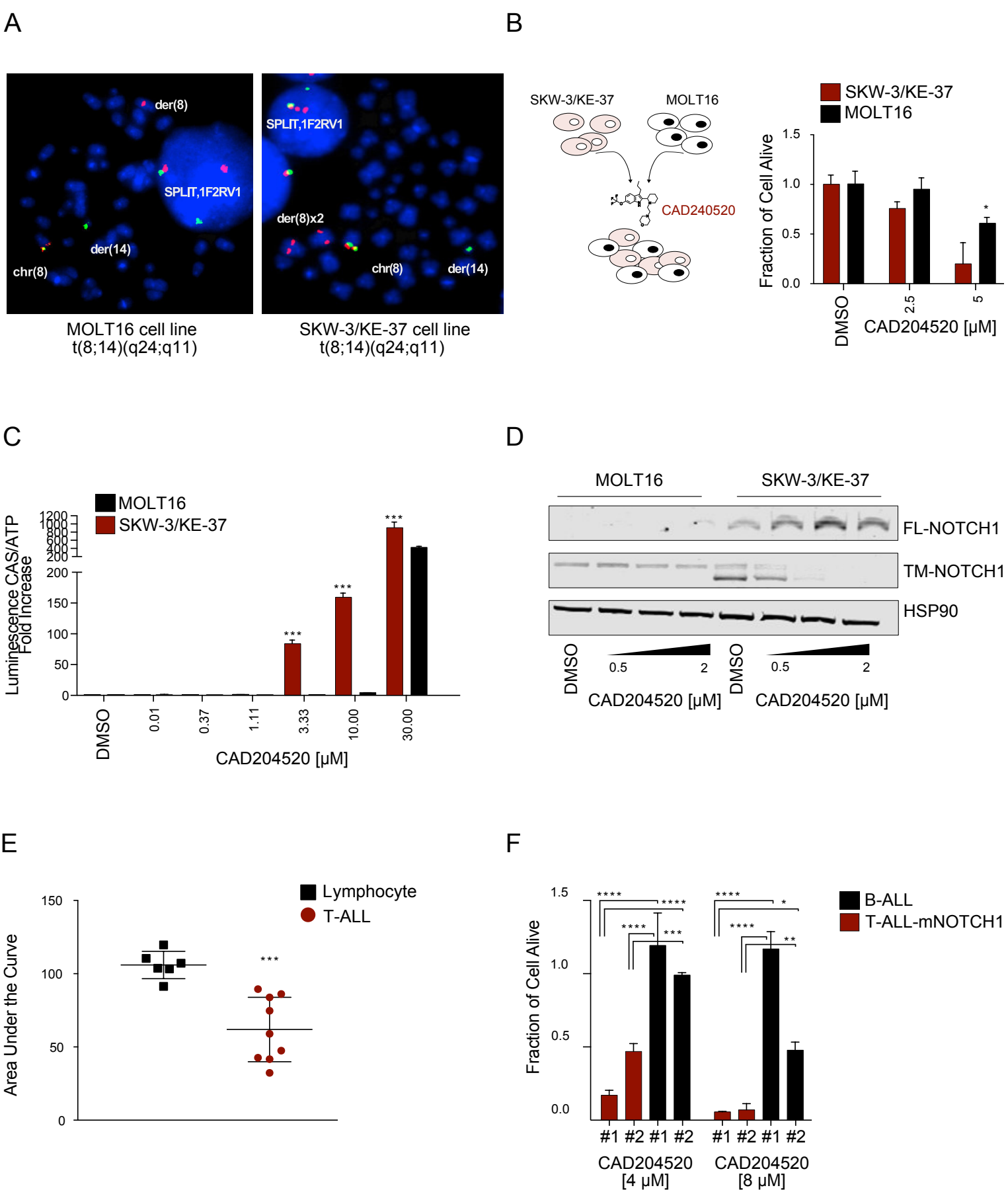
A
der(8)
SPLIT,1F2RV1
der(14)
chr(8)
MOLT16 cell line
t(8;14)(q24;q11)
SPLIT,1F2RV1
der(8)x2
chr(8)
der(14)
SKW-3/KE-37 cell line
t(8;14)(q24;q11)
B
SKW-3/KE-37
MOLT16
CAD240520
SKW-3/KE-37
MOLT16
Fraction of Cell Alive
1.5
1.0
0.5
0.0
DMSO
2.5
5
CAD204520 [µM]
C
MOLT16
SKW-3/KE-37
Luminescence CAS/ATP
Fold Increase
1200
1000
800
600
400
200
200
150
100
50
0
***
***
***
DMSO
0.01
0.37
1.11
3.33
10.00
30.00
CAD204520 [µM]
D
MOLT16
SKW-3/KE-37
FL-NOTCH1
TM-NOTCH1
HSP90
DMSO
0.5
2
DMSO
0.5
2
CAD204520 [µM]
CAD204520 [µM]
E
Lymphocyte
T-ALL
Area Under the Curve
150
100
50
0
***
F
B-ALL
T-ALL-mNOTCH1
Fraction of Cell Alive
1.5
1.0
0.5
0.0
****
****
****
***
****
*
****
**
#1 #2 #1 #2
#1 #2 #1 #2
CAD204520
[4 µM]
CAD204520
[8 µM]

Figure 8

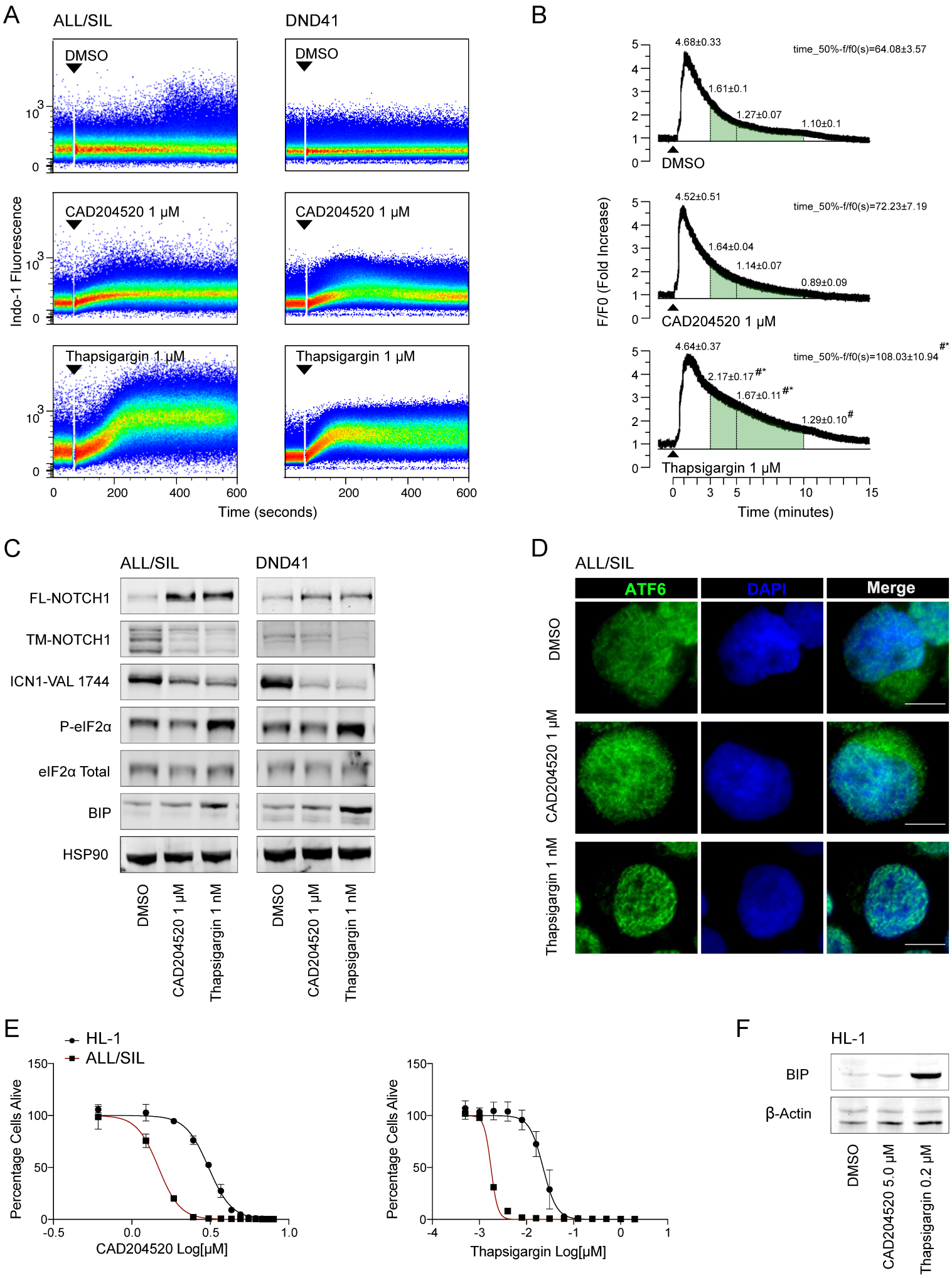
A
ALL/SIL
DND41
DMSO
CAD204520 1 μM
Thapsigargin 1 μM
Indo-1 Fluorescence
Time (seconds)
B
4.68±0.33
time_50%-f/f0(s)=64.08±3.57
1.61±0.1
1.27±0.07
1.10±0.1
4.52±0.51
time_50%-f/f0(s)=72.23±7.19
1.64±0.04
1.14±0.07
0.89±0.09
4.64±0.37
time_50%-f/f0(s)=108.03±10.94
2.17±0.17
1.67±0.11
1.29±0.10
F/F0 (Fold Increase)
Time (minutes)
C
ALL/SIL
DND41
FL-NOTCH1
TM-NOTCH1
ICN1-VAL 1744
P-eIF2α
eIF2α Total
BIP
HSP90
DMSO
CAD204520 1 μM
Thapsigargin 1 nM
D
ALL/SIL
ATF6
DAPI
Merge
DMSO
CAD204520 1 μM
Thapsigargin 1 nM
E
HL-1
ALL/SIL
Percentage Cells Alive
CAD204520 Log[μM]
Thapsigargin Log[μM]
F
HL-1
BIP
β-Actin
DMSO
CAD204520 5.0 μM
Thapsigargin 0.2 μM

Figure 9

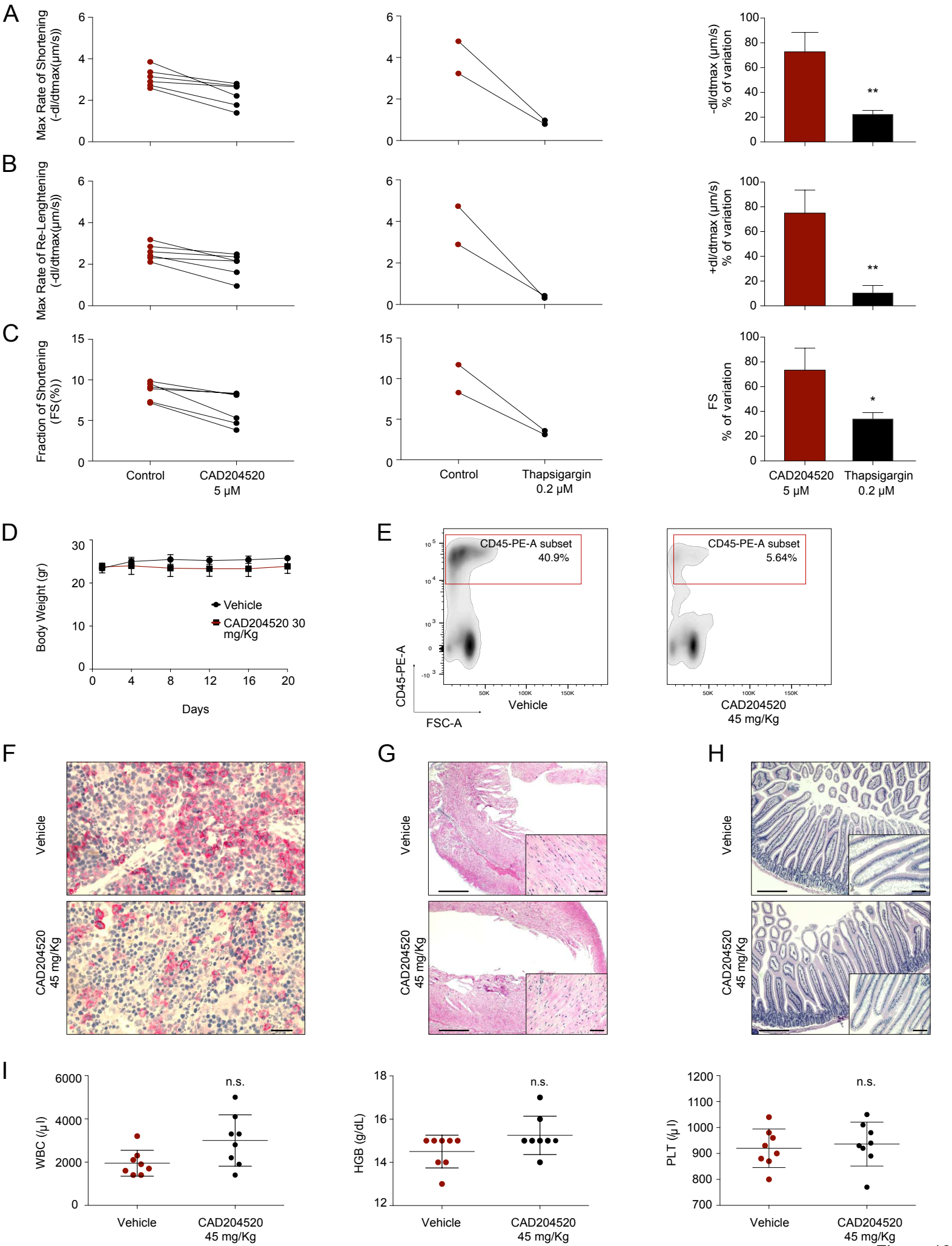
A
Max Rate of Shortening (-dl/dtmax(µm/s))
Control
CAD204520 5 µM
Thapsigargin 0.2 µM
-dl/dtmax (µm/s) % of variation
**
B
Max Rate of Re-Lenghtening (-dl/dtmax(µm/s))
+dl/dtmax (µm/s) % of variation
**
C
Fraction of Shortening (FS(%))
FS % of variation
*
D
Body Weight (gr)
Vehicle
CAD204520 30 mg/Kg
Days
E
CD45-PE-A subset 40.9%
CD45-PE-A subset 5.64%
CD45-PE-A
FSC-A
Vehicle
CAD204520 45 mg/Kg
F
G
H
I
WBC (/µl)
HGB (g/dL)
PLT (/µl)
n.s.

Figure 10

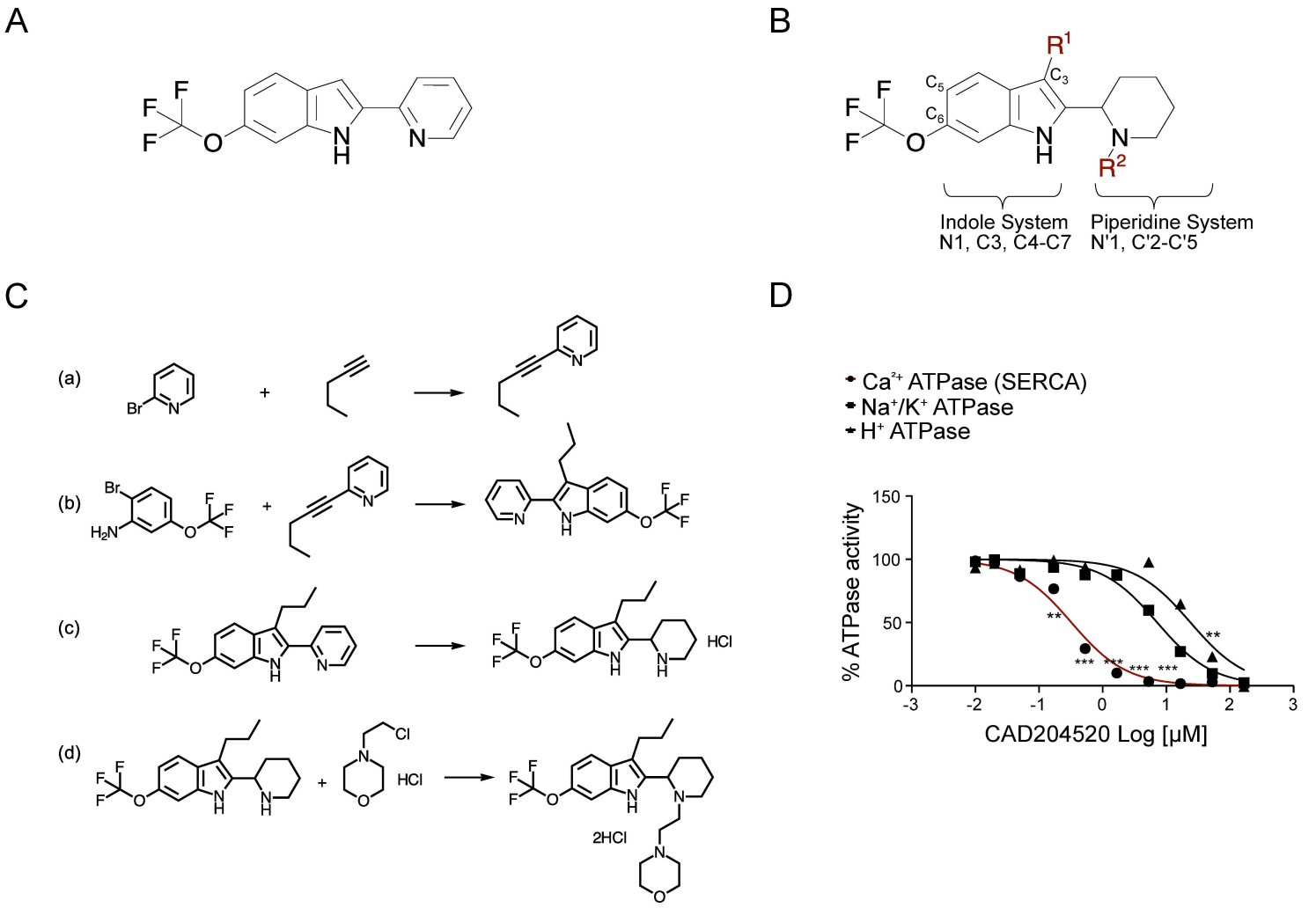

Supplementary Figure S1

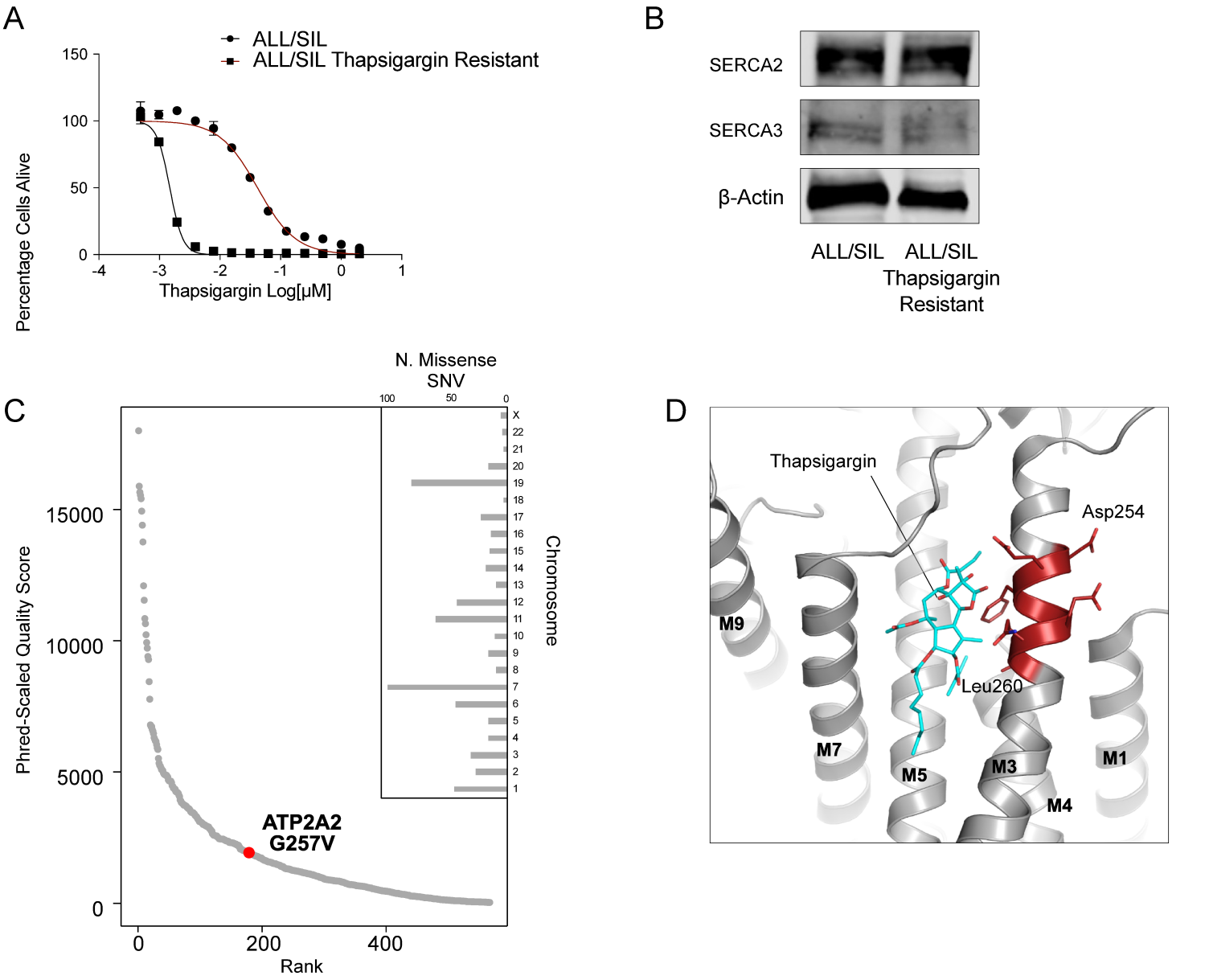

Supplementary Figure S2

A

T-ALL Cell Line	NOTCH Protein Domains		CAD204520 IC_{50} [μM]
	Heterodimerization (HD)	Proline, Glutamic Acid, Serine and Threonine (PEST)	
ALL/SIL	Mutated	Mutated	2.1
DND41	Mutated	Mutated	3.1
RPMI-8402	M u t a ted	WT	2.5
PF382	Mutated	Mutated	1.5
SKW-3/KE-37	WT	Mutated	1.5
PEER	WT	WT	9.9
Loucy	WT	WT	4.8
MOLT16	WT	WT	2.3
HSB2	WT	WT	9.5
CTV-1	WT	Mutated	0.8
REC-1	WT	Mutated	1.4
MAVER-1	WT	WT	12.7
Mino	WT	Mutated*	5.9

* PEST domain mutation p.Q2487* (exon 34). The effect of this mutation is to be considered ligand-dependent. E. Silkenstedt, F. Arenas, B. Colom-Sanmartì et al. Notch1 signaling in *NOTCH1*-mutated mantle cell lymphoma depends on *Delta-Like* ligand 4 and is a potential target for specific antibody therapy. J. Exp. Clin. Cancer Res, 2019. **38**(1), 446.

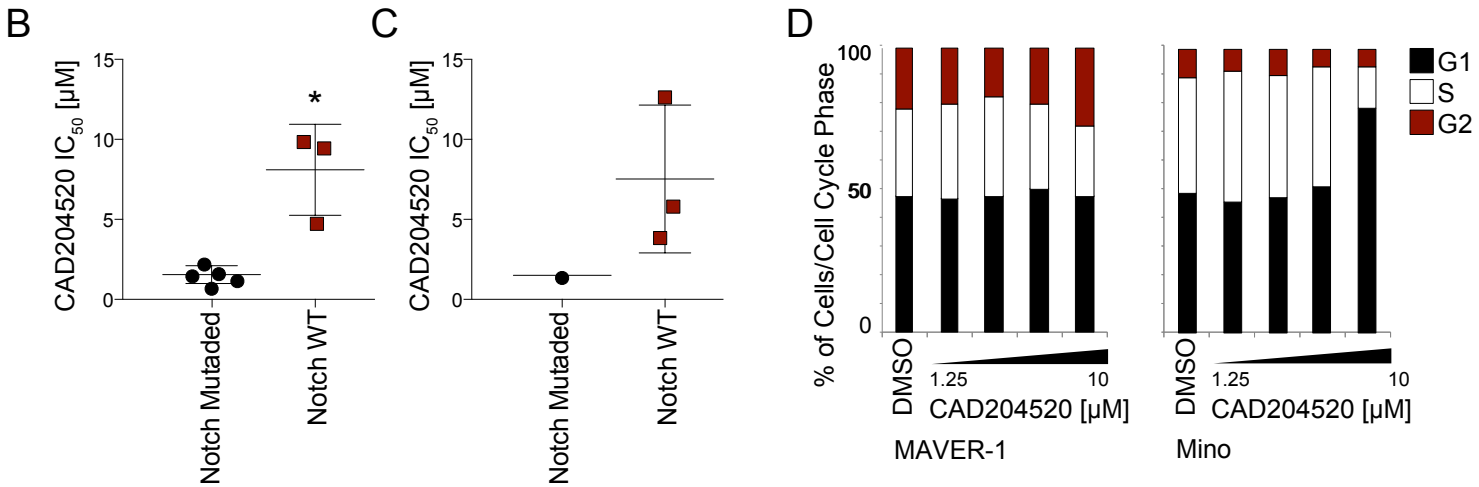

Supplementary Figure S3

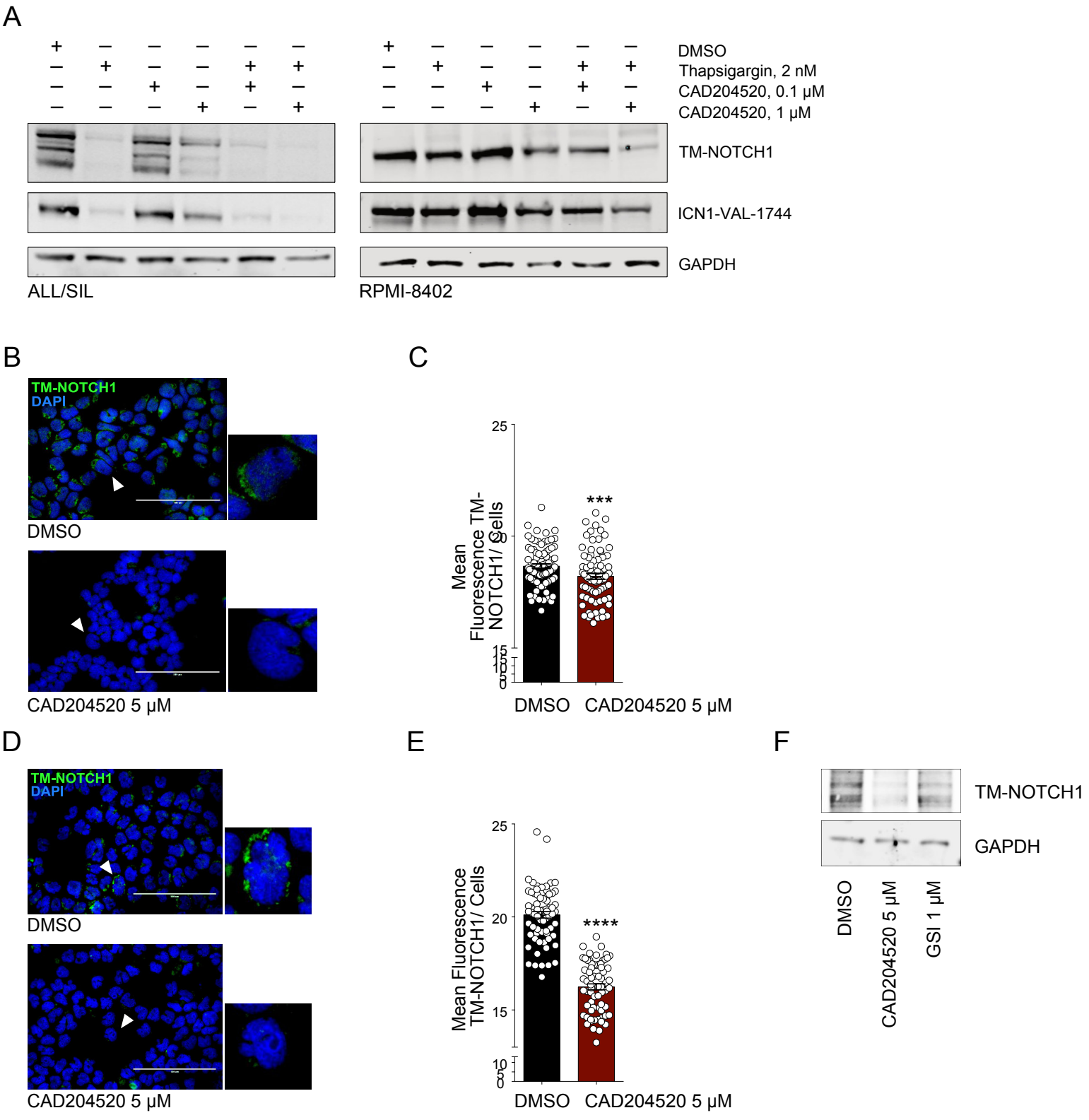

Supplementary Figure S4

A

CELL LINES	GENOMIC PROFILE
MOLT16	*SIL-TAL1* t(3;11)(p21;p13)/*LMO2* translocation with non-*TR@* partner t(8;14)(q24;q32)/*TRAD@-MYC* *CDKN2AB* biallelic deletion *PTEN* c.735-736insCTTA p.P246fs*12 (exon 7)
SKW-3/KE-37	t(8;11)(p11-12;p13)/*LMO2* translocation with non-*TR@* partner t(8;14)(q24;q32)/*TRAD@-MYC* *CDKN2AB* biallelic deletion *PTEN* biallelic deletion *NOTCH1* c7375C>T p.Q2459* (exon 34)

B

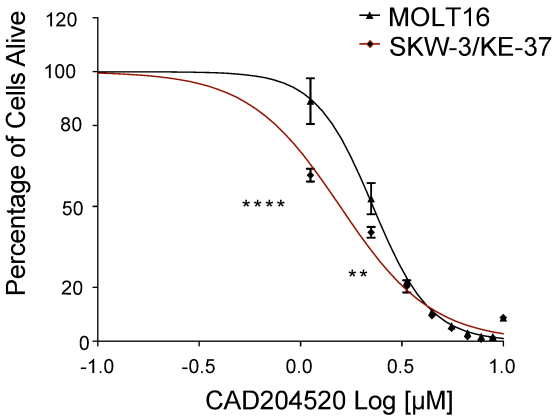

C

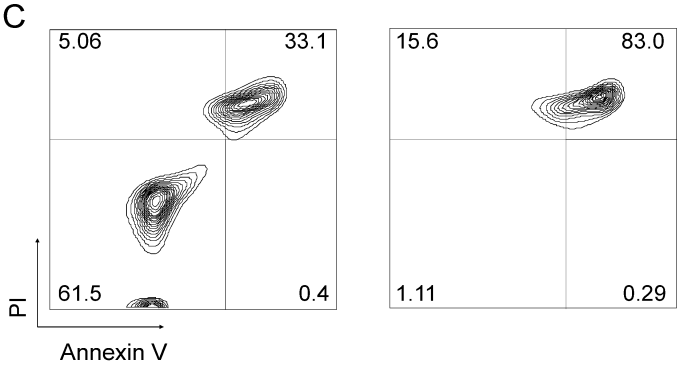

Supplementary Figure S5

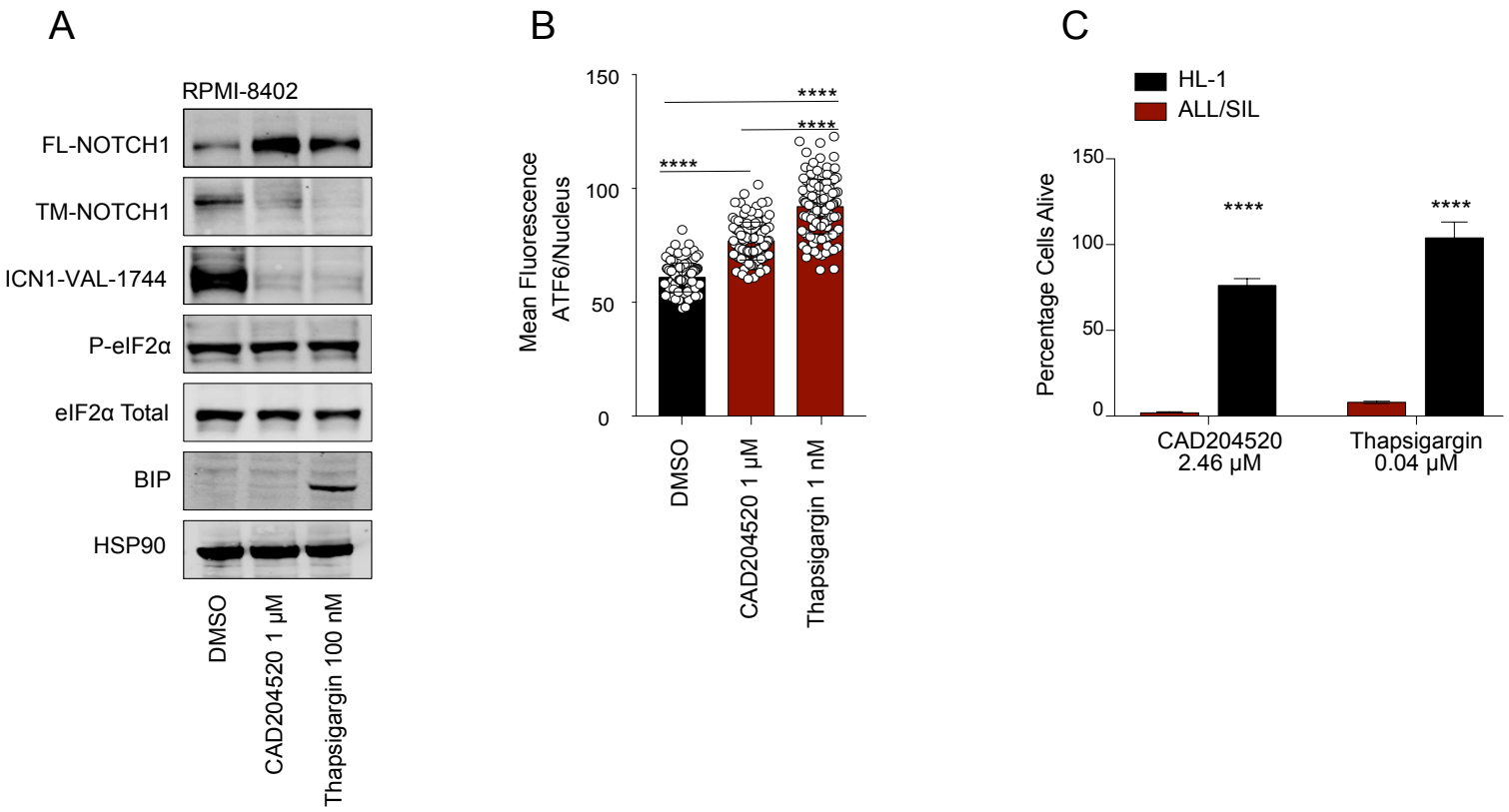

Supplementary Figure S6

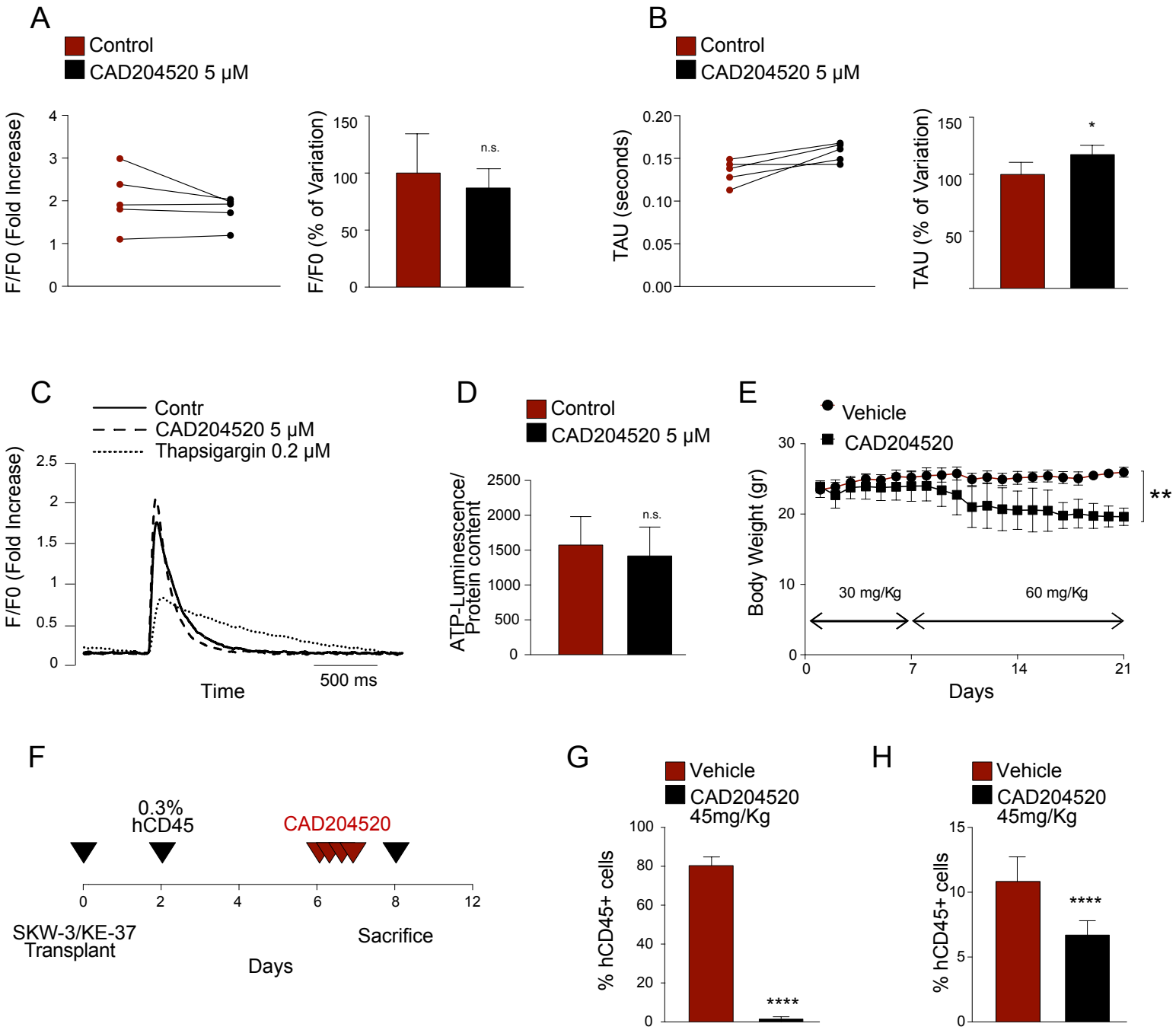

Supplementary Figure S7

Compound	Structure	ATP hydrolysis IC_{50} [μM]			SERCA Ligand Efficiency Index (LE)
		H^+- ATPase	Na^+,K^+- ATPase	Ca^{2+}- ATPase (SERCA)	
CAD204522	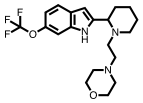	126.80 ±14.94	22.56 ±5.48	30.14 ±5.61	0.20
CAD307496	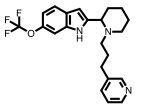	37.68 ±6.22	20.09 ±2.76	58.86 ±6.50	0.21
CAD204521	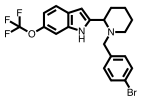	21.81 ±4.50	0.28 ±0.07	7.75 ±1.68	0.26
CAD204630	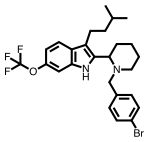	>333	0.04 ±0.01	1.56 ±0.45	0.25
CAD204631	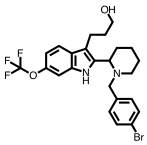	71.25±18.00	3.16 ±0.41	18.00 ±3.25	0.21
CAD305666	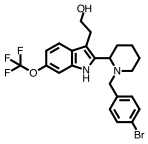	9.74 ±1.67	0.39 ±0.20	1.03 ±0.22	0.27
CAD204519	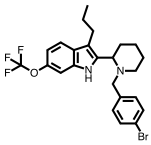	84.22±24.37	0.01 ±0.02	0.55 ±0.12	0.28
CAD204520	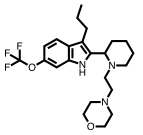	26.90 ±2.98	8.30 ±0.95	0.34 ±0.03	0.29
CAD306749	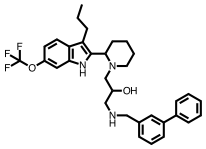	7.75 ±2.69	0.59 ±0.17	0.32 ±0.19	0.22
CAD306750	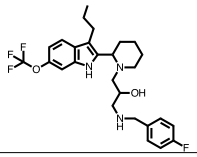	16.80 ±2.68	1.21 ±0.37	2.62 ±0.83	0.22

Table S1